TECHNICAL REPORT

SER. ELECTRICAL ENGINEERING

CENTRE ESTIMATION IN MARKER BASED MOTION ANALYSIS

ÁKOS JOBBÁGY

Department of Measurement and Instrument Engineering
Technical University of Budapest

No. TUB–TR–93–EE04

BUDAPEST, April 15, 1993

TECHNICAL UNIVERSITY OF BUDAPEST

TECHNICAL REPORT

SER. ELECTRICAL ENGINEERING

CENTRE ESTIMATION IN MARKER BASED MOTION ANALYSIS

ÁKOS JOBBÁGY

Department of Measurement and Instrument Engineering
Technical University of Budapest

No. TUB–TR–93–EE04

BUDAPEST, April 15, 1993

TECHNICAL UNIVERSITY OF BUDAPEST

ISSN 1216-3015 (Technical Report, Ser. Electrical Engineering, on paper)
ISBN 963-421-509-2 (on paper)

ISSN 1216-9226 (Technical Report, Ser. Electrical Engineering, on microfiche)
ISBN 963-421-508-4 (on microfiche)

Editor of the Technical Report Series of the TUB:
I. Kollár
Periodica Polytechnica Secretariat,
H-1521 Budapest, Hungary
Telefax: + 36 1 166-6808

Reproduced in booklet form by the Printing Office of the TUB
Microfiche: Central Library of the TUB
Request for Technical Reports or a list of published Technical Reports:
Central Library of TUB
Department for International Exchange
H-1521 Budapest, Hungary
Telefax: + 36 1 181-2753, telex: 22-5931 muegy h

CENTRE ESTIMATION IN MARKER BASED MOTION ANALYSIS [1]

PhD Thesis
1993.

JOBBÁGY, Ákos

Department of Measurement and Instrument Engineering
Faculty of Electrical Engineering and Computer Science
TECHNICAL UNIVERSITY OF BUDAPEST
1521 Budapest, Hungary
Phone, fax: + 36 1 166 - 4938
e-mail: jobbagy@mmt.bme.hu

Abstract:
The majority of 3-D motion analyzers process the images acquired by cameras. In general feature extraction is necessary, which can be achieved by attaching markers to landmark points of moving objects and determine the position of these landmark points only. Usually spherical markers are used, and the centre of the sphere is regarded as the marked point. The real-time applications can afford only 1-bit A/D conversion of the acquired images, consequently the centre of a binary image must be determined to get the coordinates of a landmark point. As a result of the quantization the centre of a binary image cannot be uniquely determined.
Both resolution and accuracy depends on the number of pixels, covered by a marker image. Accuracy further depends on the method used to estimate the centre. It is shown that the conventional algorithms are not optimal, and new methods (BEWRI, ring-fitting) are introduced, which provide a more accurate estimation for the centre of a binary image. A further advantage of the ring-fitting method that it inherently gives a measure for the deviation of an image shape from the ideal circular one. The methods are compared using simulation programs.

Keywords: motion analysis, 3-D motion analyzers, binary image processing, centre estimation, measure for circularity, pattern recognition, simulation.

---

[1] The research work was done by the author partly as a research fellow at the Delft University of Technology, Faculty of Applied Physics.

Content

1. INTRODUCTION

Motion has long been in the focus of interest of both scientists and philosophers. The ancient Greek way of meditation was contradictory regarding its relation to motion: some denied the existence of any kind of motion, others had different opinion (Simonyi, 1978). Heraclitus had the idea that "everything moves" (pantha rei). The analysis of motion is greatly helped if it can be recorded. From the Greek philosophers to the Renaissance contributions to movement analysis were based on visual observation. Borelli, who lived in the XVIIth century, is considered to be the "father of biomechanics" - a brand new book on movement analysis devotes a whole chapter to him (Cappozzo et al., 1992). From the mid-nineteenth century several attempts have been made to record human and animal motion, the most important results are the following.

K.H.Vierordt attached ink nozzles to the patient and they left traces on suspended paper stripes. He published his results in 1881.

Helmholz's *kymograph* contained a rotating drum with soot blackened surface. The deflection of a pointer as a function of time could have been recorded. Its slightly modified version, the *myograph* was used by E.J.Marey, who recorded the wing-beat of a flying dove using pneumatic connection to this device in 1868.

The next milestone in recording motion was the invention of the ***photocamera***. Different methods were used which made possible to store the consecutive phases of motion with the help of still picture(s). E.Muggeridge (later Muybridge) used 12 cameras and trip wired shutters. Later he developed a rotary commutator for the electromagnetic release of the shutters and applied this method to 24 cameras. Named *serial photography* he recorded about 100,000 plates of animal and human motion in Palo Alto and later at the University of Pennsylvania. Based on his photographs soon results concerning normal and pathological gait were published.

Another solution was to use several pieces of photographic emulsion, which rotated with intermediate full stops. E.J.Marey used 12 pieces of photographic emulsion and reached 1/720 s aperture time in 1885. The first stick-diagrams can also be thanked to Marey, who used one plate and a rotating disk with some slits on it. To promote evaluation the moving person was dressed in black, the limbs marked by white lines, the joints and the head with shining buttons.

*In 1888 E.J.Marey invented the film-camera which he called **chronophotographic box**.* Two years later he could reach the 50 pictures/s speed and 1/4000 s aperture time.

The use of *flash light* for photography is due to W.H.F.Talbot, who applied it first in 1851. A 10 μs spark-gap discharge was derived from parallel Leyden jars.

Several improvements have been done which are described in (Furnée, 1989), where a more detailed summary can also be found regarding the beginning and history of motion analysis.

At present there are several types of motion analyzers, Fig. 1.1. is a possible classification of them. The shaded area defines the type, the dissertation concentrates on.

The contacting methods are valuable in the case of simple motion, e.g. one- or two dimensional displacement. The majority of applications requires the analysis of three dimensional motion. There are some sophisticated mechanical equipment - the goniometer is an example, see (Chao et al., 1980), (Oderkerk et al., 1991) - instruments based on non-contacting methods usually outperform them. These latter instruments process the images of cameras or PSDs (Position Sensitive Device). In

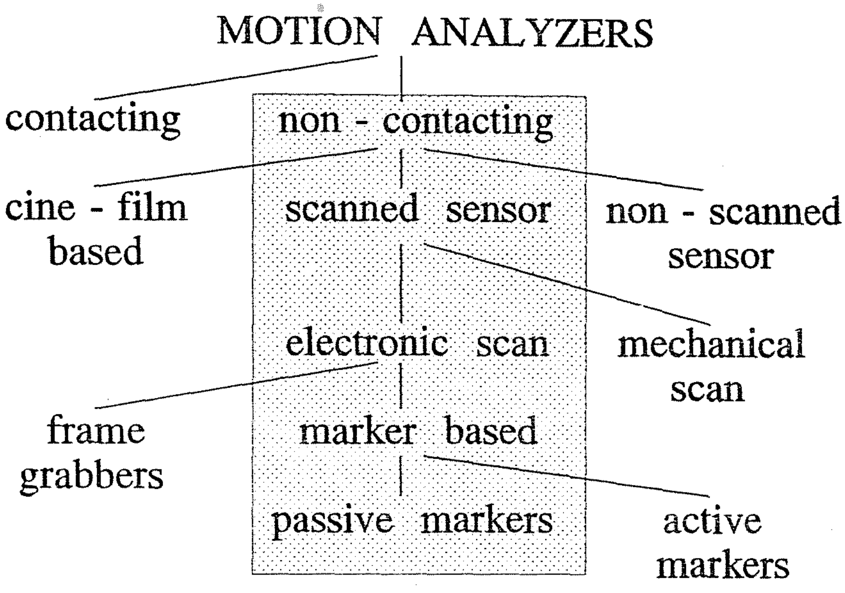

Figure 1.1. Classification of motion analyzers

general the information contained in the images is redundant, feature extraction is necessary. Feature extraction in software gives a flexible and universal solution but in this case the real-time operation is limited. There is another solution for feature extraction: to attach markers to landmark points of moving objects and determine the positions of these landmark points only.

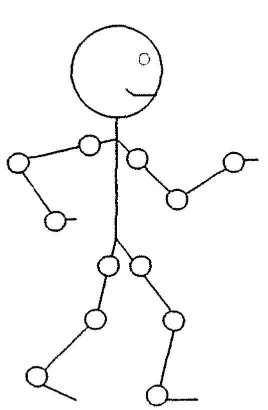

Figure 1.2. A rigid body model for human motion

Fig. 1.2. shows a popular rigid body model, used for human gait analysis. Markers are attached to landmark points. As the luminosity of a marker image is significantly higher than that of the ambient parts, feature extraction can easily be done on the basis of the video output signal of a camera. Sharp changes in the video output signal mark the border of the marker image. Hardware feature extraction is based on this. In 1967 at TU Delft a video/digital coordinate converter was developed, described in (Furnée, 1967). The solutions incorporated in this instrument can be found in its direct successor, the PRIMAS system, cf. (Furnée, 1989) as well as in several

derivative and alternative systems, cf. (Furnée et al., 1974), (Paul et al., 1974), (Bruegger et al., 1978), (Taylor et al., 1982), (Ferrigno et al., 1985) which in some cases have developed into commercially available systems. A review is given in (Walton (ed.), 1990). The TV based CINTEL system (Dinn et al., 1970) can be considered as a slightly different category. As it digitised the video signal on different reduced grids of image coordinates, it constituted a video frame grabber, at a time too early for industry to realise its potential. Alternative approaches using non-TV sensors of various categories were reported by (Lindholm et al., 1974), (Mitchelson, 1988), (Macellari, 1983), leading to systems which have also attained commercial application. The marker positions can be determined by mechanical scan as well. Mitchelson(1975) describes the prototype of such a system (CODA - Cartesian Optoelectronic Dynamic Antropometer) having one vertical and two horizontal scanners. Each scanner has a rotating mirror drum for light emission, the reflected light is split and projected onto a detector element, which triggers the readout of the angle of the drum. The main drawback is the mechanical movement of the drums, but three dimensional position determination is also problematic: in the general case the light beam of each scanner hits the marker when it is in a different position.

Doppler radar motion transducers, utilising ultrasound, are not generally able to track the motion of single points. However, there are applications, which fit well to these devices (Kemp et al., 1982).

Cine film based analyzers provide the highest sampling rate, 1000 frame/s is not uncommon, even 10 000 partial frames per second can be captured and stored using electronic shutters and multiple intensified imagers (Balch, 1991). Their main drawback is the digitisation process, which is necessary after the film is developed. Real-time application is impossible. (Mesqui et al., 1981) describes a computer controlled film analysis system based on a video dissector and image RAM.

Frame grabbers are rather popular and general purpose tools. If applied for motion analysis their software feature extraction would allow for limited real-time applications.

The resolution of a *Position Sensitive Device* is theoretically infinite. As the midpoint of one marker image is determined at a time, precise focusing is not required. It allows for a typical 8:1 maximum to minimum distance ratio, compared to the typical 4:1 of the CCD sensors. There are some associated problems however, that must be solved: the reflected light components degrade accuracy, the marker images must be separated and the ambient light as well as the reflections must be suppressed (Given, 1988). Only active markers can help to eliminate the aforementioned difficulties, and they introduce new ones. Active (light emitting) markers provide good separation (they are lit separately, one at a time or emit different frequency radiation) but require either wiring between the moving object and the equipment or a power supply and control circuitry to be attached to the object. Passive markers mean almost no discomfort for a human being or an animal consequently, they influence the motion of the object under test only negligibly. Their disadvantage is that the markers must be identified. Colour markers can solve this problem only if a few of them (usually 6) appear on the same frame.

If passive markers are used then the ambient light suppression can be increased with stroboscopic infrared illumination. Its efficiency can further be increased if the

markers are made of retroreflective material and the integration time of the CCD camera is reduced and synchronised to the illumination.
Motion analyzers play an important role in biomedical- and sport applications. Rehabilitation, prosthesis manufacturing and setting, (sport) training and sport goods design are the most important fields of application where mainly ***non-contacting, TV-based, three dimensional motion analyzers with passive reflecting markers*** are used. The dissertation will focus on this type of analyzers, concentrating on their resolution and accuracy. Both resolution and accuracy are influenced by the sensor element as well as by the marker size. If the image of a marker is projected onto only one pixel of the sensor CCD chip then the resolution and accuracy of measuring the position of the marker are determined by the number of columns (horizontally) and lines (vertically). If the image of a marker covers several elementary pixels then subpixel resolution and accuracy can be achieved by estimating its midpoint on the basis of all the covered pixels. The detailed explanation for the term *covered* will be given in Chapter 3. Simplifying the problem: the integrated charge of each elementary pixel is thresholded, the pixels having more charge than the threshold level are qualified as "covered" while the others as "not covered" or "uncovered". Hereafter the set of the covered pixels and of their uncovered adjacent pixels will be called ***binary marker image***. This term denotes a localised qualification: the adjoining covered pixels of a marker image and their neighbours. During the investigations generally single level thresholding of the video signal was supposed, i.e. qualification of the sensor image by a 1 bit A/D conversion. The effect of multiple level thresholding is mentioned where it is necessary and summarised in Chapter 5.
Deriving mainly from its simplicity by far the most popular centre estimation method is *geometric centroid calculation*. It is shown that this method may result in distorted estimation, depending on the actual pattern of the binary marker image. Another, less frequently used method is *circle fitting*. The circle must fit on the edge points of the image and the centre of the circle is the estimated midpoint. Although this method is theoretically able to find the centre point of a partly occluded marker image, provided the image on the sensor is an ideal circle, its accuracy is not better than that of geometric centroid calculation. My results show that the decisive factor, concerning resolution and accuracy, is the number of elementary pixels that are covered by the marker image. It follows that it is not worth searching for an *optimal geometry* of the sensor chip for the purpose of motion analysis. I also showed, that the conventional estimation methods can be outperformed.
I spent a year as a postdoctoral research fellow in the Motion Analysis Laboratory - led by Dr.Ir.E.H.Furnée - of the Delft University of Technology, Fac. Applied Physics. I had the possibility to carry out measurements with the PRIMAS PRecIsion Motion Analysis System. I have developed a model which is suitable for the qualification of elementary pixels as covered and uncovered to acquire the binary marker image if the centre of a marker image is given. I wrote simulation programs based on this model. The programs - written in Turbo Pascal - were run on IBM PC.
I studied the conventional estimation methods both in theory and in practice and I concluded that they can result in a distorted estimate because they neglect the fact, that the quantisation errors, occurring while qualifying the elementary pixels at the circumference of the image as covered and uncovered, are not independent of each

other. With a given radius the centre of a marker image may move along an area so that the same binary marker image result. I gave a method to calculate the theoretical limit of accuracy: if the centre of a marker image with known radius is within such an area then the median of the area is the best estimation, the expected value of the distance between the actual and the estimated centres of a randomly projected image is minimal. If the expected value of the squared distance between the actual and the estimated centres of a randomly projected image is to be minimised then the centre of gravity of the area should be selected as the estimate of the marker image centre. In practical cases the radius of the marker image is not known. It means that the same binary marker image can be caused by marker images of different radii. To each radius different area belongs. I gave a method to estimate the centre of a marker image without knowing its radius. The **BEWRI** (Best Estimate Without Radius Information) method renders to a binary marker image the weighted average of the centres of the areas belonging to different radii, the weighting factors are the areas. I worked out an algorithm which has an accuracy only slightly worse than that of the BEWRI method but requires much less computation, so it is appropriate for real-time applications. The ***ring fitting method*** gives the centre of the widest possible ring, that can produce the binary marker image as its estimated centre. Both the outer and the inner circles of the ring produce the given binary marker image if it derives from an ideal circular image. The method is extended to distorted images as well. In this general case the width of the ring is defined in the following way: the distance between the centre point and the farthest covered pixel is subtracted from the distance between the centre point and the closest uncovered pixel. This means that the width may also be negative, if the marker image is distorted. The negative width compared to the appropriate radius characterises the distortion: small value may result from noise, greater values may be caused by occlusion or overlapping. Calculations show that the ring fitting method gives approximately 30...40 % better accuracy than the conventional estimation methods in the case of most frequently used marker sizes, even with noisy marker images. The absolute value of the standard deviation is also more favourable as it decreases in the case of the most marker image sizes.

Chapter 2. depicts the most important elements of present-day marker based movement analyzers (markers, cameras, video/digital coordinate converters), outlines the necessary data processing and describes some representatives of the existing systems together with their typical applications. Chapter 3. gives a correct definition of resolution and accuracy of motion analysis. Based on this it is shown that the ratio of the neighbouring sides of an elementary pixel of the CCD sensor is irrelevant regarding resolution. The theoretical limit of accuracy is determined and the conventional centre estimation methods are evaluated by comparing their results to this limit. Chapter 4. introduces the BEWRI method for centre estimation, which gives far more accurate estimates than the conventional algorithms. Two possible realisations of the BEWRI method are also given. The maximum likelihood estimate of the marker centre is provided by the ring fitting algorithm. This algorithm inherently provides a measure for the deviation of the image from the ideal circular form. Chapter 5. summarises the measurements made with the conventional and the devised methods and shows the possible applications on other fields. The dissertation ends with a list of references.

I consider the following as my most important results:

- It has been proved that the resolution of marker centre estimation is primarily determined by the number of 'covered' pixels, but the relationship is not monotonous. The tendency is that the more pixels are covered the better is the resolution. However, contemplating small changes, the relationship might even be opposite. It has been shown that the shape of the elementary pixel - the ratio of its vertical and horizontal sides - has only a negligible effect on the resolution compared to the number of covered pixels.

- The theoretical limit of accuracy has been determined. It can be achieved if the radius of the marker image is known. To each binary marker image the centre of gravity of that area is rendered, within which the centre of the image with known radius might be anywhere to cause the given binary marker image.

- It has been shown that the conventional methods of centre estimation are not optimal regarding the accuracy. The reason is that they neglect the fact, that the quantisation errors along the circumference are not independent from each other.

- A method has been worked out which gives an optimal estimate for a binary marker image regarding the accuracy without knowing the radius of the covering image (BEWRI method). The same way as described for the theoretical limit of accuracy areas are determined for the whole possible range of radii as if they were fixed and known. The centre of gravity of these areas are determined and the weighted average of these centres are calculated, the areas being the weighting factors. The method gives the minimal expected value of the squared deviation of the estimated centre from the actual one, provided the marker image is randomly projected onto the surface of the sensor with a randomly selected radius, and the distributions are uniform. It must be emphasised that BEWRI minimises the *expected value* of the squared deviation between the actual and the estimated midpoints of a circular image when only the binary marker image is given. A binary marker image can be produced by circular images of different radii, BEWRI accommodates to the practical case, i.e. the actual radius of the image is unknown.

- Two realisations of the BEWRI method has been worked out, the MAXARE and the AVRAE methods. They approximate the accuracy of BEWRI but require less computation.

- The ring fitting algorithm has been devised, which gives the maximum likelihood estimate of the marker image centres. The input data of the algorithm is a binary marker image, i.e. no actual radius information is needed. This algorithm inherently provides a measure to characterise the distortion of circular shapes from the ideal one.

2. MARKER BASED MOTION ANALYSIS

In this chapter I give a description of marker based motion analyzers, mainly of those using scanned sensors.

2.1. MARKERS

In general motion analysis requires an appropriate model and measurements are carried out according to it. If the model is a rigid body based one then landmark points of the moving object can be designated so that knowing the trajectories of these points fully describes the motion. The important points can be tracked if markers are stuck to them. Markers are *carriers* then, after acquiring a picture, only the midpoint coordinates are important, provided the midpoint always means the position of the corresponding landmark point.
The marker images are excessively bright thus providing a means for feature extraction: thresholding the luminosity of the whole frame the marker images can be separated from their surroundings.
There are basically two types of markers, active and passive ones. ***Active markers*** have their own light. Their advantage is that the identification of a marker is easy, it is possible to light only one marker at a time. With active markers PSD (Position Sensitive Device) sensors can also be used. These sensors utilise the lateral photoeffect, which was first mentioned by Schottky. The first PSD, being able to locate the source of incident radiation, was described by the Swedish scientist Wallmark. Woltring(1975) analyzed the different realisation possibilities and showed that the relation between the position of a single light spot on the sensor surface and the output signal (distribution of currents) can be linear. The PSD sensor has a theoretically infinite resolution, but the light sources must be separated either in time or in frequency. Active markers can be used with scanned sensors as well. The disadvantage of active markers is that they require either their own power supply and control circuitry or wiring that connects them to a control unit. Investigating human or animal motion is influenced, no matter which of the two possible solutions is chosen.
If the active markers are lit separately, one at a time, this means that their positions are not measured at the same time instant. The compensation of this time skew requires substantial computation, so real-time applications can't afford it.
The "midpoint" of an active marker depends on the radiation characteristics and also on the angle between the camera axis and the main axis of the light source. This is an error source especially in three dimensional applications, when the markers are tracked from different directions.
Passive markers have the important advantage that they mean almost no discomfort for the human or animal, as they are lightweight ($\leq$ 10 gram) and need no wired connection. The form must be selected so that its projection to the sensor plane have always the same shape. It follows that the marker shape should result in a circular projection: spherical shape is needed for three dimensional applications, hemispheres and disks are also satisfactory for two dimensional use. The relative brightness of markers compared to their environment (it also can be expressed as ambient light suppression) can be increased in two ways: the cover of a passive marker is made of retroreflective material and a stroboscopic infrared illumination is applied. (The illumination will be detailed in 2.2.) The retroreflective cover has a further advantage: even if the marker is (hemi)spherical, the luminosity of its image is close to uniform.

The usual illumination is mainly parallel with the camera axis so its angle to the normal of the marker surface is between 0° and 90°. The reflective efficiency, i.e. the luminance factor as a function of the observation angle is available for a retroreflective material. As an illustration, the reflection from a Scotchlite retroreflective material can be approximately 20 times better compared to a white diffuse background. As white skin tone is 4 times below white diffuse background, almost 100 times "gain" can be achieved putting Scotchlite marker on white skin. If disks are used, ±60° rotation of the marker plane to the TV camera lens axis doesn't result in a high change in luminous intensity (Andrews, 1982).
The processing of a frame, containing several marker images, must start with *clustering*: if two or more markers cover parts of the same line of the sensor then their segments will come interlaced (section 2.4. explains the details).
The main drawback of passive markers is that they need to be identified. As a result of motion the relative positions of the markers may change. Several predicting algorithms exist which, on the basis of previous (or subsequent) positions are all able to specify a small window, so that the marker image must be within that, e.g. (Furnée, 1990). Unfortunately these algorithms scarcely help when identification is really problematic: if the traces of two markers cross each other, near the crossing point the corresponding two windows will cover about the same area. Identification is even more difficult if the marker image is totally occluded for some time. There are off-line methods suggested for this, e.g. (Taylor et al., 1982).
When the marker image is a circle its centre is considered to be the "midpoint", i.e. the point the position of which we are interested in. While processing marker images the problem of partly occluded or overlapping marker images must be taken into account.

2.2. CAMERAS

In marker based motion analysis a camera may consist of the following parts:

- light source for illumination,
- optical lens(es),
- shutter,
- light sensor,
- interface circuitry.

The aim is to get a picture, on which the luminosity of the marker images is uniform and equal, at the same time much greater than the environment and all the markers are sampled simultaneously. This aim cannot be achieved in general but might well be approximated with restrictions that can usually be fulfilled in practical applications. The most important restriction is that the markers remain within a defined volume. The smaller is this volume the better the aforementioned aim can be approximated. One camera gives a two-dimensional picture. The actual size of the plane it sees, the Field Of View (FOV) depends on its distance from the camera. When passive markers are used then the relative brightness of their image can be increased by covering them with a reflective material and applying an illumination, the frequency of which is close to that on which the reflectivity of the cover is maximal. This frequency should be outside the visible spectrum. Generally the infrared region is the optimal selection.

The best *illumination* would be uniform along the field of view of the camera. If markers might be present anywhere within a substantial volume then the radiation characteristics of the light source cannot be neglected. In the majority of cases infrared emitting diodes (IRED) are used, which have an ellipse-like characteristic on a polar diagram. The IREDs are best placed around the camera lens in concentric rings. It is possible to optimise the angle between the optical axis of each diode and the optical axis of the camera in order to get constant intensity along a perpendicular plane. It is advantageous when the markers are in such a plane during the analysis. This problem was dealt with at TU Delft and it is proved that a better result can be achieved compared to the situation, when all the diodes are placed in parallel (Toet, 1991). To complete the task the scatter diagram of the retroreflective material should also be considered. The conclusion is that properly placing the diodes around the camera lens and deflecting them with the appropriate angle from the camera axis assures a quasi constant intensity across the field of view, being at a given distance from the camera. Moreover, as the distance increases, the average reflective efficiency of the marker covering material also increases if the field of view is constant. The reason is that the maximal angle between the camera axis and the border lines of the FOV decreases, which means a more effective reflection compared to the surroundings, partly compensating for the decreasing intensity resulting from the increased distance (Furnée, 1984). In practical cases this means that for different distances different illuminator arrays should be used. The *optical lens* might also be changed according to the required field of view.
The luminosity of an image depends on the amount of light, perceived by the camera and also on the aperture time, the time interval, during which the light affects the sensor element. The ambient light suppression can be substantially increased if the aperture time is only a fraction of the time that elapses between two consecutive frames, while the light reflected from the markers remains constant. It can be achieved by *shuttering* and *stroboscopic illumination,* synchronised to it. This solution has a further advantage: assures equidistant and simultaneous sampling.
Early TV-based systems had cameras with mechanical rotary shutter. Since CCD sensors are available, the shuttering function can be realised electronically by reducing the integration time. As an example, the HTH MX type measurement quality cameras run with 100 Hz and their integration time is 0.1 ms in harmony with the 100 μs duration infrared illumination pulse.
The first *sensors* were electron tubes like Vidicon or Plumbicon. They were vulnerable, had substantial nonlinearity along the surface and the dependence of their output signal on temperature was not negligible. Present day sensors are almost exclusively solid state imagers. They all exhibit precise geometry and small temperature dependence. There are different types with subtle differences effecting the geometry (layout), the read-out, the sensitivity and the noise. The three basic types, the interline sensor, the X-Y addressed MOS sensor and the frame transfer sensor are detailed in (Collet, 1985).
I give a short summary of the frame transfer sensors (FT), because they are widely used in cameras produced for motion analysis.
Fig. 2.1. shows the basic structure of an FT sensor. During the integration period each cell (pixel) generates some charge, which is proportional to the light intensity,

affecting it and to the integration time. During vertical blanking the charge pattern of the imaging section is transferred into the storage section which is shielded in order to exclude any further modification of the charge pattern. The horizontal blanking periods are utilised for shifting this charge to the horizontal shift register (one line at each blanking). The video output signal is composed by clocking out this shift register. The photosensitive cells can further be divided into 4 parts as shown in Fig.2.2. The operation of a part can be controlled by the voltage applied to the corresponding gate electrode. The layout of the sensor must be investigated as it influences the results in two respects. The ratio of the vertical and horizontal sides must be taken into account when the possible coverage of the binary marker image by circular shaped pattern is examined. The sensor layout also influences the active surface of a pixel. The interleaved operation is unusual in motion analysis as it would result in a virtual modulation of the markers, which must be avoided. The non-interleaved operation reduces the active surface of a pixel as it is explained in the following.
Each gate can be enabled or disabled, which is necessary for the charge transfer. The separate enabling allows the interlaced operation: during the odd fields Φ_4, Φ_1 and Φ_2, during the even fields Φ_2, Φ_3 and Φ_4 are enabled. As an example the NXA 1011 from Philips has 288 effective lines and in each line 604 elementary cells (Feddern et al., 1984). The total area of this chip is 66 mm^2, the size of a cell is 10 μm (horizontal) x 15.6 μm (vertical). The colour version of this sensor is described in details by (van de Steeg et al., 1985).
In motion analysis the interlaced operation might cause an undesired modulation

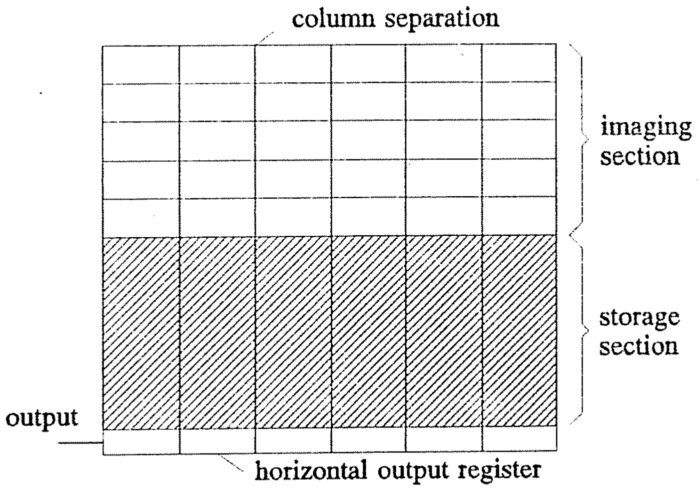

Figure 2.1. The schematic structure of the frame transfer sensor.

so it is advisable to avoid interlacing. The non-interlaced operation means that one fourth of a pixel surface is always inactive during the integration, because either Φ_4, Φ_1 and Φ_2 or Φ_2, Φ_3 and Φ_4 are enabled during imaging both in the odd and in the

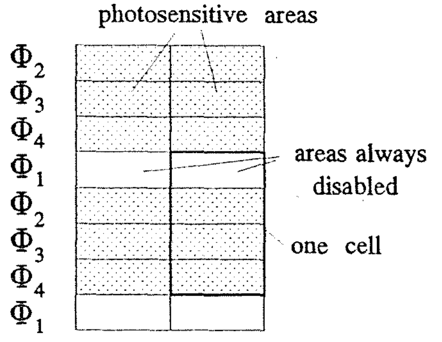

Figure 2.2. One cell of a frame transfer sensor is divided into 4 parts.

even fields.
The *interface circuitry* receives the clock signal and the control signals for the illumination and integration and drives the output video signal.

2.3. VIDEO/DIGITAL COORDINATE CONVERSION
The name originates from the era when electron tubes were the sensors in video cameras. The converter is considered to be the key element while developing on-line real-time motion analyzers. Furnée(1967) reports one of the earliest applications. The task of the converter is to extract the marker images from a picture. It is done by thresholding the video signal: above threshold level signals the presence of a piece of a marker image. The marker image is divided into pieces called *segments*, cf. Fig. 2.3. The segments can be fully determined by two data: specifying the coordinates of a given point (usually the endpoint) and the width is most common.

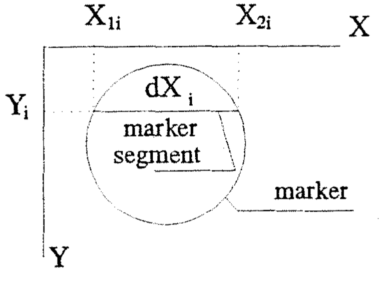

Figure 2.3. Marker segment definition in general.

In case of an electronic tube the vertical coordinate of a point is determined by its line number, the horizontal coordinate is the position within that line. Two counters can be applied which show the x,y coordinates of the scanning beam. Both counters are

reset with the vertical synchronising signal. The vertical position counter is clocked by the horizontal synchronising signal, which resets the horizontal position counter. The latter requires an extra clock signal to measure the position within a line.
The method can be applied to CCD sensors by omitting the horizontal clock generator. The converter designates the coordinates of an elementary pixel. Fig. 2.4. shows the definition of segment in case the marker image is on the surface of a CCD sensor. The video/digital coordinate converter gives the coordinates of the CCD pixel (or a part of the scanned line in case of electron tubes) to which the actual value of the video output signal belongs.
Present day video/digital coordinate converters use mainly one-level thresholding. When the video signal increases above the threshold level, the corresponding pixel (part of a line) is considered to be the starting one of the segment. Similarly, when the video signal decreases below the threshold level, the corresponding pixel (part of a line) is the last one of the segment.

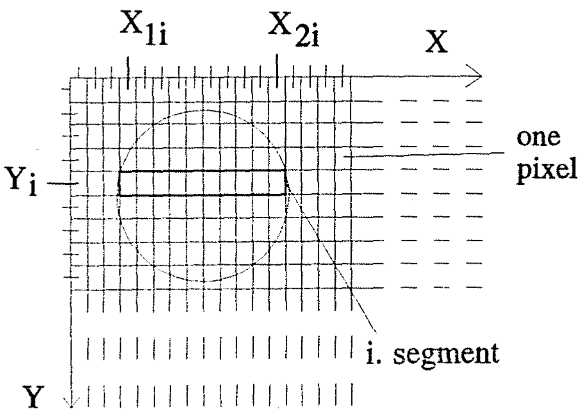

$$dX_i = X_{2i} - X_{1i} + 1$$

Figure 2.4. Marker segment definition using solid state sensor.

Multiple level thresholding would result in a smaller quantisation error but at the same time would considerably increase the computational demand.

2.4. DATA PROCESSING

In marker based motion analysis, as it was mentioned in section 2.1., markers are used as "carriers". In conformity with it, I divide the data processing into two parts: I call *low level data processing* what is required to get the coordinate values of the points, which are marked. The second part is the processing independent of the markers: lens distortion compensation, point identification, tracking and user specific algorithms. Low level data processing has to solve two tasks: *segment clustering* and *centroid estimation*. These tasks are usually performed by a dedicated *real-time* *marker segment processor.* Its output data are one x,y coordinate pair per marker on each frame, hopefully the coordinate value of the marked point in the perpendicular plane.

Segment clustering

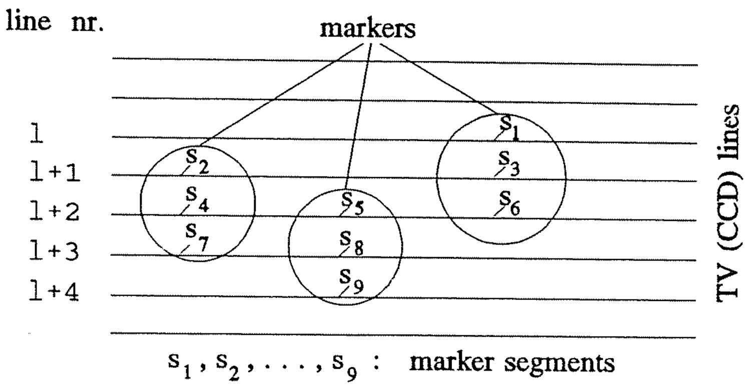

Figure 2.5. Marker images on a sensor surface.

Fig. 2.5. shows a marker arrangement when two or more marker images have segments in the same line. The segments will arrive interlaced in time, the ones belonging to the same marker are: $\{s_1, s_3, s_6\}$, $\{s_2, s_4, s_7\}$ and $\{s_5, s_8, s_9\}$. The clustering algorithms can make use of the facts that:

- only one segment of a marker can have a given Y coordinate,
- for the consecutive segments of a marker $Y_i^{(m)} + 1 = Y_{i+1}^{(m)}$, where m denotes the *m*th marker and i denotes the *i*th segment of the *m*th marker.

In Fig. 2.5.:

(s_1):	$Y_1^{(1)} = l$	(s_2):	$Y_1^{(2)} = l+1$	(s_5):	$Y_1^{(3)} = l+2$
(s_3):	$Y_2^{(1)} = l+1$	(s_4):	$Y_2^{(2)} = l+2$	(s_8):	$Y_2^{(3)} = l+3$
(s_6):	$Y_3^{(1)} = l+2$	(s_7):	$Y_3^{(2)} = l+3$	(s_9):	$Y_3^{(3)} = l+4$

The first clustering algorithms used to be serial regarding the order the markers were processed: in order to gather the segments belonging to a given marker all the segments were tested and this process was repeated for each marker. Segments could have been excluded from the search on condition that they had already been processed and there had been at least one empty line following them which separated the processed and unprocessed markers. This method was inherently slow.

The clustering method we have been applying (Jobbágy et al., 1991) evaluates each segment only once. Its first version clustered on the basis of the line number and the (transformed) midpoint value of the segment, added to a cluster for the last time. These values are called **last Y_m** and **last X_{m0}** respectively. The midpoint of a segment is $(X_{1i}+X_{2i})/2$. In order to get always an integer value a transformation is used:

$X_{0i} = 2 * [(X_{1i}+X_{2i})/2] = 2 * X_{2i} - dX_i$. A segment was added to a cluster if both

$$Y_i = \text{last } Y_m + 1 \quad (2.1).$$

and

$$|X_{0i} - \text{last } X_{m0}| < \epsilon \quad (2.2)$$

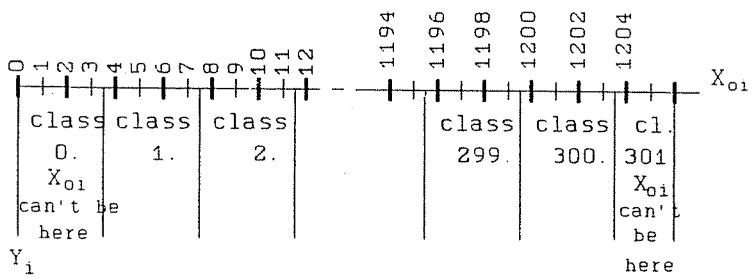

Figure 2.6. The definition of classes for clustering.

were true. Processing a new segment started with comparing its Y_i to the last Y_m values of active clusters and if (2.1) was fulfilled then (2.2) was also tested. If both (2.1) and (2.2) were not fulfilled for any of the active clusters then a new cluster had to be

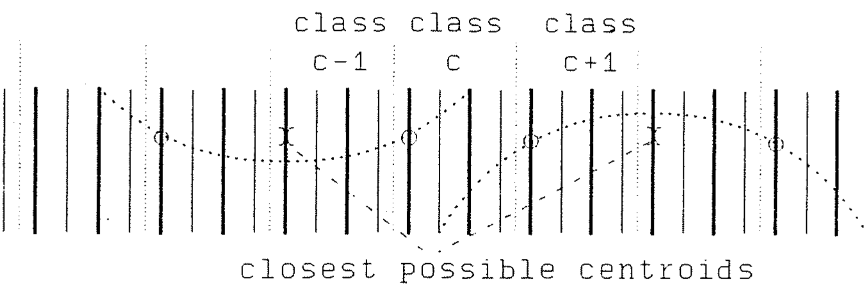

Figure 2.7. Clustering marker segments.

opened. The efficiency of this version can be increased if those clusters that surely will not have more segments are closed: the segments will not be tested against the last Y_m and last X_{m0} values of the closed clusters. If $Y_i >$ (last Y_m+1) then the *m*th cluster can be closed.
The new version of this algorithm eliminates the time consuming loop of trying to fit a segment to all the active clusters. While processing a segment we make use of the

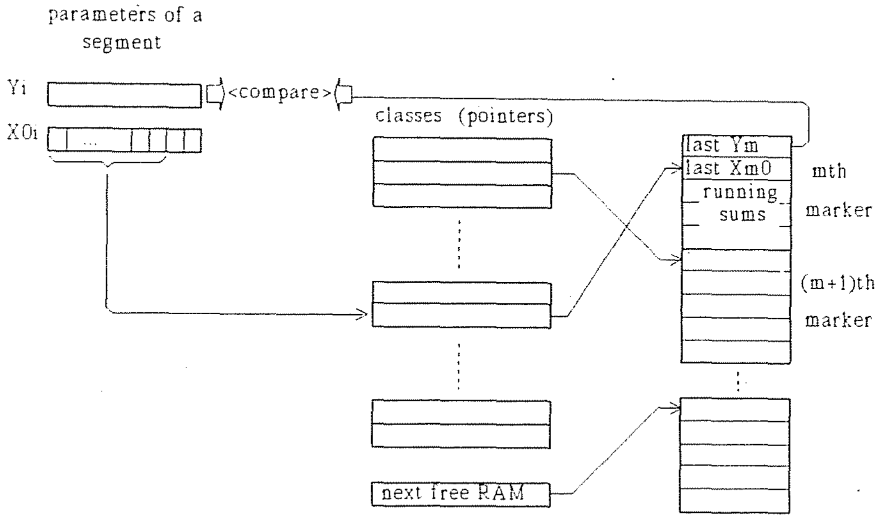

Figure 2.8. The block diagram of a fast clustering algorithm

fact that it can belong only to clusters with 'last X_{m0}' being close to X_{0i}. It means that the *clusters should be ordered according to their 'last X_{m0}' values.* The image field is divided horizontally into classes so that to each class (together with its right and left adjacent classes) the segments of only one marker can be related to at the same time. If the minimal segment width is e.g. 4 pixels (in order to exclude spurious signals) then to a CCD sensor having 604 columns 302 classes belong. The X_{0i} of a segment can be neither in the leftmost nor in the rightmost class. Figures 2.6. and 2.7. illustrate the classification.In these figures bold lines indicate physical columns (CCD pixels). The extra columns drawn by normal lines are needed as a result of scaling of X_{0i} only. Fig. 2.7. shows the situation when the segments of two circular markers are as close to each other as possible on condition that the minimal segment width is 4 pixels. The algorithm performs the $|X_{0i} - \text{last } X_{m0}| < \epsilon$ evaluation by searching in the class where X_{0i} points to and in its right and left neighbours. If the first segment of a marker must be put in a class where the data of a previous marker are present then the estimated centre coordinates of the previous marker are calculated and the marker data are replaced by the data of the new segment. The decision that it is a new segment and does not belong to the previous marker is done by comparing Y_i to (last Y_m). When all the input segments have been processed then the classes must be tested whether or not they contain a marker. (This test can be combined with clearing the classes.) This overhead is constant in time which results in a proper accommodation of the algorithm to the number of markers to be processed on a frame. If there are a great number of markers to be processed then the efficiency of the algorithm is high and if the number of markers to be processed is small then the worse efficiency is affordable. While realising the algorithm we used

an ordered chain solution which eliminates the need for testing the classes after the clustering is ready and reduces the memory requirements as well. (Only the clearing of the classes - pointers -remains as an overhead.) The classes contain only pointers which address memory segments designated to markers (see Fig. 2.8). As a result the data (last Y_m, last X_{m0} and running sums for centre estimation, see later in this section) related to markers are placed in memory consecutively requiring minimal storage capacity and providing convenient post-processing after clustering. The price to be paid for these advantages is the need for indirect addressing. The pointers must be reset before starting to process the segments of a new frame: they are set to point to the parameters of a dummy marker having so great value (511) for last Y which can never come from the video/digital coordinate converter. When the first time the X_{0i} of a segment selects a pointer it addresses this dummy marker and the comparison of Y_i to last Y_m shows that this segment does not belong to the (dummy) marker but it is the first segment of another marker. A detailed analysis of the clustering methods, based on measurements using different marker configurations is given in (van Veenendaal, 1992).
The marker image in practice usually deviates from an ideal circle. The reason is noise and occlusion, the resulting image is called 'distorted'. If the occluding object is a marker itself then we speak of overlapping. Clustering distorted markers may result in false solutions. Fig. 2.9. demonstrates that a marker can be split into two (a, b) or two overlapping markers can be split into three (c). In Fig. 2.9. the midpoints of the segments, X_{0i}, are marked by vertical bars. If the clustering condition is changed that may result in a different solution. Consider the following rule: a segment is added to a cluster if for its Y_i value:

$$Y_i + 1 = \text{last } Y_m \tag{2.3}$$

is true **and** the segment has overlapping X coordinates with the segment last added to the cluster:

$$X_{1i} < X_{2(i-1)} \quad \text{and} \quad X_{1(i-1)} < X_{2i} \tag{2.4}$$

Clustering according to this rule does not split the markers in Fig. 2.9a) and b) but takes the overlapping markers of c) as if they were one marker.
The present motion analysing systems generally offer (post processing, **not** real-time) programs containing tracking algorithms which estimate the position of each marker on a frame on the basis of the preceding n frames. (Jarrett, 1976), (Ferrigno et al., 1988) and (Downs et al., 1990) describe different tracking algorithms. Some of these can correct the distorted or missing estimates of the midpoint coordinates of the split, stuck or occluded markers. However, research work continues to implement clustering and midpoint estimation of distorted markers on a frame in real-time, independently of other frames. In section 4.4. a measure of distortion will be

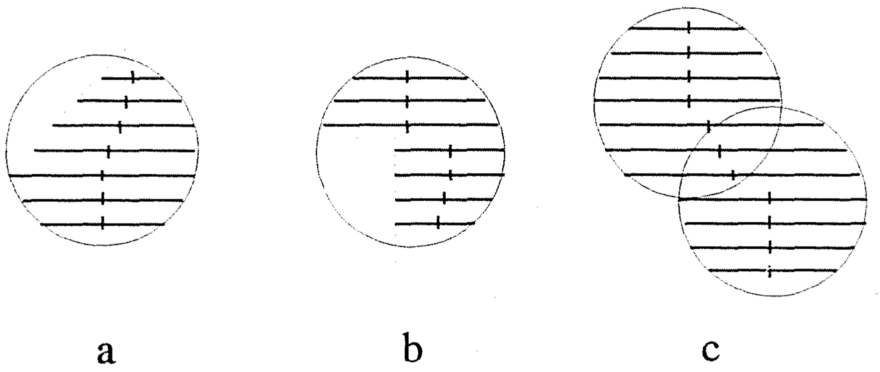

Figure 2.9. The segments and segment midpoints of distorted images.

introduced, which greatly helps to deal with this problem.

Centroid estimation

Centroid estimation means to search for the possible midpoint of a marker image. If the image of a marker is projected onto only one pixel of the CCD sensor (see Fig. 2.10a.) then the resolution and accuracy of measuring the position of the marker are

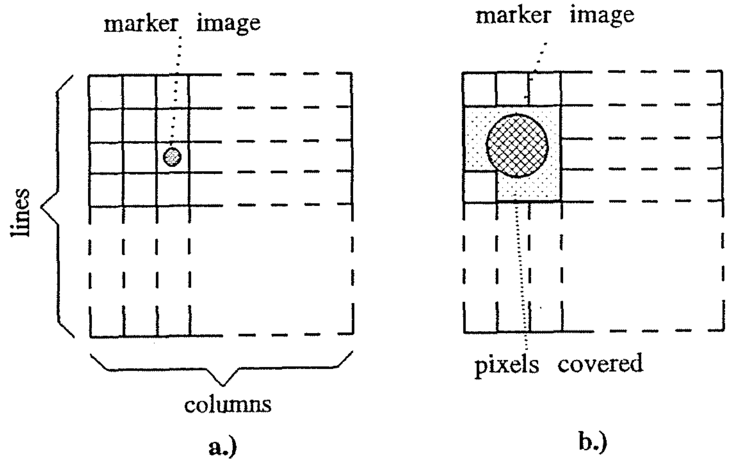

Figure 2.10. Marker images of different size projected onto the surface of a CCD sensor.

determined by the number of columns and lines. If the image of the marker covers several elementary pixels (see Fig. 2.10b.) then subpixel resolution and accuracy can

be achieved by estimating the midpoint of the marker image on the basis of all the covered pixels, i.e. the *binary marker image*.
While giving a description of the estimation methods the marker image on the surface of the CCD chip is considered to be an ideal circle with uniform luminosity (cf. Fig. 2.11). The related simplifications do not substantially diminish the generality of the results as it is shown in Chapter 3.

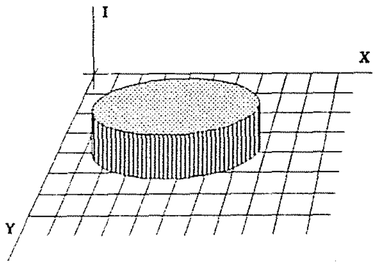

Figure 2.11. The simplified intensity distribution of a marker image.

Motion analyzers most frequently use **geometric centroid calculation.** Let us denote the coordinates of the pixels, covered by the marker image by (x_j, y_j), $j = 1...N$, where x stands for the *x*th column and y for the *y*th line. The coordinates of the geometric centroid are:

$$X_{0g} = \frac{1}{N}\sum_{j=1}^{N} x_j \,, \quad Y_{0g} = \frac{1}{N}\sum_{j=1}^{N} y_j \tag{2.5}$$

These coordinates can be calculated on the basis of the segment data as well (cf. Fig. 2.4.):

$$X_{0g} = \frac{\sum_{l=1}^{L} (X_{2l} - \frac{dX_l}{2}) dX_l}{\sum_{l=1}^{L} dX_l} \,, \quad Y_{0g} = \frac{\sum_{l=1}^{L} Y_l dX_l}{\sum_{l=1}^{L} dX_l} \tag{2.6}$$

where L is the number of segments, belonging to the binary marker image.
It must be emphasised that (2.5) and (2.6) are **equivalent.** The width dX_l of a segment equals the number of pixels covered by that segment, and as a result the denominator in (2.6) equals the total number of pixels covered, N. The expressions

in the argument of the summation of the numerators in (2.6) equal the sum of x and y coordinates of the pixels in the ith segment. Of the two equivalent expressions (2.6) fits much better to processing segments.
The method is generalised in (Jobbágy et al., 1991). The estimate of the marker image centre coordinates, $X_{0g}^{(n)}$, $Y_{0g}^{(n)}$ using the weighted averaging of the segment data is:

$$X_{0g}^{(n)} = \frac{\sum_i X_{0i} W_i}{\sum_i W_i} , \qquad Y_{0g}^{(n)} = \frac{\sum_i Y_i W_i}{\sum_i W_i} \tag{2.7}$$

where Y_i, X_{0i} are the parameters of the *i*th segment of a marker and $W_i = (dX_i)^n$ is the weight related to it. If $n=1$ then we get the conventional geometric centroid estimation method. The sensitivities of $X_{0g}^{(n)}$ and $Y_{0g}^{(n)}$ have been analyzed to the segment widths. The change of the width of the *i*th segment influences the change of $Y_{0g}^{(n)}$:

$$\Delta Y_{0g}^{(n)} = \frac{\partial Y_{0g}^{(n)}}{\partial (dX_i)} \Delta dX_i \tag{2.8}$$

where

$$\frac{\partial Y_{0g}^{(n)}}{\partial (dX_i)} = \frac{Y_i \sum_i W_i - \sum_i Y_i W_i}{(\sum_i W_i)^2} \frac{\partial W_i}{\partial (dX_i)} \tag{2.9}$$

The first term is the smaller the closer Y_i is to $Y_{0g}^{(n)}$. If $Y_i = Y_{0g}^{(n)}$ then the width of this segment does not influence $Y_{0g}^{(n)}$ at all as according to (2.7) the first term of (2.9) is zero. In the case of a marker, the segments of which are the wider the closer they are to the centre (which is the case with circular markers without overlapping or occlusion) it means that the change in the width of a wider segment has smaller effect on $Y_{0g}^{(n)}$ than a change in the width of a shorter segment. It is a disadvantage of linear weighting. Using higher powers of dX_i as W_i increases the second term in (2.9) when a segment is wider but does not help if $Y_i = Y_{0g}^{(n)}$. For $X_{0g}^{(n)}$ the situation is different as:

$$\frac{\partial X_{0g}^{(n)}}{\partial (dX_i)} = \frac{X_{0i} \sum_i W_i - \sum_i X_{0i} W_i}{(\sum_i W_i)^2} \frac{\partial W_i}{\partial (dX_i)} \tag{2.10}$$

According to (2.10) the sensitivities of $X_{0g}^{(n)}$ to the segment widths are **zero** if the segments give the same estimate for $X_{0g}^{(n)}$.

The generalised method was investigated with simulation, the characteristics of the simulation were the same as described in Chapter 3. The overall accuracy of the centre point estimation did not increase when the weights were $(dX_i)^2$ or $(dX_i)^3$ compared to linear weighting. Figures illustrating this are given in Chapter 3 following the description of the simulation process together with the applied models. As a consequence, in the general case while applying weighted averaging the linear weighting is recommended because it requires the minimum number of computations. **Circle fitting** can be used to estimate the midpoint of a marker image if the image is circular. In this case the midpoint is the centre of the circle. The circle must fit on the edge points of the image: on the first and last pixels of the segments. The circle fitting is done by using least-squares fitting method. Real-time operation requires the modification of the inherently non-linear procedure: the elimination of iterations. The solution we used is based on a

modified error function (EF) to be minimised:

$$EF_2 = \sum_i [(X_{0c} - X_i)^2 + (Y_{0c} - Y_i)^2 - R^2]^2 \qquad (2.11)$$

instead of the classical

$$EF_1 = \sum_i [\sqrt{(X_{0c} - X_i)^2 + (Y_{0c} - Y_i)^2} - R]^2 \qquad (2.12)$$

where X_i, Y_i are the endpoints of the segments: (x_{1i}, y_i) and (x_{2i}, y_i) for the *i*th segment, R is the radius of the fitted circle. The procedure is described in details in (Chernov and Ososkov, 1984) and in (Moura and Kitney, 1991). As an error function, it is possible to use the *maximal deviation* of the points from the circumference. The disadvantage of the application of this error function is that its minimisation is an iterative process. When using the circle fitting method the features of the primary sensor, the CCD chip must also be analyzed. The CCD sensor, applied in the HTH cameras, mentioned in section 2.2. has an elementary pixel size of 10 μm (horizontal) by 15.6 μm (vertical). It means that the image of a circle covers more columns than lines, cf. Fig. 2.12. This fact must be compensated for before circle fitting!
When circle fitting is used the circumference must be close to the edge points of the binary marker image. It is evident, that including inner points while computing the value of the EF_1 or the EF_2 error function must be avoided as they could bias the fitting of a circle. Selecting the endpoints of the segments seems to be a good solution. However, this procedure for contour point extraction introduces an undesirable asymmetry. Having selected the contour points, the circle fitting algorithm considers each point with the same weight. Consequently, if we select different contour points of the same set of covered pixels, the resulting estimate might also be different.
Fig. 2.13. shows a binary marker image and the same image rotated clockwise by 90 degree. Those pixels are hatched in both binary images which will be extracted if the endpoints of each segment are selected for extraction. In both sets black rings mark

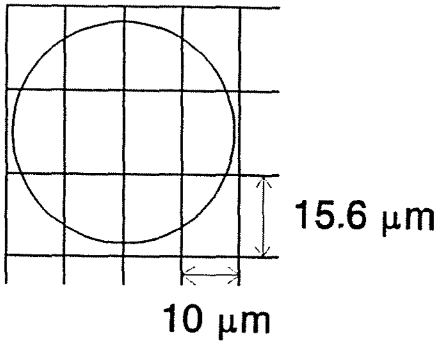

Figure 2.12. Circular image on the surface of the NXA 1011 CCD sensor.

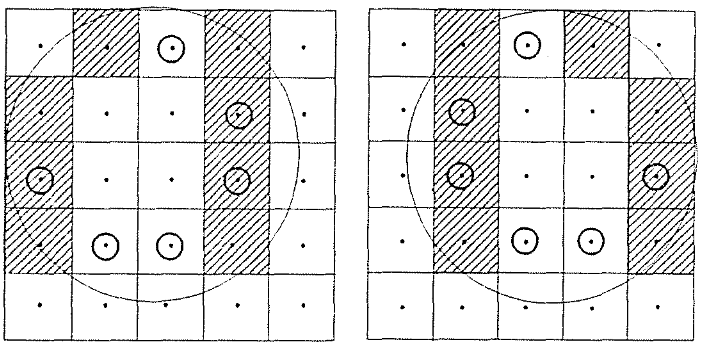

Figure 2.13. Centre estimation with circle fitting. The horizontal and the vertical accuracies are different even in the case of square shaped pixels.

those pixels which are differently evaluated as a result of the rotation: they will be extracted from the original set and will not be extracted from the rotated one or vice versa. The symmetry might be achieved if all the pixels in the top and in the bottom segments are selected for curve fitting. However, this symmetry does not improve the accuracy.

Different template matching techniques can also be used for centre estimation, especially if the video signal is digitised with a several bit A/D converter.

The low level data processing gives the marker centre coordinates in two dimensions for each camera. The most frequently used general purpose algorithms utilise these centre coordinates and aim at camera calibration.

Camera calibration
Camera calibration is necessary to reconstruct three dimensional coordinates on the basis of two dimensional images, taken at the same time by at least two cameras of the marker. Several algorithms exist which solve this problem, the Direct Linear Transformation (DLT) is the most frequently used one. Although the idea had been published long before in the field of photogrammetry (Das, 1949), the name derives from (Abdel-Aziz and Karara, 1971). A point on a 2D photograph determines a line. Sufficiently placed, at least two cameras provide spatial coordinates. If a coordinate system is determined by 3 points, attached to a rigid body, then its actual position can be expressed by giving three rotations (around the 3 axis) and a displacement. Camera calibration requires some reference points with known coordinates. Based on their measured coordinates the transformation constants are calculated. After calibration it is even possible to reconstruct three dimensional positions of rigid bodies using a single camera (Miller et al., 1980) but the accuracy is much better if more cameras are suitably placed. The modified DLT algorithm (Hatze, 1988) gives better accuracy but requires substantially more computation.
An alternative calibration is Simultaneous Multiframe Analytical Calibration (SMAC) described by (Woltring, 1980). To get three dimensional coordinates the set of cameras must be calibrated taking into account not only the external parameters (the position of cameras in space) but also the internal ones (scaling, shifting, distortion). The disadvantage of DLT that it requires a calibration object covering the *volume* to be measured! In human gait analysis it is some m^3! SMAC is based on taking pictures of a plane (placed in different orientations with respect to the cameras) having a lot of control points with accurately known positions. (Sabel, 1990) reports a SMAC realisation in motion analysis with a three dimensional accuracy of 1:4000 rms. (Borghese and Ferrignc, 1990) applied the classical iterative least-squares method for 3-D coordinate reconstruction based on 2-D images, supplied by at least two cameras.
Other high level algorithms are application specific. Usually displacement, velocity, acceleration and jerk parameters are calculated. Resulting from the noise and the finite resolution and accuracy, the higher derivatives of displacement are calculated, the worse are the results, because of the increasing Noise Amplification Factor, NAF. Different filtering techniques are necessary to obtain acceptable results (Andrews, 1982). (Fioretti et al., 1990b) investigates possible numerical differentiation procedures that are applicable for the in vivo kinematic analysis of the human joints. (D'Amico et al., 1992) evaluates the recent methods applied in biomechanics for smoothing and derivative assessment.

2.5. APPLICATIONS, EXISTING SYSTEMS
Applications of motion analysis cover a wide range from missile tracking to locomotion analysis of cats. Only marker based applications will be mentioned in this section. The advantage of passive markers, that they cause almost no discomfort to human beings or animals, explains that the majority of their applications is related to human and animal motion. Attaching markers to landmark points, the gait and the arm motion are most frequently studied. Usually angles (e.g. at the knee, elbow, etc.) and displacements versus time are calculated. The studying of human gait disorders

helps in rehabilitation and assures a feedback for treatment. For a company, producing orthoses, movement analysis is important both in the development and for the fitting of orthoses to the patients. Three dimensional analysis of gait in paraplegic man - hip, knee and ankle angles, duration of the supporting and oscillatory stage of the gait - is useful to compare the postural and biomechanical parameters of the varying gait conditions. (Safee-Rad et al., 1990) reports of an arm motion study in feeding, providing fundamental information for the design of functional arm prosthesis. The involuntary facial movement analysis and mandibular motion analysis together with the results are given in (Furnée, 1989). The evaluation process of drugs for suppressing involuntary movements (choreoathetoid syndromes) can be backed by a Doppler radar motion transducer, too. It converts all body movements into one electrical signal, which contains information on the size and trajectory of the moving parts of the body (Kemp et al., 1982). A simple VME system based low-cost video system has been developed for recording human motion by tracking up to six markers (Keemink et al., 1991). A 3-D motion measurement system was applied during a space flight (Steinwender et al., 1992).

While testing human locomotion, quite frequently force plate signals and electromyographic (EMG) signals are also recorded. The analysis of kinematics of human gait based on the CINTEL system was detailed in (Winter et al., 1972b). The results of a statistical study on a group of normal subjects walking at different speeds is given in (Winter et al., 1974). (Costigan et al., 1992) reports on a semiautomatic 3-D knee motion assessment system. (Medved, 1991) describes a method to evaluate the skill level of athletes in fast locomotion using both kinetic and myoelectric signal analysis. Motion analyzers are widely used to test and aid other sport activities as well. (Sanderson et al., 1986) shows that the use of augmented feedback was effective for cyclists to improve their pedalling mechanics. (Zatsiorsky et al., 1990) investigated the aiming process in air-rifle shooting.

(Webb et al., 1982) gives a general method for recovering the three dimensional structure of moving rigid and jointed objects from several single camera views. Their method can be applied to any structure of jointed objects that conform to the fixed axis assumption. (Fioretti et al., 1990a) describes the CAMA (Computer Aided Movement Analysis) system and its specific application devoted to posture analysis.

Industrial applications include among others supervision of production lines or the trolley speed optimisation of a bulk crane.

Several motion analysis systems exist, a classification is given in Chapter 1. A detailed description of the systems would be beyond the scope of this dissertation. A short summary of the PRecIsion Motion Analysis System will be given, because it can be considered a good (and in many respects novel) representative of TV-based motion analyzers. Fig. 2.14. shows the block diagram of the PRIMAS system.

The *markers* are passive, non-wired retroreflectors, shaped as circular disks or low-mass spheres in a range of sizes. *Illumination* is stroboscopic, produced by an Infrared Emitting Diode (IRED) assembly. The IREDs are mounted around the camera lens and give light beams nearly parallel with it. There are different types of illuminators to match the field of view, determined by the lens, to obtain near uniform intensity of the marker images. The *cameras* are dedicated (HCS MXR/100) 100 Hz measurement quality CCD cameras. Their integration time is reduced (0.1 ms) and synchronised to the 0.1 ms IRED pulses. It means a 1:100 duty cycle resulting in a good ambient light suppression (1:100). The CCD sensor is the NXA 1011 from Philips with 288 effective lines (used in the non-interlaced mode) and 604 columns. The *video/digital coordinate converter* provides the x and y coordinates of image points (CCD pixels) corresponding to the video signal crossings of an adjustable threshold level. It produces the parameters of a marker segment. The *real-time marker segment processor* clusters the segments, belonging to the same marker image, and on the basis of all the segments estimates the centroid of the image. At present an IDT R3001 RISC processor board is applied (van Veenendaal, 1992). Geometric centroid calculation is standard, circle fitting is optional. The estimated centroid coordinates are transmitted to a PC through a fast (10 Mbyte/s) duplex serial line using coaxial cable (Furnée et al., 1993). The PC means the human interface, the camera configuration as well as the actual parameters of a measurement can easily be programmed through a menu system. The standard routines include camera calibration, action replay, display of time functions and stick diagrams, marker identification. The user programs can be written in high level languages (ASYST, MATHEMATICA).

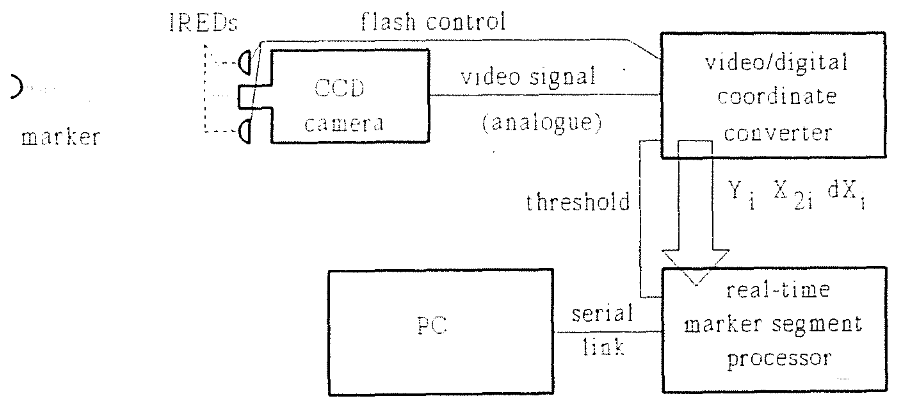

Figure 2.14. The functional block diagram of the PRIMAS system.

3. RESOLUTION AND ACCURACY OF THE MEASUREMENT

3.1. MARKER IMAGE AND BINARY MARKER IMAGE

Resolution and accuracy of marker centre estimation have been investigated by simulation. The simulation was carried out with the assumption that the *marker image* on the CCD surface is an ideal circle with uniform luminosity, see Fig. 2.11. This assumption is justified if the following simplifications are valid:

- ideal circular/spherical markers,
- homogeneous light reflection from the markers,
- totally compensated lens distortion,
- noise-free environment.

The mechanical distortion of the markers is negligible.
The homogeneous light reflection is a good approximation if the markers are circular disks. If the markers are (hemi)spherical then although their projection remains a circle the amount of the reflected light diminishes as the angle between the tangential plane of the sphere and the camera axis deviates from the right angle. It means a bell shaped intensity distribution instead of the puck shaped one in Fig. 2.11. The effect of intensity distribution will be discussed in section 3.2.
There are different, effective methods of lens distortion compensation and camera calibration, the most popular ones are the DLT method and the SMAC method. As the present investigation is concerned with local accuracy, limited to pixel and/or marker image size, the assumption of negligible lens distortion is even closer to reality.
The ambient light may cause charge patches to develop on the CCD pixels. This effect is very similar to that of the electrical noise of the components. Both distort the analogue video output signal that will be quantised in order to qualify pixels as 'covered' and 'uncovered'. As already mentioned, ambient light suppression may reach the 1:100 value. The signal/noise ratio of a measurement quality camera is good enough to keep the effect of noise at a negligible level. Electrical noise can be modelled as a varying threshold level of the comparator (one bit A/D converter), receiving the video output signal of the camera. The influences of the above simplifications can be summarised as the relative uncertainty of the simulated results. This relative uncertainty was found to be less than 2% if disks are used as markers and their plane is perpendicular to the axis of the camera.
In present day motion analyzers the video output signal of a CCD camera is processed by a 1 bit A/D converter. It means that a pixel is evaluated as *covered by the marker image* if the corresponding video output signal is above a given threshold level. As a result of this quantisation, marker images with different radii and centres can be placed on the CCD surface so that the resulting ***binary marker image*** is the same. The term binary marker image denotes a localised qualification: the adjoining pixels evaluated as covered (by the marker image) and their neighbours, evaluated as uncovered. Fig. 3.1. shows two marker images with different radii and centres. In those pixels, which are partly covered by the images the percentage of coverage is written: the upper number is always for the circle drawn by solid line while the lower one is for the circle drawn by dashed line. If the threshold level used for quantising the video signal corresponds to 50% coverage of a pixel - supposing uniform intensity distribution along the marker image - then after digitising the video output signal the same binary marker image belongs to both marker images. It means that when the binary marker image is known it determines neither the centre nor the radius of the

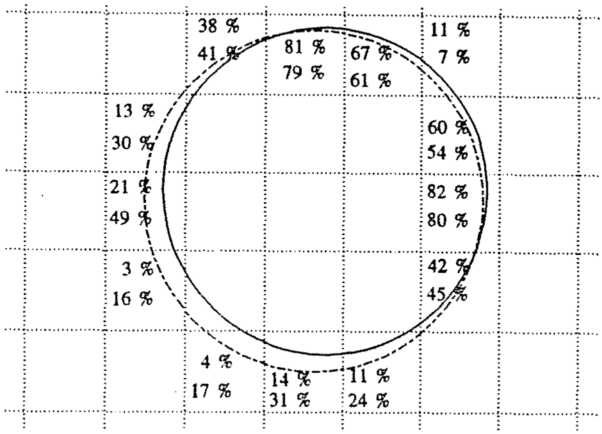

Figure 3.1. Marker images with different radii and centres may result in the same binary marker image as a result of quantisation.

covering marker image. In other words it is the result of the finite resolution and it is independent of the method used for estimating the centre on the basis of the covered pixels.

3.2. MODELS FOR THE SIMULATION

In order to create a satisfactory model for the analysis of resolution and accuracy we must have a closer look at how the marker image, projected on the surface of a CCD chip determines its video output signal and how this signal is digitised. Fig. 3.2. shows an ideal circular marker image projected onto a CCD surface. The centre coordinates are 3.75, 3.25 if integer numbers are related to the midpoint of a pixel. The video output signal of the chip is composed on the basis of the photon-induced charge pattern of the pixels. The charge developed on a pixel depends on the intensity of the light reaching it and the integration time. The light intensity - evenly for the whole surface of the CCD sensor - can be controlled by the diaphragm. It must be set to the proper value: to prevent pixels with 100 % lit surface from blooming but at the same time provide enough light for the pixels with only partly lit surfaces.

If 1 bit A/D conversion is used it means that the analogue video output signal of the CCD based camera is compared to a threshold voltage. According to the result of the comparison either **0** or **1** is related to each pixel: **1** if the corresponding video output signal exceeds the threshold level, **0** otherwise.

This relation can also be called *qualification*. Fig. 3.3. shows the result of a high (left) and a low (right) threshold level for the marker image of Fig. 3.2. A pixel is hatched if **1** is related to it. For the analysis of the resolution and accuracy with simulation a model is needed which relates either a **0** or a **1** to each pixel according to the actual marker image on the CCD chip. The actual image of a circular marker is fully specified by its centre and its radius and the relation is done on the basis of the ratio of the covered and the total area of a pixel.

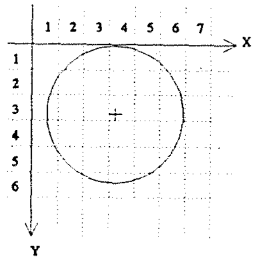

Figure 3.2. An ideal circular marker image on a CCD sensor surface.

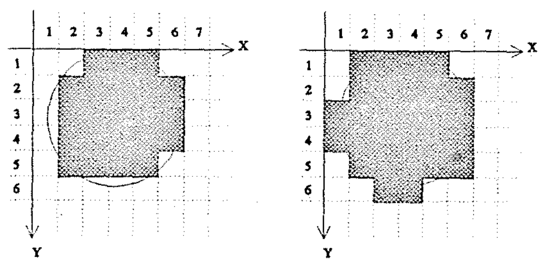

Figure 3.3. The effect of the threshold level on pixel qualification.

It follows that the model must deal with pixels *partly* covered by circular images. (If the whole surface of a pixel is covered then **1**, if no part of it is covered then **0** is related to it.) In the simulation **1** was related to a pixel if at least 50 % of its active surface was covered by a marker image. The active surface of a pixel is smaller than its physical size, cf. (van de Steeg et al., 1985).

We used three different models to answer the following question: *does a marker image cover at least 50 % of the active surface of a pixel* if the radius of the marker image is **R**, the horizontal and the vertical projections of the section between its centre **P** and the geometric centroid **M** of the pixel are **xd** and **yd** respectively and the pixel has a rectangular form with the horizontal side **s** and the vertical side **r * s**, see Fig. 3.4. There is a simple approximation based on the assumption that the active surface of a pixel is concentrated into its midpoint: if the distance between the centre of the marker image and the geometric centroid of the pixel is not greater than the radius of the marker image (**MP ≤ R** in Fig. 3.4.) then the whole active surface of the

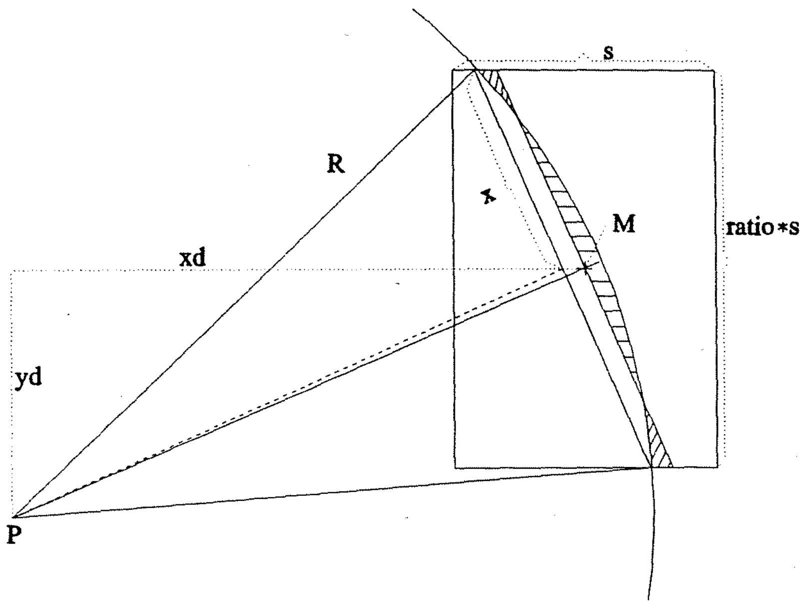

Figure 3.4. A pixel partly covered by a circular marker image.

pixel is covered. I developed a more accurate solution, too supposing that the active surface is symmetrically distributed along the total surface. Using the notations of Fig.3.4. at least 50 % of the active, and so of the total surface of a pixel is covered by a marker image if

$$\overline{MP} \le \frac{2}{3}*R + \frac{1}{3}*\sqrt{R^2 - x^2} \tag{3.1}$$

where

$$x \approx \begin{cases} \overline{MP}*\dfrac{\frac{s}{2}}{yd}, & \text{if ratio}*yd \ge xd \\ \overline{MP}*\dfrac{\frac{s}{2}}{xd}*\text{ratio}, & \text{if ratio}*yd < xd \end{cases} \tag{3.2}$$

Solving (3.1) and (3.2) for rectangular shaped pixels we get

where

$$\overline{MP} \leq R * \frac{12+\sqrt{36-3/l^2}}{18+0.5/l^2} \tag{3.3}$$

$$l \approx \begin{cases} \dfrac{yd}{s}, & \text{if ratio} * yd \geq xd \\[2ex] \dfrac{xd}{s * \text{ratio}}, & \text{if ratio} * yd < xd \end{cases} \tag{3.4}$$

The comparison of the two models (cf. Fig. 3.11. and Fig. 3.12.) shows that the application of the simple model means a virtual increase in the marker image radius. The actual value of the virtual increase is basically determined by the shape of the pixel but it also depends on the marker image size. The effect of this increase is the smaller the longer the actual radius is, compared to the pixel side. A third model was also tested, which originates from the frame transfer sensor, described in section 2.2. If the sensor is used in the non-interlaced mode, then 25% of the surface of each pixel is inhibited during the integration period and only 75% is active. The accurate model can easily be modified in order to consider only 75% of the pixel surface active. *From now on I will call the three different models "accurate", "75% active" and "simple" PCQ (pixel coverage qualifying) model.*
The effect of the bell shaped intensity distribution of a marker image can easily be taken into account if the simple PCQ model is used, cf. Fig. 3.5. The intensity is constant along a circumference and it decays as the distance increases from the centre of the circular image. Expressing the intensity (I) as a function of the ratio of this distance (d) and the marker image radius (r) we get:

$$I\left(\frac{d}{r}\right) = e^{-c_1\left(\frac{d}{r}\right)^{c_2}} \tag{3.5}$$

where c_1, c_2 are constants. Using the simple PCQ model, with the uniform intensity distribution assumption a pixel was qualified as covered if its midpoint was covered by the marker image. With the bell shaped intensity distribution assumption the condition for the coverage is augmented: the intensity in the midpoint of a pixel must be above a given threshold level. It means that the effect of the bell shaped intensity distribution is the virtual shortening of the marker image radius.
The accurate and the 75% active PCQ models require that the intensity distribution function be taken into account while summing up the charge of a pixel. If $\int_{A_p} I(A)dA$ exceeds the threshold level then the pixel is qualified as covered. A_p is the active area of a pixel and $I(A)$ is the intensity distribution along it. The PCQ models can be used for rectangular pixels with any ratio of the neighbouring sides.

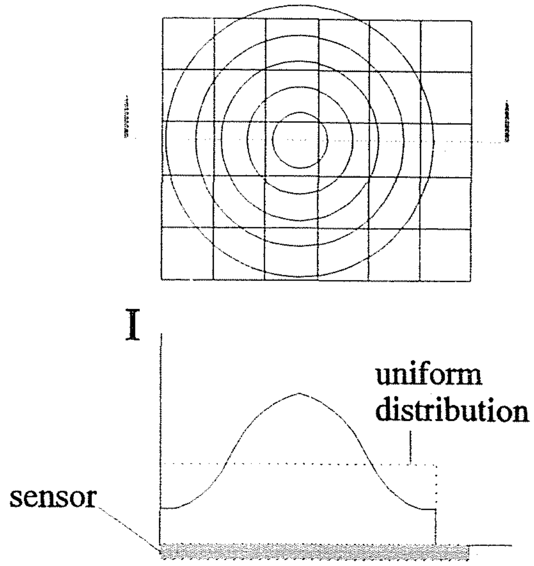

Figure 3.5. Bell shaped intensity distribution on the sensor surface.

3.3. RESOLUTION ANALYSIS

As a result of the *finite resolution* of a motion analyzer the position of a marker can change without a corresponding change in its estimated position. Areas can be defined in a way that if the centre of a circular marker image with a fixed radius is within an area then the estimated centre coordinates are the same independently of the actual position within the area. The actual forms of the above areas depend on the radius of the marker image. (The threshold level influences the actual forms, too.) The areas repeat as the centre of the marker image moves along the CCD surface as a result of its symmetrical structure. The pattern of areas must be the same for a whole pixel surface until no edge effect is present i.e. the distance between the pixel and the edge of the CCD chip is longer than the radius of the marker image.

The centre of a circle (representing an ideal circular marker image) with fixed radius was moved along a surface equivalent to the surface of a pixel. The expected values of the x and y sections of the above defined areas were computed. *Apart from the edge effect, the centre of a circle with a fixed radius was supposed to have uniform distribution along the CCD surface.* The analysis was repeated using different circle radii. The horizontal resolution analysis was done by scanning the designated surface horizontally at a number of different vertical positions. The lengths of the horizontal sections of the areas were determined and their expected value was calculated based on these data. Fig. 3.6. explains the proper surface selection for determining the horizontal resolution. Dotted lines form the border lines around an area ($A_{ci}^{(k)}$) to which the same binary marker image belongs and dashed lines separate the pixels. An area can be either within one pixel only or occupy parts of two or even four neighbouring pixels. Bold lines show the surface along which the analysis was carried out. The border lines of this surface do not intersect any of the horizontal sections - $\Delta x(A_{ci}^{(k)}, y)$ - of the areas, thus the scanning of the surface could easily be done. The pattern of areas is arbitrary, serves only for explanation and does not correspond to any marker image radius. The vertical resolution can be analyzed similarly.

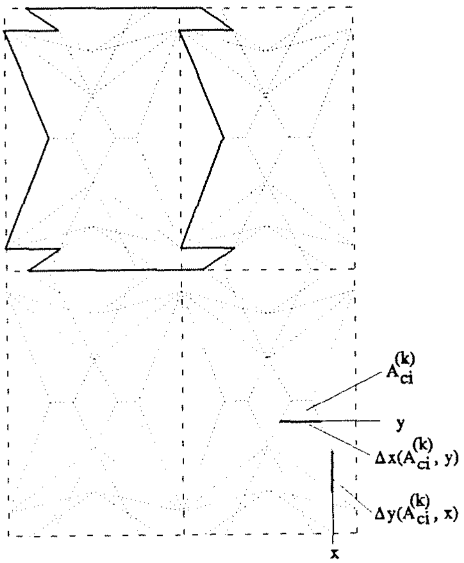

Figure 3.6. Designating the area for resolution analysis.

The following notation will be used while describing the resolution analysis:

r_{cmin}	=	the minimal marker image radius used during the analysis,
r_{cmax}	=	the maximal marker image radius used during the analysis,
Δr	=	the step size in the marker image radius during the analysis,
r_{ci}	=	$r_{cmin} + i * \Delta r$, the actual marker image radius,
N_{ci}	=	the number of different areas within the surface, equivalent to that of a pixel, if the radius of the covering image is r_{ci},
A_{ci}	=	$[A_{ci}^{(1)}, A_{ci}^{(2)}, \ldots, A_{ci}^{(N_{ci})}]$, the vector of the areas belonging to r_{ci},
$p(\epsilon)$	=	the probability of the event ϵ,
$E\{\xi\}$	=	the expected value of the random variable ξ,
$\Delta x(A, y)$	=	the horizontal section of the area A at the height of y,
$\Delta y(A, x)$	=	the vertical section of the area A at the width of x,

The horizontal and the vertical resolutions, belonging to r_{ci} are regarded as $res_x(r_{ci})$ and $res_y(r_{ci})$, respectively. They are defined as the expected values of the horizontal and the vertical sections of A_{ci}. In other words it means the expected length of the section along which the centre of a marker image with a given radius can be moved (either horizontally or vertically) without a change in the binary marker image:

$$res_x(r_{ci}) = \sum_{k=1}^{N_{ci}} p(A_{ci}^{(k)}) * E\{\Delta x(A_{ci}^{(k)})\}, \qquad \sum_{k=1}^{N_{ci}} p(A_{ci}^{(k)}) = 1 \tag{3.6}$$

where $p(A_{ci}^{(k)})$ is the probability that the centre of a circle with radius r_{ci} is within $A_{ci}^{(k)}$ if for the centre uniform distribution is supposed along A_{ci}.
The expected value of the horizontal section of an area is:

$$E\{\Delta x(A_{ci}^{(k)})\} = \int_{y_{min_k}}^{y_{max_k}} \Delta x(A_{ci}^{(k)}, y) f(\Delta x(A_{ci}^{(k)}, y)) dy \tag{3.7}$$

where $f(\Delta x(A_{ci}^{(k)}, y))$ is the probability density function of the horizontal sections of the area $A_{ci}^{(k)}$:

$$f(\Delta x(A_{ci}^{(k)}, y)) = \frac{\Delta x(A_{ci}^{(k)}, y)}{A_{ci}^{(k)}}$$

$$E\{\Delta x(A_{ci}^{(k)}, y)\} = \int_{y_{min_k}}^{y_{max_k}} \Delta x(A_{ci}^{(k)}, y) \frac{\Delta x(A_{ci}^{(k)}, y)}{A_{ci}^{(k)}} dy$$

$$E\{\Delta x(A_{ci}^{(k)}, y)\} = \frac{\int_{y_{min_k}}^{y_{max_k}} (\Delta x(A_{ci}^{(k)}, y))^2 dy}{A_{ci}^{(k)}} \tag{3.8}$$

The probability, $p(A_{ci}^{(k)})$, that the centre of a randomly projected marker image falls onto a given $A_{ci}^{(k)}$ area is proportional to the size of its area:

$$p(A_{ci}^{(k)}) = \frac{A_{ci}^{(k)}}{\sum_{j=1}^{N_{ci}} A_{ci}^{(j)}} \tag{3.9}$$

Thus the horizontal resolution can be calculated:

Similarly, the vertical resolution is:

$$res_y(r_{ci}) = \frac{\sum_{k=1}^{N_{ci}} \int_{x_{min_k}}^{x_{max_k}} (\Delta y(A_{ci}^{(k)}, x))^2 dx}{\sum_{j=1}^{N_{ci}} A_{ci}^{(j)}} \tag{3.11}$$

$$res_x(r_{ci}) = \sum_{k=1}^{N_{ci}} \frac{A_{ci}^{(k)}}{\sum_{j=1}^{N_{ci}} A_{ci}^{(j)}} \frac{\int_{y_{min_k}}^{y_{max_k}} (\Delta x(A_{ci}^{(k)}, y))^2 dy}{A_{ci}^{(k)}}$$

$$res_x(r_{ci}) = \frac{\sum_{k=1}^{N_{ci}} \int_{y_{min_k}}^{y_{max_k}} (\Delta x(A_{ci}^{(k)}, y))^2 dy}{\sum_{j=1}^{N_{ci}} A_{ci}^{(j)}} \tag{3.10}$$

During the simulation the area, equivalent to that of a pixel was scanned in finite number of steps, each step corresponding to a rectangular sub-area. The sections were determined as the number of consecutive sub-areas belonging to the same area. Within a surface, equivalent to that of an elementary pixel, if the radius of a marker image is r_{ci} then the total number of horizontal sections is nx, the total number of vertical ones is ny. The horizontal and vertical sections, belonging to r_{ci} are called $N_{sxi}^{(j)}$ and $N_{syi}^{(k)}$, respectively. The probability, that the centre of a randomly projected circular marker image falls onto a horizontal section is proportional to the area of that section, i.e. $N_{sxi}^{(j)}$ for the **j**th section. The vertical resolution can be determined similarly. Consequently, the horizontal and the vertical resolutions belonging to the radius r_{ci} were computed according to the formulae of Eq. 3.12.

$$res_x(r_{ci}) \approx \frac{\sum_{j=1}^{nx} (N_{sxi}^{(j)})^2}{\sum_{j=1}^{nx} N_{sxi}^{(j)}}, \quad res_y(r_{ci}) \approx \frac{\sum_{k=1}^{ny} (N_{syi}^{(k)})^2}{\sum_{k=1}^{ny} N_{syi}^{(k)}} \tag{3.12}$$

The expected values can be expressed as fractions of the corresponding side of a pixel to get relative results:

$$E'(Dx) = \frac{res_x}{s}, \quad E'(Dy) = \frac{res_y}{ratio * s} \tag{3.13}$$

With square shaped pixels **E'(Dx)≡E'(Dy)** as a result of the symmetry. If the shape of a pixel is rectangular where the length of the horizontal side is **s** and the length of the vertical side is **ratio ∗ s** then in order to get results comparable to the square shaped pixels the radius of the circular marker must be modified. The results for resolution and accuracy can be compared if the number of pixels, covered by the marker image, remains the same. Fig. 3.7. explains the derivation of the equivalent radius. It will be shown that the number of covered pixels is the decisive factor regarding both the resolution and the accuracy.

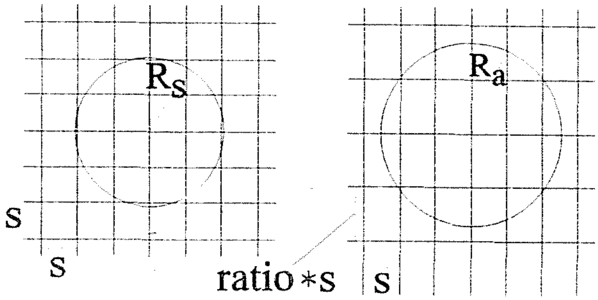

$$\frac{R_s^2 \pi}{s^2} = \frac{R_a^2 \pi}{ratio * s^2} \quad \Rightarrow \quad R_a = R_s\sqrt{ratio}$$

Figure 3.7. The equivalent radius for resolution analysis.

In the majority of cases a marker image covers 4...12 lines. In accordance with it the value of the marker radius was varied between 2 and 8 pixel sides, assuming symmetrical pixels, which means $2*\sqrt{ratio}$ to $8*\sqrt{ratio}$ in the case of asymmetrical pixels . As an example, if the ratio is 1.56 it is equivalent to approximately 3 to 13 covered lines (5 to 20 covered columns). To assure easy comparability the results are always given in equivalent radius. While selecting the step size, i.e. the distance of two adjacent centre positions of the fixed radius marker image while moving it along the part of the sensor surface, designated for analysis, a trade-off had to be done between the run time of the simulation and the accuracy of the results. Two different values for the step size in the centre position displacement (1% and 2% of the horizontal pixel side) were tested.

Fig. 3.8. shows the results with higher resolution, 100x100 steps within the square shaped and 100x156 steps within the rectangular shaped pixel (ratio = 1.56) with each radius. The pattern of areas proved to be very sensitive to the value of the marker image radius. It explains the extraordinary small step size during the analysis in the equivalent marker image radius: 0.01, resulting in 600 steps between 2.00 and 8.00.

In Fig. 3.9. the results of the same resolution analysis are presented, using simple PCQ model, 2% of the horizontal pixel side as step size in the centre position displacement and 0.02 as the step in the equivalent marker image radius.

Comparing Fig. 3.8. and Fig. 3.9. based on visual observation no substantial difference can be found. A more detailed analysis was carried out in order to find the above mentioned trade-off. To investigate the effect of the step size in the centre position displacement during simulation we compared the results acquired by using

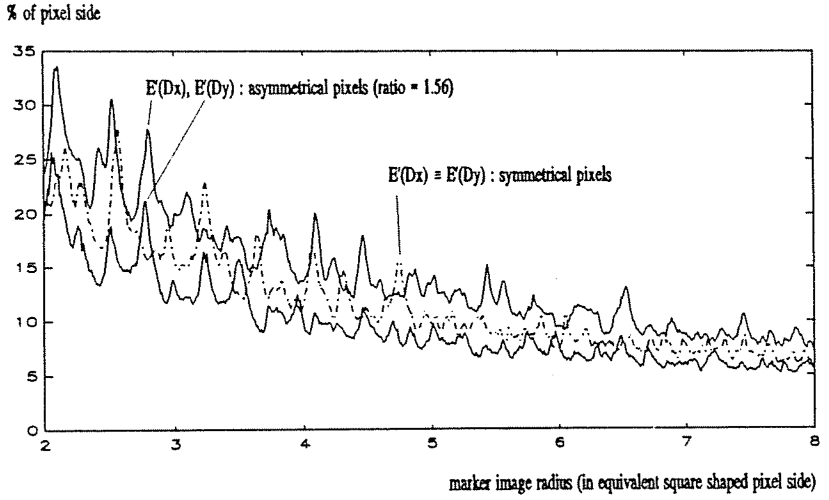

Figure 3.8. Resolution analysis, accurate PCQ model, step size in radius is 0.01, step size in the centre position displacement is 1% of its horizontal side.

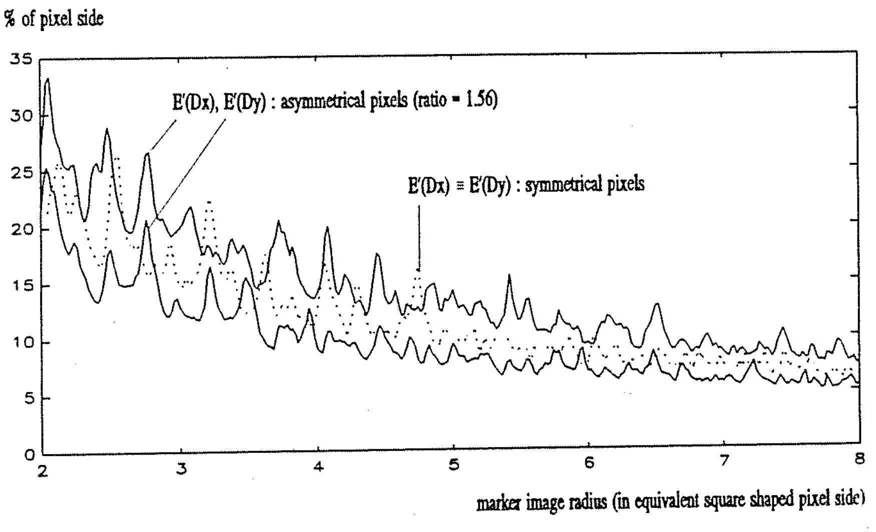

Figure 3.9. Resolution analysis, simple PCQ model, step size in radius is 0.02, step size in the centre position displacement is 2% of its horizontal side.

1% of the horizontal pixel side to those acquired by using 2% of the horizontal pixel side. In both cases the simple PCQ model was applied and the step in radius was 0.01. Fig. 3.10. shows the results. On the left the relative differences are given, the upper diagram is for the horizontal and the lower one is for the vertical resolution. On the right the histograms show the relative occurrences of the relative differences.

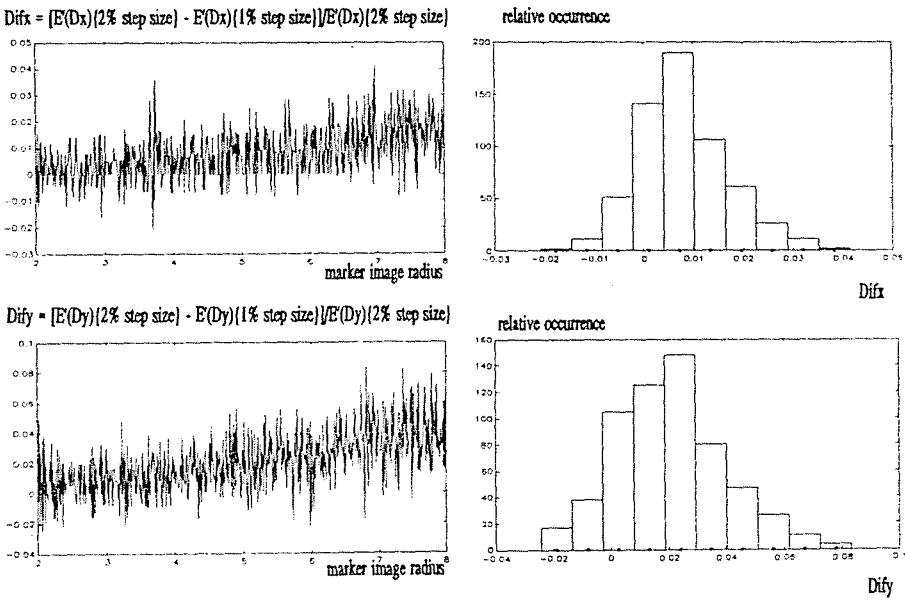

Figure 3.10. Comparing the results gained with different step sizes in the centre position displacement. Simple PCQ model, step in the radius is 0.01.

The relative deviation is smaller regarding the horizontal resolution (-2...+4%) but quite tolerable for the vertical resolution, too (-2...+8%). The average deviation is +1% for the horizontal and +2% for the vertical resolution. As a consequence, the 2% of the horizontal pixel side is sufficient as the step size in the centre position displacement.

In Fig. 3.11. the differences of the results are given, gained by using the accurate and the simple PCQ models. The step size in the centre position displacement is 2% of the horizontal pixel side (square shaped pixels) and the step size in the radius is 0.01. The relatively big differences can be decreased by discerning that the use of the simple PCQ model means a virtual increase in the marker image radius. We repeated

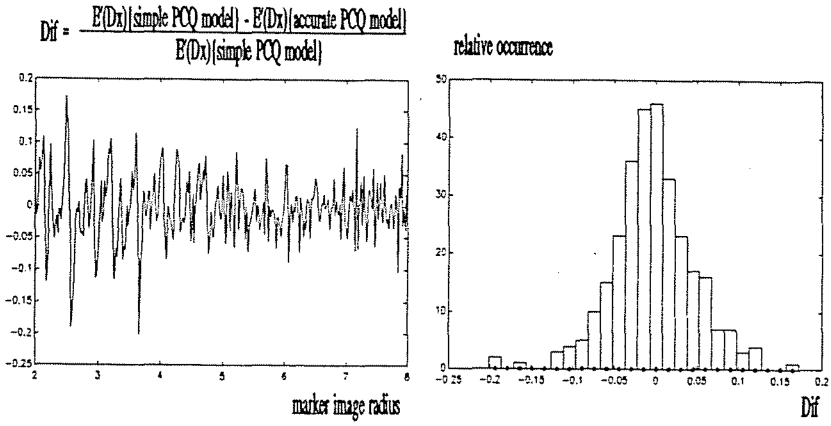

Figure 3.11. Comparing the accurate and the simple PCQ models. Step size in the centre position displacement is 2% of the horizontal pixel side, step size in the radius is 0.02. Square shaped pixels.

the investigation subtracting the results of the accurate PCQ model with greater radius from that of the simple PCQ model. The minimum for the difference was found with an 0.013 difference in radii, cf. Fig. 3.12.
We may conclude that the simple PCQ model is sufficient for the analysis. The step size in the radius during the analysis can be increased to 0.02, because neither the trend nor the local behaviour of the curves change with this "undersampling".
Hereafter, unless otherwise specified, simple PCQ model is used, the step size in the centre position displacement being 2% of the horizontal pixel side and the step size in radius being 0.02.
The careless evaluation of Fig. 3.8. may lead to the false conclusion that using asymmetrical pixels with longer vertical sides results in better vertical than horizontal resolution, however it is only true for the *relative resolutions*, expressed as fractions of the corresponding pixel sides. In practice the absolute values res_x and res_y are more informative, cf. Eq. 3.10. and 3.11. Fig. 3.13. shows that there is not a significant difference between the horizontal and the vertical resolutions if we compare the absolute lengths of the intersections, along which the centre of a marker image may move without a change in the binary marker image.
If we want to analyze the effect of the shape of an elementary pixel on resolution we must not forget about the different radii, belonging to the different shapes of pixels. It means that we have to express a section as a fraction of the marker image radius. It can be explained by a different reasoning, too. If the effect of the shape of the elementary pixel is investigated, then another correct comparison is to assume the *same area for the sensor element* and the same number of pixels within it. It means that the area of a pixel remains constant and consequently the horizontal side of a

pixel is the smaller the higher is the ratio of its vertical and its horizontal sides. In this case the term "equivalent radius" doesn't have to be used, the marker image radii must be the same. But the horizontal pixel side of a rectangular pixel (s_a) is smaller than that of the square shaped one (s_s):

$$s_a * s_a * \text{ratio} = s_s^2 \quad \Rightarrow \quad s_a = \frac{s_s}{\sqrt{\text{ratio}}} \tag{3.14}$$

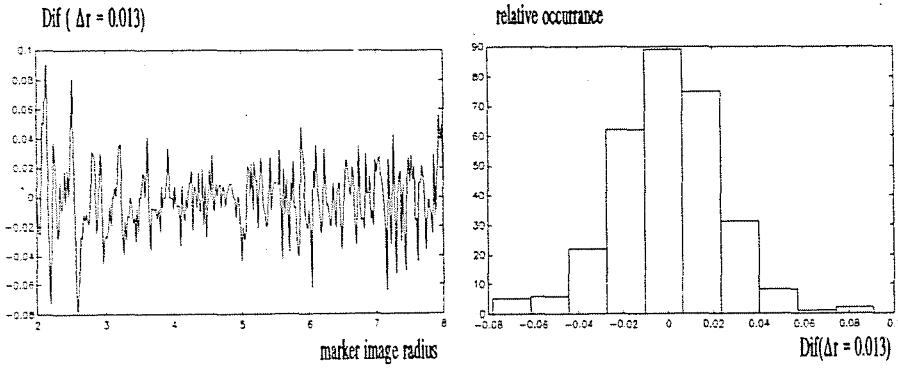

Figure 3.12. Comparing the accurate and the simple PCQ models. The virtual increase of the radius of the simple PCQ model is taken into account.

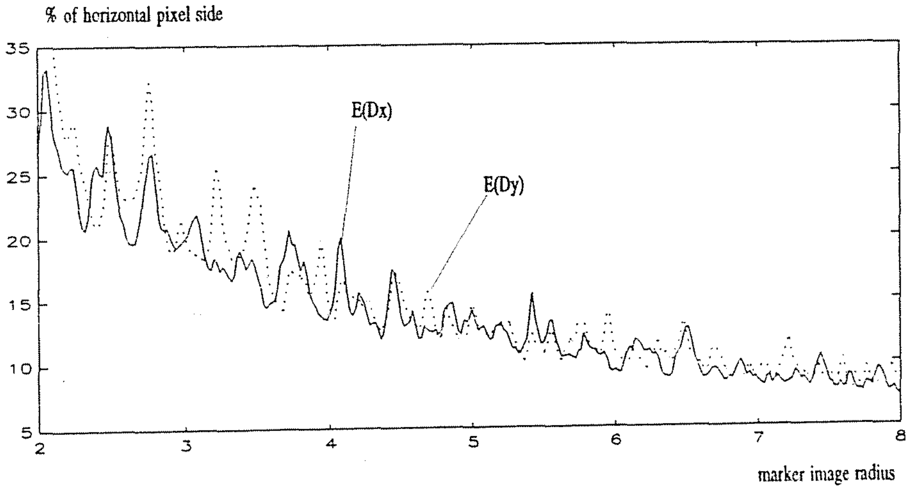

Figure 3.13. There is no significant difference between the horizontal and vertical resolutions, expressed as absolute distances.

Fig. 3.14. shows the horizontal resolution using asymmetrical pixels (ratio = 1.56) and the resolution using square shaped pixels taking the equivalent radius into account. Let's see why the pixel shape does not influence significantly the resolution. If we have two marker images with the same radius on the sensor surface and we move one image into the position of the other image on the shortest possible route, then the resolution can also be characterised by the number of different estimates, what we get for the marker image centre en route. Fig. 3.15. shows two images on a square shaped pixel grid.
The distance of their centres equals the side of a pixel. While we move one marker image into the position of the other image then if we use the simple PCQ model, then the number of different estimates, what we get for the marker image centre en route depends on the number of pixel midpoints that fall into the two crescent shaped areas. These areas are part of one image and are not part of the other, i.e. they are non-overlapping. Consequently, if we use the simple PCQ model, then the qualifica-

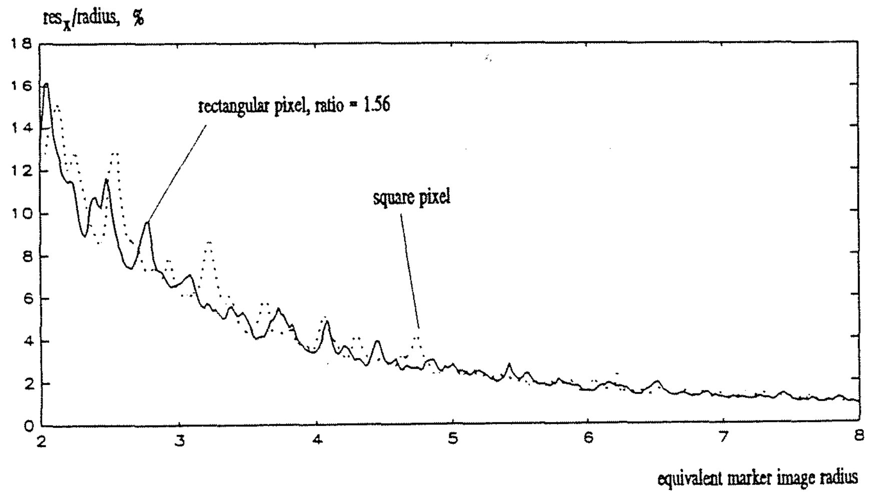

Figure 3.14. The shape of the pixel does not significantly influence the resolution.

tion of the pixels, the midpoints of which are in the crescent shaped areas, will change as we move the marker image between the two positions. Fig. 3.16. shows a grid, where the pixels are rectangular with a ratio of 4:1 of their sides but have the same area as the square shaped ones in Fig. 3.15.
Projecting the same marker images as in Fig. 3.15., the number of pixel midpoints in the crescent shaped area is also the same. It means that using the simple PCQ model for the pixel grid of Fig. 3.15. and Fig. 3.16. the same number of different estimates result as one image is moved, on the shortest possible route, in the position of the other. Different can be the distribution of the sections, along which the image centre

can be anywhere to result the same binary marker image. The *ratio of the pixel area and the crescent area* is the same, independently of the ratio of the pixel sides.

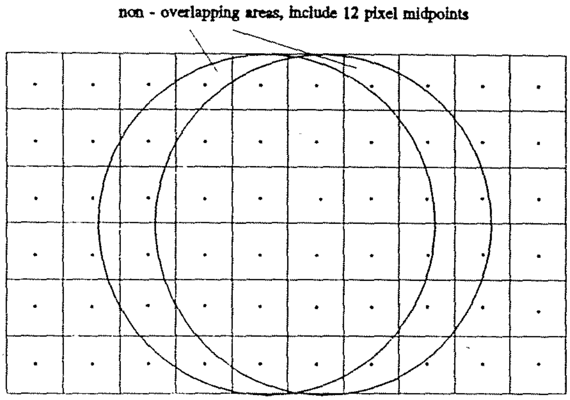

Figure 3.15. The pixel midpoints within the non-overlapping areas influence the resolution while an image is moved between the two positions on the shortest possible route.

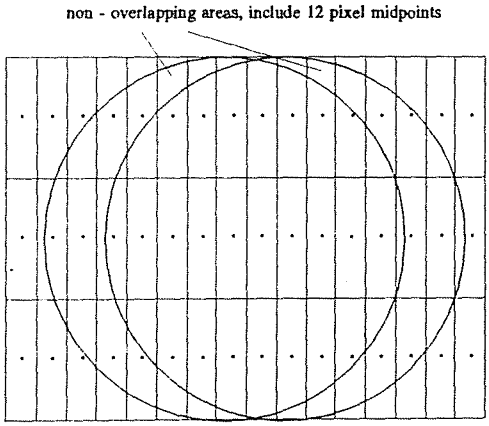

Figure 3.16. The ratio of the rectangular pixel sides does not significantly influence the number of pixel midpoints that are qualified differently while moving the image between the same positions.

The number of pixel midpoints within the non-overlapping area of the two images is not the only factor determining the resolution. The estimated centre of the image changes when the qualification of at least one pixel changes. As the image moves, the change of the qualification of those points, which have their midpoints in the non-overlapping area may happen at different distances from each other en route. It means that there may be different distributions of the same number of sections, where to each section the same marker centre estimate belongs. An unfavourable event is if the qualification of two (or more) pixel midpoints changes at the same time. The probability that it happens frequently depends on the ratio of the marker image radius and the pixel side. It explains that the resolution does not increase monotonously with increasing marker image radius. Using other PCQ models influences the distribution of the aforementioned sections while the ratio of the pixel area and the crescent area remains the same.

3.4. ACCURACY ANALYSIS

The markers are used as *carriers*, we are interested in the midpoint coordinates of the circular marker images, which should coincide with the landmark points of the moving objects. It follows that on the basis of the covered pixels of the binary marker images the midpoint of the covering circle should be determined. As a result of the quantisation, marker images with different radii and centres may result in the same binary marker image as shown in Fig. 3.1. The consequence is that we can give only an estimate for the centre of the marker image. Accuracy can be increased if some additional information is available, but we confine our investigation to the general case when neither the trajectory of a marker is known nor the possibility exists to take several measurements of the same marker positions. The accuracy of marker centre estimation depends on several factors. In this chapter only the influence of the estimation method will be dealt with, supposing that the other factors are ideal.

No a priori knowledge is utilised during the marker centre estimation, regarding the parameters of the possible covering image. A binary marker image could have been caused by marker images with different radii and centres. For the radius of a possible covering marker image uniform distribution is supposed. Having selected a radius, for the centre of a circle with that radius also uniform distribution is supposed along an area, so that while the centre is within that area the resulting binary marker image is the same. Accordingly, ***all possible covering marker images of a binary marker image are supposed to have the same probability.*** Justified by this assumption as well as by the ambition to give a general, application independent evaluation, I examined different statistical characteristics of the estimation methods. These characteristics give information about the estimation methods provided a marker image is projected randomly onto the sensor surface. This is a general information, taking into account all binary marker images that can be caused by marker images with a given radius. The following general statistical characteristics were used:

The *expected value of the deviation* of the estimated centre of a randomly projected marker image from its actual centre:

$$\mathrm{dev}(r_{cl}) = E\{d(P_a, P_e)\} \tag{3.15}$$

where P_a is the actual and P_e is the estimated centre, $d(P_a, P_e)$ is the distance between P_a and P_e. The deviation is given as a function of the radius of the randomly projected marker image, as $E\{d(P_a, P_e)\}$ depends on it in the case of all the estimation methods.
devx and devy will stand for the expected value of the horizontal and the vertical projection of this distance, respectively.
The *expected value of the squared deviation* of the estimated centre of a randomly projected marker image from its actual centre, characterising the variance of the estimation, is:

$$\mathrm{sqdev}(r_{cl}) = E\{d^2(P_a, P_e)\} \tag{3.16}$$

The *maximal value of the deviation* of the estimated centre of a randomly projected marker image from its actual value:

$$\mathrm{maxdev}(r_{cl}) = \max\{d(P_a, P_e)\} \tag{3.17}$$

maxdevx and maxdevy will stand for the maximal horizontal and vertical distance, respectively.
In the case of *one* binary marker image the deviations between the estimated centre point and the possible marker image centre points are not given as a function of the marker image radius. The expected values of the squared distances are defined as

$$CF_{sd}(\text{binary marker image}) = E\{d^2(P_i, P_e)\} \tag{3.18}$$

where P_i represents all the possible covering marker image centres, regardless of the radius. If all P_i points have the same probability then

$$CF_{sd}(\text{binary marker image}) = \frac{\int_{r_1}^{r_2} E\{d^2(r)\}A(r)dr}{\int_{r_1}^{r_2} A(r)dr} \tag{3.19}$$

where r_1 is the smallest, r_2 is the longest possible radius of the covering image, $E\{d^2(r)\}$ is the expected value of the deviation between the actual and the estimated centres if the supposed value of the radius is r, A(r) is the area, along which the centre of a covering image with radius r can be anywhere to produce the binary marker image.
Similarly, for the expected values of the distances:

$$CF_d(\text{binary marker image}) = E(d(P_I, P_e)) \tag{3.20}$$

$$CF_d(\text{binary marker image}) = \frac{\int_{r_1}^{r_2} E(d(r))A(r)dr}{\int_{r_1}^{r_2} A(r)dr} \tag{3.21}$$

As a result of the symmetry of the sensor, it is enough to move the centre of a fixed radius marker image along only one pixel area to get the statistical characteristics (neglecting the edge-effect, when an image is only partly on the sensor surface). Fig. 3.17. shows the results when the *geometric centroid calculation* was the tested estimation method. Simple PCQ model was used, the step size in the centre position displacement was 2% of the horizontal pixel side and the step in the radius was 0.02.

The ratio of the neighbouring sides of the rectangular pixel was 1.56. The effect of these simplifications were tested the same way as in the case of the resolution analysis and these parameters were found to be satisfactory. ***Unless otherwise noted, all the further figures were derived with these parameters.*** Contrary to the resolution analysis, the *relative* values are quite similar as shown in Fig. 3.18. and Fig. 3.19. Comparing the square shaped and the asymmetrical pixel grid neither devx nor devy show the differences in the relative values we experienced during resolution analysis. It could be expected, that the square shaped pixels provide better results for the distances between the real and the estimated centres. Fig. 3.20. demonstrates that this is not the case.

I compared the accuracy of the geometric centroid calculation and the circle fitting method. The pixel for the analysis was asymmetrical, the ratio of the neighbouring sides being 1.56. As it can be seen from Fig. 3.21. there is no significant difference between estimating with the geometric centroid and circle
fitting. The reason is that neither of the two methods takes into account that the quantisation errors, that occur along the circumference, are not independent of each other.

In order to give the proper evaluation of the conventional estimation methods I determined the **theoretical limit of accuracy**, that can be achieved by centre estimation based on binary marker images.

The theoretical limit of accuracy is defined with the assumption that the radius of the covering marker image is known. In the general case, when the covering marker image radius is unknown, to a binary marker image only one estimate belongs. As already described, if a circular marker image with known, fixed radius is moved along the sensor surface, then, as a result of quantisation, areas can be defined so that if the centre is anywhere within an area, the binary marker image is the same. It was also shown, that a binary marker image can be caused by marker images with

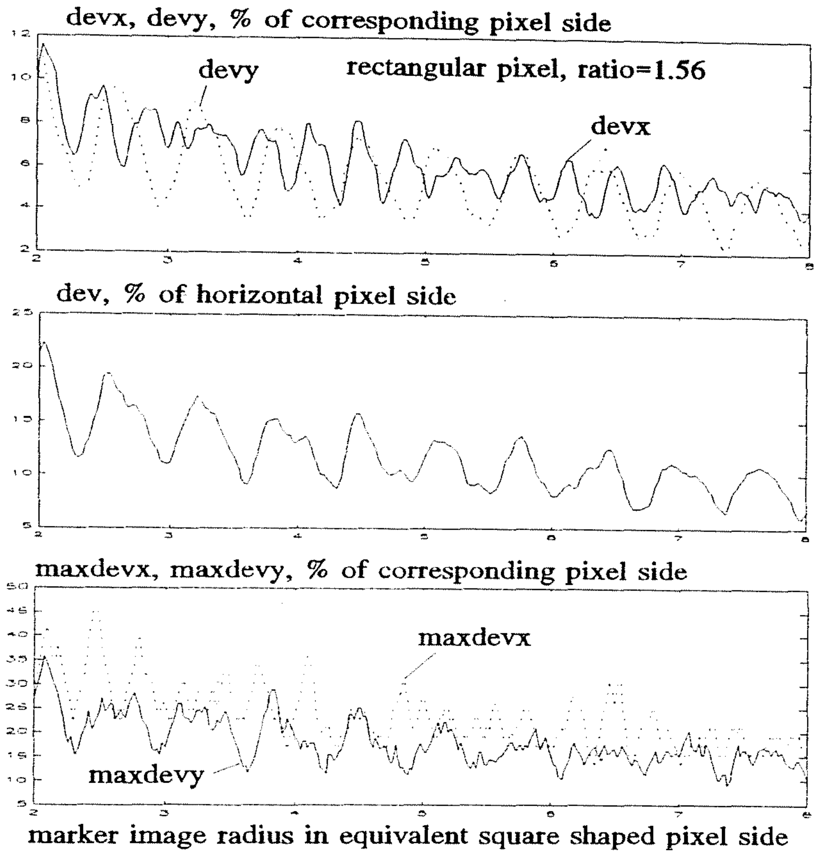

Figure 3.17. Characterisation of the accuracy of the geometric centroid calculation

different radii. It follows, that to one binary marker image different areas may belong as a function of the radius of the covering marker image. This means that considering the marker image radius known, to one binary marker image different estimates may belong as a function of the radius. The theoretical limit of accuracy is derived by relating an estimate to a binary marker image based on the area, determined by the binary marker image and the supposed radius of the covering marker image. This estimate can be optimal if the cost function is given. The cost function can be the expected value of either the deviation or the squared deviation between the actual and the estimated centres. In the following it will be determined for both cost functions how the estimated centre of a binary marker image should be designated within the corresponding area if the radius of the covering image is known.
For the analysis, the area - corresponding to a binary marker image and the given radius - will be considered as composed of N subareas, where N is big enough to

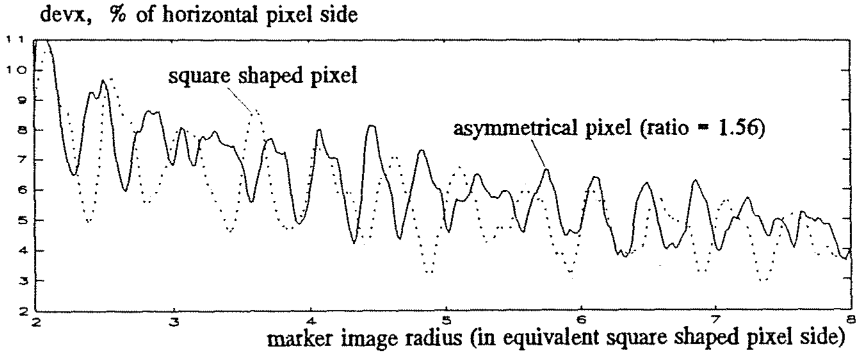

Figure 3.18. Characterisation of the horizontal accuracy of geometric centroid calculation.

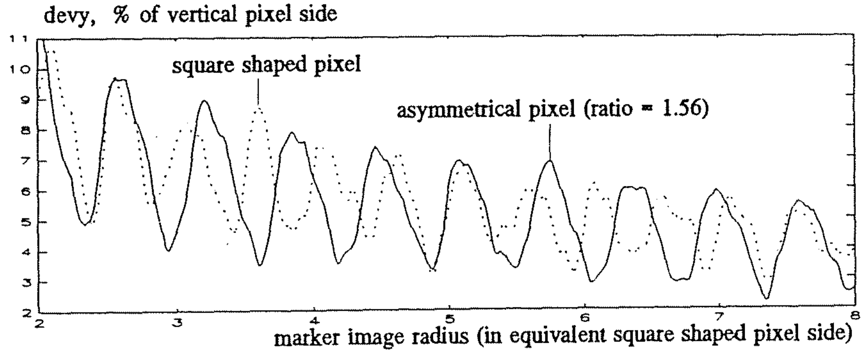

Figure 3.19. Characterisation of the vertical accuracy of geometric centroid calculation.

allow for the approximation that a subarea is a point, P_a. The coordinates of the P_a points are: x_a, y_a , $a = 1 \dots N$, P_e (X_e, Y_e) is the estimated centre.
Cost function: $E\{d^2(P_a, P_e)\}$

$$E\{d^2(P_a, P_e)\} = \frac{1}{N}\sum_{a=1}^{N}((x_a - X_e)^2 + (y_a - Y_e)^2) \qquad (3.22)$$

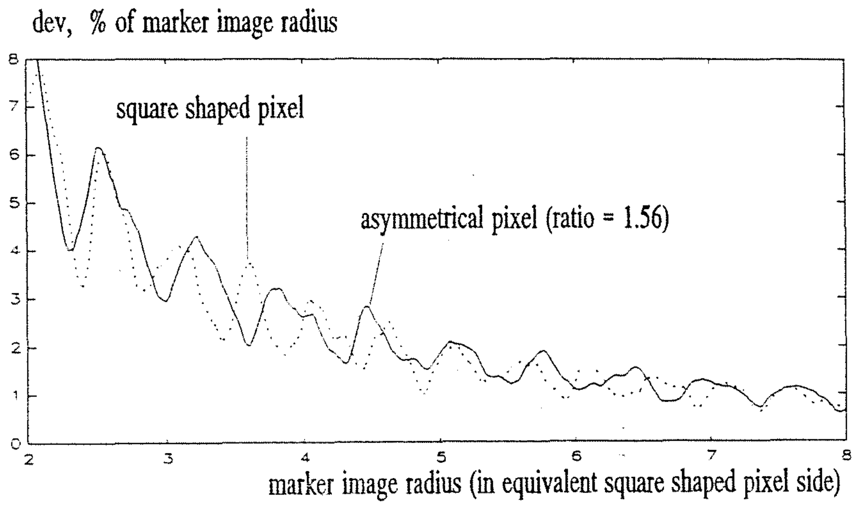

Figure 3.20.dev(r_{ci}) for the geometric centroid calculation: the pixel shape does not significantly influence it.

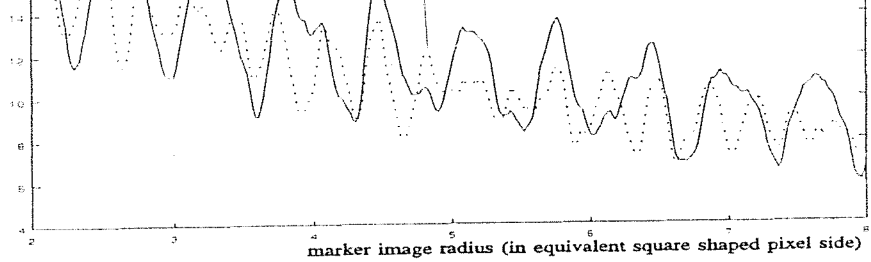

Figure 3.21.There is no significant difference between geometric centroid estimation and circle fitting regarding dev(r_{ci}).

The value of the cost function is minimal, if

$$\frac{\partial(E\{d^2(P_a, P_e)\})}{\partial X_e} = 0, \quad \text{and} \quad \frac{\partial(E\{d^2(P_a, P_e)\})}{\partial Y_e} = 0 \qquad (3.23)$$

$$\frac{\partial(E\{d^2(P_a,P_e)\})}{\partial X_e} = -\frac{2}{N}\sum_{a=1}^{N}(x_a - X_e) = 0, \quad \text{if} \quad X_e = X_{se} = \frac{1}{N}\sum_{a=1}^{N} x_a \qquad (3.24)$$

Similarly,

$$Y_e = Y_{se} = \frac{1}{N}\sum_{a=1}^{N} y_a \qquad (3.25)$$

It means that the geometric centroid of an area - P_{se} (X_{se}, Y_{se}) - should be selected as the estimated centre of the corresponding binary marker image.
Cost function: $E\{d(P_a, P_e)\}$

$$E\{d(P_a, P_e)\} = \frac{1}{N}\sum_{a=1}^{N}\sqrt{(x_a - X_e)^2 + (y_a - Y_e)^2} \qquad (3.26)$$

The cost function is minimal, if X_e is selected so, that:

$$\frac{\partial(E\{d(P_a, P_e)\})}{\partial X_e} = \frac{1}{N}\sum_{a=1}^{N}\frac{1}{2}\frac{-2(x_a - X_e)}{\sqrt{(x_a - X_e)^2 + (y_a - Y_e)^2}} = 0 \qquad (3.27)$$

Y_e should be selected similarly. The optimal estimated centre point is P_{de}, as for its coordinates X_{de}, Y_{de}:

$$\sum_{a=1}^{N}\frac{x_a - X_{de}}{d(P_a, P_{de})} = 0, \quad \sum_{a=1}^{N}\frac{y_a - Y_{de}}{d(P_a, P_{de})} = 0 \qquad (3.28)$$

The (3.28) equations cannot be solved for X_{de} and Y_{de} analytically. Furthermore, the application of numerical solutions can be difficult if P_{de} is close to a P_a point. However, it is possible to find a point P'_{de} within an area so that the sums of the horizontal and the vertical projections of the distances between all P_a and P'_{de} be minimal. The sums are:
These sums are minimal if X'_{de} is the median of the x_a points and Y'_{de} is the median of the y_a points. This assures that the expected values of the horizontal and the vertical projections of the $d(P_a, P'_{de})$ distances are minimal. It does not necessarily

$$sum_x = \sum_{a=1}^{N} x_a - X'_{de}, \quad sum_y = \sum_{a=1}^{N} y_a - Y'_{de} \tag{3.29}$$

mean that the $E\{d(P_a, P'_{de})\}$ expected value is minimal.
According to the actual needs of an application, further cost functions can be used.

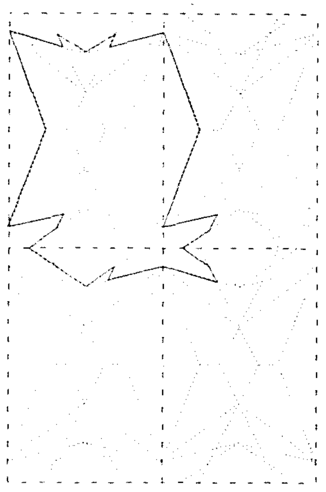

Figure 3.22. The selection of the surface to be scanned shows how it can be made up of whole areas.

While computing the theoretical limit of accuracy with simulation it is a must that the surface, along which the centre of the marker image is moved, be made up of ***whole areas***, because the optimal estimate is determined on the basis of an area. It is demonstrated in Fig. 3.22., which uses the same arbitrary pattern of areas as Fig. 3.6. The results - using sqdev as cost function - are given in Fig. 3.23., compared to the results gained by the geometric centroid estimation method. Rectangular shaped pixels are assumed. Supposing asymmetrical pixels, Fig. 3.24. shows devx and devy as a function of the equivalent marker image radius both for the geometric centroid calculation and for the theoretical limit.
During the simulation the results gained with different cost functions were found to be very close to those results gained by using $E\{d^2(P_a, P_e)\}$ as cost function.
Not only the much smaller expected values for the difference between the real and the estimated marker image centres characterise the theoretical limit, but also the substantially smaller local variations, as a function of the image radius. However, the local variations are present, even while computing the theoretical limit of accuracy, so this phenomenon must be taken into account while using any estimation method.

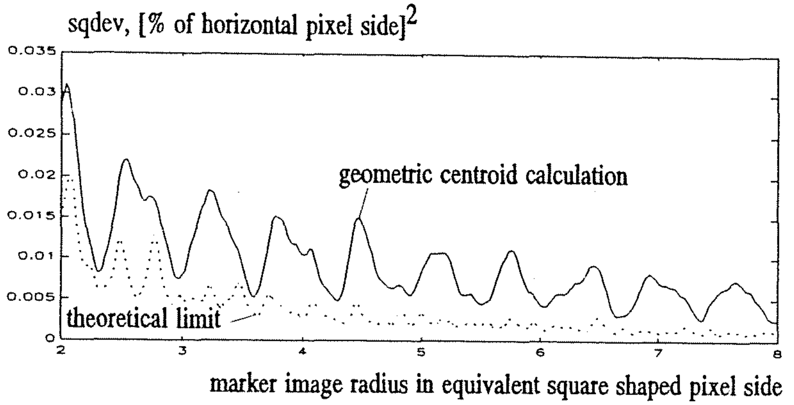

Figure 3.23. Comparing the accuracy of geometric centroid estimation method to the theoretical limit of accuracy.

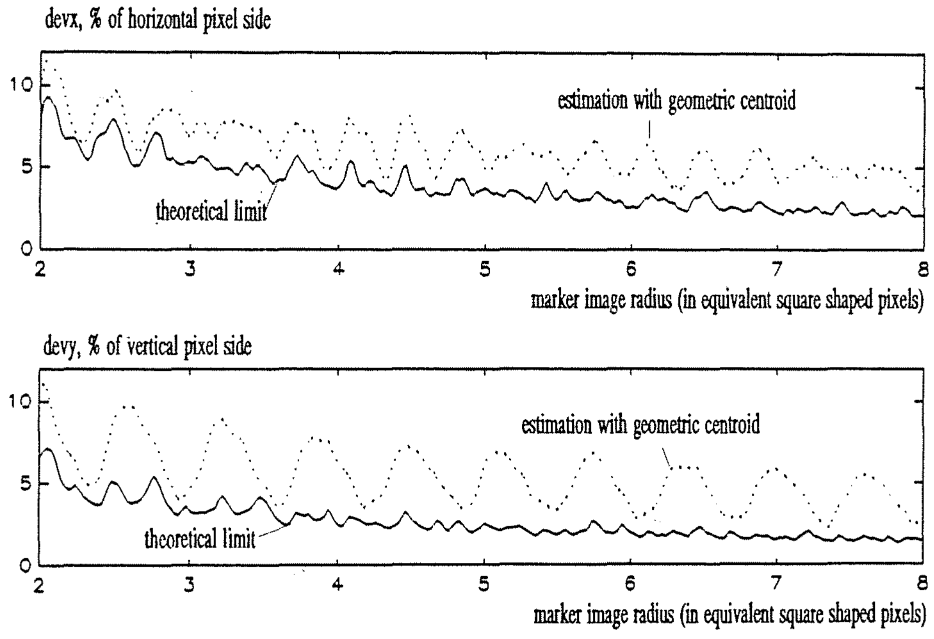

Figure 3.24. Comparing the horizontal and vertical accuracies of geometric centroid estimation to the theoretical limits. Asymmetrical pixel is assumed, the ratio of its neighbouring sides is 1.56.

The geometric centroid calculation may even result in an estimated midpoint, from which the 'covered set' of a binary marker image cannot be covered with a circle! Fig. 3.25. and Table 3.1. illustrate this, using the simple PCQ model. The dots represent pixel midpoints, both the actual centre of the covering circular image (3.90, 3.975) and its geometric centroid estimate (3.793, 3.966) are marked. Table 3.1. contains the distances of some points along the circumference from the actual centre as well as from the estimated one. As the geometric centroid estimate is closer to the (1, 5) point, which is 'not covered', than to the (4, 7) point, which is 'covered', it is clear that the original 'covered set' cannot be covered from this point independent of the radius.

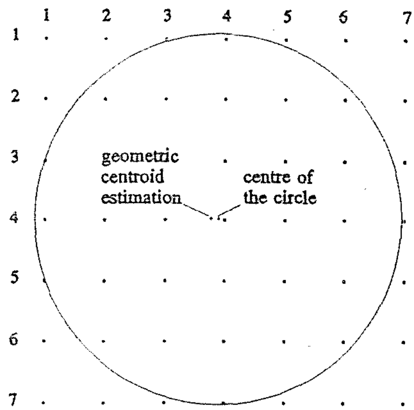

Figure 3.25. Illustration of the distortion of the geometric centroid estimation.

P_i	distance from the centre of the covering image	distance from the geom. centroid estimate	qualification of the point
(3, 1)	3.108	3.070	not covered
(4, 1)	2.977	2.973	covered
(1, 3)	3.060	2.955	covered
(7, 4)	3.100	3.207	not covered
(1, 5)	3.076	2.978	not covered
(4, 7)	3.027	3.041	covered

Table 3.1.

Distances of pixel midpoints from the actual and the estimated (by geometric centroid calculation) midpoints of the circular image is shown in Fig. 3.25.

3.5. THESES FROM THE CHAPTER

Thesis 1.

I showed that the resolution of marker centre estimation is basically determined by the number of pixels, covered by the marker image, but the relation - contrary to that of implied by the diagrams, published in the literature - is not monotonous. Regarding the tendency, the more pixels are covered the better is the resolution, but for small changes the relation might be opposite.

I showed, that the resolution - expressed as a distance - depends only negligibly on the ratio of the vertical and horizontal sides of a pixel. There is no significant difference between the horizontal and the vertical resolutions in the case of rectangular pixels: plotting the resolution versus the marker image radius, the regions characterised by better horizontal resolution are separated by regions where the vertical resolution is better.

Thesis 2.

2.1. I defined the theoretical limit of accuracy for centre estimation of binary marker images, regarding CF_{sd} as cost function. This can be reached if the radius of the marker image is known. To each binary marker image the geometric centroid of the area is related, along which the centre of the fixed radius marker image can be anywhere to result in the same binary marker image.

2.2. I showed that the conventional methods (geometric centroid calculation, circle fitting) of marker centre estimation are not optimal regarding the accuracy. The reason is, that they neglect the fact, that the quantisation errors along the circumference are not independent of each other.

I showed that both the geometric centroid calculation and the circle fitting can give an estimate for the centre, from which the binary marker image cannot be caused by a circle: the circle either does not cover pixels, that should be covered or covers pixels, that must not be covered.

4. NEW METHODS FOR CENTRE ESTIMATION

Based on the results of Chapter 3, the conventional marker centre estimation methods cannot be considered optimal, in the sense that their input data would allow for a more accurate estimate. Neither the geometric centroid calculation nor the circle fitting algorithm take into account that the quantisation errors along the circumference of the marker image are not independent of each other. The circle fitting method might be advantageous if the marker image is partly occluded. This will be dealt with in more details in section 4.4. If the marker images are not distorted then the circle fitting algorithm does not give more accurate results than the geometric centroid calculation, so coming from its simplicity the latter is usually applied.
The evaluation of the results, gained by the conventional estimation methods shows that there is a possibility to develop an estimator with better accuracy.

4.1. THE BEST ESTIMATE WITHOUT RADIUS INFORMATION (BEWRI)

In Chapter 3 cost functions were introduced to evaluate the estimates given for the centre of a binary marker image. While determining the theoretical limit it was shown how to select the optimal estimate to a binary marker image when the radius of the covering image is supposed to be known and the cost function is defined. The estimate was determined based on the area, along which the centre of the fixed radius marker image could be anywhere to cause the binary marker image.
In practical cases the marker image radius is not known. The input data of centre estimation is only the binary marker image. The coverage can result from marker images with different radii and centres, and to each fixed radius covering image different areas may belong. The exact definition of the centre estimation problem is: ***given a binary marker image and a cost function, what is the best estimate for the centre point of the covering marker image***. Among the different possible cost functions CF_{sd} (cf. Eq. 3.19) will be used in the following. However, the method can be applied with other cost functions as well.
Examining different binary marker images we concluded that

a.) a given set of pixels can be covered by circular images with different radii,

b.) applying the method, described at the theoretical limit of accuracy, different estimated centres may be assigned to the same binary marker image assuming different radii.

The lack of any a priori information justifies the assumption that all possible covering marker images occur with the same probability. The devised BEWRI method takes into account all the possible covering marker image centres and minimises CF_{sd}.
Fig. 4.1. shows a part of a CCD chip surface and the circular image of a marker projected onto it. Those elementary pixels are hatched that are qualified as covered after digitisation by a 1 bit A/D converter. The ratio of the two sides of an elementary pixel is 1.56. Fig.4.2. shows a smaller part in the middle of the same sensor surface and on it pyramids illustrate the estimates for the centre of the binary marker image shown in Fig.4.1.
The estimates were derived with the method, described at the derivation of the theoretical limit, supposing different, but in each case regarded as fixed marker radii. The base of a pyramid shows the x,y coordinates of the centre of gravity of the area, along which the centre of a circular marker image may move with the given radius so that the covered pixels are those, hatched in Fig. 4.1. The height of a pyramid is

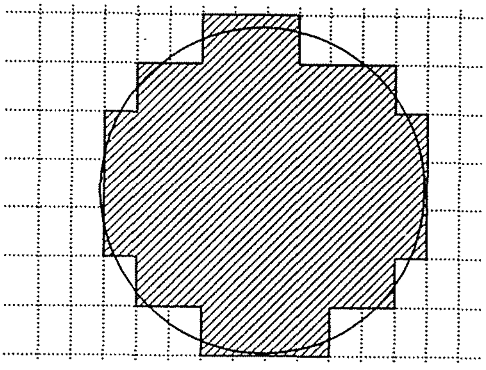

Figure 4.1. A circular marker image on the surface of a CCD chip. The hatched elementary pixels can be qualified as covered, depending on the threshold level.

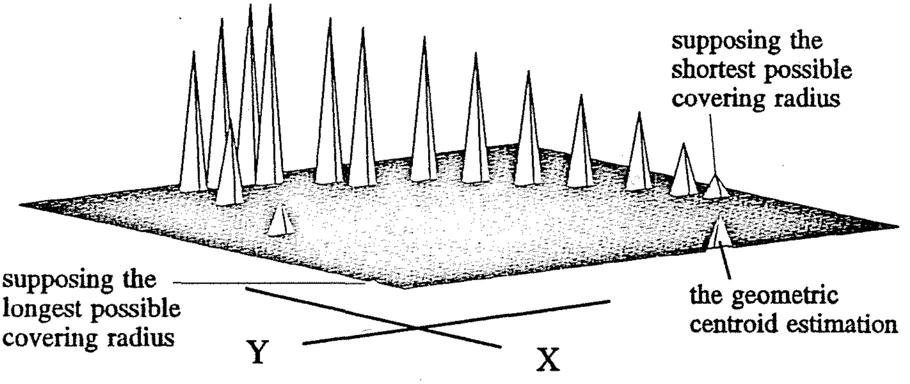

Figure 4.2. Estimations of the centre of a marker image, that can cover the hatched pixels of Fig. 4.1.

proportional to the size of the corresponding area. The result of the geometric centroid calculation is also shown on the figure, and it can be seen that it gives a distorted estimate for this binary marker image. The shortest covering marker image radius yields an estimate in the upper right part, while the longest one in the bottom of Fig. 4.2.

The BEWRI (Best Estimate Without Radius Information) method relates an estimate to a binary marker image so that the expected value of the squared difference between the estimated and the real centres of a marker image, which is randomly projected onto the sensor surface is minimal. CF_{sd} must be minimised, assuming uniform distribution for the possible covering marker image radius and if a radius is given, then also assuming uniform distribution for the centre of the covering marker image along the possible area. All the possible covering marker images are taken into account:

$$\text{BEWRI(binary marker image)} = \frac{\int_{r_1}^{r_2} CG[A(r)]A(r)dr}{\int_{r_1}^{r_2} A(r)dr} \tag{4.1}$$

where r_1 is the shortest, r_2 is the longest possible radius of the covering image, $A(r)$ is the area, along which the centre of a covering image with radius r can be anywhere to produce the binary marker image and $CG[A(r)]$ is the centre of gravity of $A(r)$.
If the radius is increased from r_1 to r_2 in M discrete steps:

$$\text{BEWRI(binary marker image)} = \frac{\sum_{i=1}^{M} CG[A(r_d(i))]A(r_d(i))}{\sum_{i=1}^{M} A(r_d(i))} \tag{4.2}$$

where $r_d(i) = r_1 + (i - 1)/(M - 1) * (r_2 - r_1)$, $i = 1 \dots M$.
The following proof shows the optimality of the discrete form of BEWRI (cf. Eq.4.2), the integral formula can be proved accordingly.
Let's consider the area - $A(r_d(i))$ - , belonging to $r_d(i)$ as composed of N_i subareas, where N_i is big enough to allow for the approximation, that a subarea is a point P_{ij} (X_{ij}, Y_{ij}), $j = 1 \dots N_i$. N_i depends on the size of the corresponding $A(r_d(i))$ area. If the size of the subarea is A_s, then

$$N_i = \text{int}\,\frac{A(r_d(i))}{A_s} \tag{4.3}$$

In this case the total number of different centre points for the possible covering marker images is N_{cm}:

$$N_{cm} = \sum_{i=1}^{M} N_i \approx \frac{1}{A_s}\sum_{i=1}^{M} A(r_d(i)) \tag{4.4}$$

The cost function to be minimised is (cf. Eq. 3.18):

$$E(d^2(P_{ij}, P_e)) = \frac{1}{N_{cm}} \sum_{i=1}^{M} \sum_{j=1}^{N_i} ((X_{ij} - X_e)^2 + (Y_{ij} - Y_e)^2) \tag{4.5}$$

To get a minimum, the partial derivatives must be equal to zero:

$$\frac{\partial(E(d^2(P_{ij}, P_e)))}{\partial X_e} = 0, \quad \frac{\partial(E(d^2(P_{ij}, P_e)))}{\partial Y_e} = 0 \tag{4.6}$$

These derivatives are equal to zero, if

$$X_e = \frac{1}{N_{cm}} \sum_{i=1}^{M} \sum_{j=1}^{N_i} X_{ij}, \quad Y_e = \frac{1}{N_{cm}} \sum_{i=1}^{M} \sum_{j=1}^{N_i} Y_{ij} \tag{4.7}$$

X_e is the average of the X coordinates of all X_{ij} points,
Y_e is the average of the Y coordinates of all Y_{ij} points.
Let's calculate X_e and Y_e in two steps. First the average of the X and Y coordinates of the P_{ij} points, belonging to the same i (i.e. to the same supposed radius) are calculated:

$$X_{ei} = \frac{1}{N_i} \sum_{j=1}^{N_i} X_{ij}, \quad Y_{ei} = \frac{1}{N_i} \sum_{j=1}^{N_i} Y_{ij} \tag{4.8}$$

As the second step, the X_{ei}, Y_{ei} averages are averaged:

$$X_e = \frac{\sum_{i=1}^{M} X_{ei} N_i}{\sum_{i=1}^{M} N_i} \approx \frac{\sum_{i=1}^{M} CG_x[A(r_d(i))] \frac{A(r_d(i))}{A_s}}{\frac{1}{A_s} \sum_{i=1}^{M} A(r_d(i))} \tag{4.9}$$

where $CG_x[A(r_d(i))]$ is the x coordinate of the centre of gravity of $A(r_d(i))$. Similarly Y_e can be determined, and so the statement in Eq. 4.2. is proved.
Figure 4.3. demonstrates the effectiveness of BEWRI. In this figure the accuracy of the geometric centroid calculation and of the BEWRI method are compared to the theoretical limit of accuracy. The pixels are asymmetrical, the ratio of the neighbouring sides is 1.56. It is evident that the BEWRI method is a good approximation of the theoretical limit of accuracy (Jobbágy et al., 1993b).

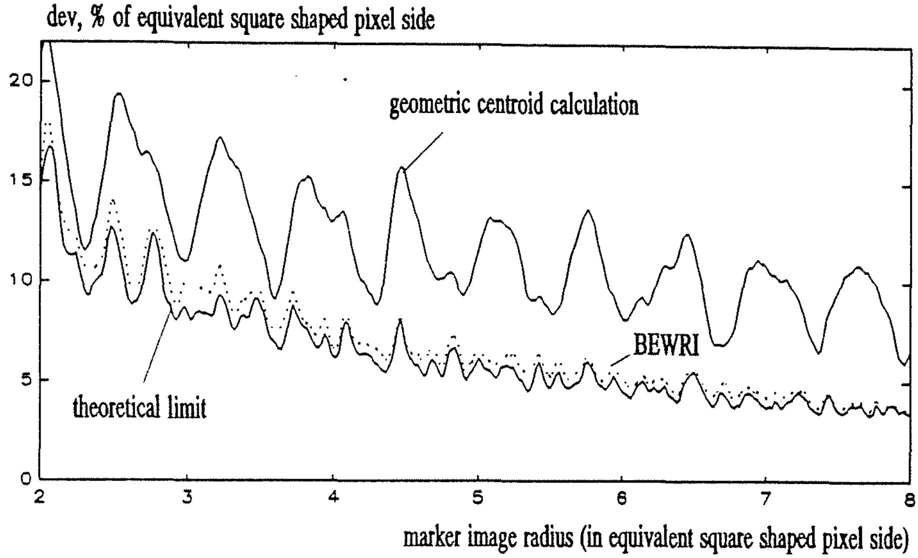

Figure 4.3. The BEWRI method is a goodapproximation of the theoretical limit of accuracy.

4.2. THE RING FITTING METHOD

The BEWRI method was derived in the previous section by searching an estimated centre point for a binary marker image, which results in a minimum for the CF_{ed} cost function. All possible covering images were supposed to have the same probability. The results gained by the BEWRI method are close to the theoretical limit of accuracy. However, the method requires a great number of computations. Let's change the cost function in the following: the best estimate is the P_e (X_e, Y_e) point, that can be the centre of a covering marker image with the highest probability. The assumption regarding the distributions both for the marker image radius and for the marker image centre is still valid, so P_e is a point which can be the centre point of covering marker images with different radii.

The ***ring fitting method*** searches for the widest ring that can be placed around the covered pixels of a binary marker image so that only these pixels are inside the ring. The centre of this ring is regarded as the estimate for the centre of the binary marker image. Fig. 4.4. shows a binary marker image and a possible ring fitted to it. P_e is the centre of the ring, r_1 is the radius of the inner circle and r_2 is the radius of the outer circle. The width of the ring is $\Delta r_r = r_2 - r_1$. A point is considered to be the estimated centre of the binary marker image, if the difference between the longest and the shortest radii of possible covering circles, drawn around this point, is maximal. This

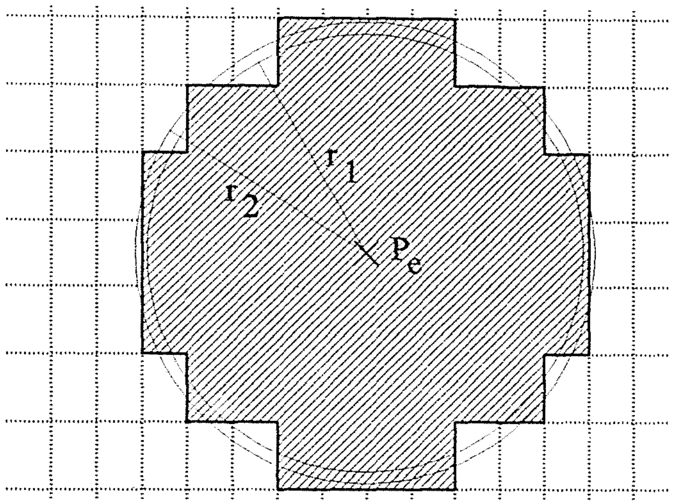

Figure 4.4. A ring with centre point P_e fitted to a binary marker image.

point is among the possible centres of covering images in the case of a binary marker image, derived from an ideal circular marker image. Fig. 4.2. shows the estimated centres and illustrates the sizes of the corresponding areas for the binary marker image shown in Fig.4.1. if we calculate estimates assuming fixed values for the covering image radius, from the shortest up to the longest possible value. The ring fitting method can be explained by supposing a scan along the whole area, where the centre of a covering marker image might be. In each point the range of the possible covering radii is calculated and the point to which the widest range belongs is selected. It means, that

$$\Delta r_r(P_i) = r_{P_{max}} - r_{P_{min}} \tag{4.10}$$

is calculated for each possible P_i point along the area on the x,y plane where the centre of a covering image might be, and

$$P_e \ , \quad e = i : \{\Delta r_r(P_i) \rightarrow \max\} \tag{4.11}$$

is considered to be the estimated centre point.
Fig.4.5. illustrates all the possible circular covering marker images that can result in the binary marker image of Fig.4.1. A circular marker image can be specified by two data: its centre point and its radius. In Fig.4.5. the radius is plotted along the vertical axis. The two surfaces relate the maximal (top surface) and the minimal (bottom surface) possible covering radii to each point on the x,y plane. The shown area of the

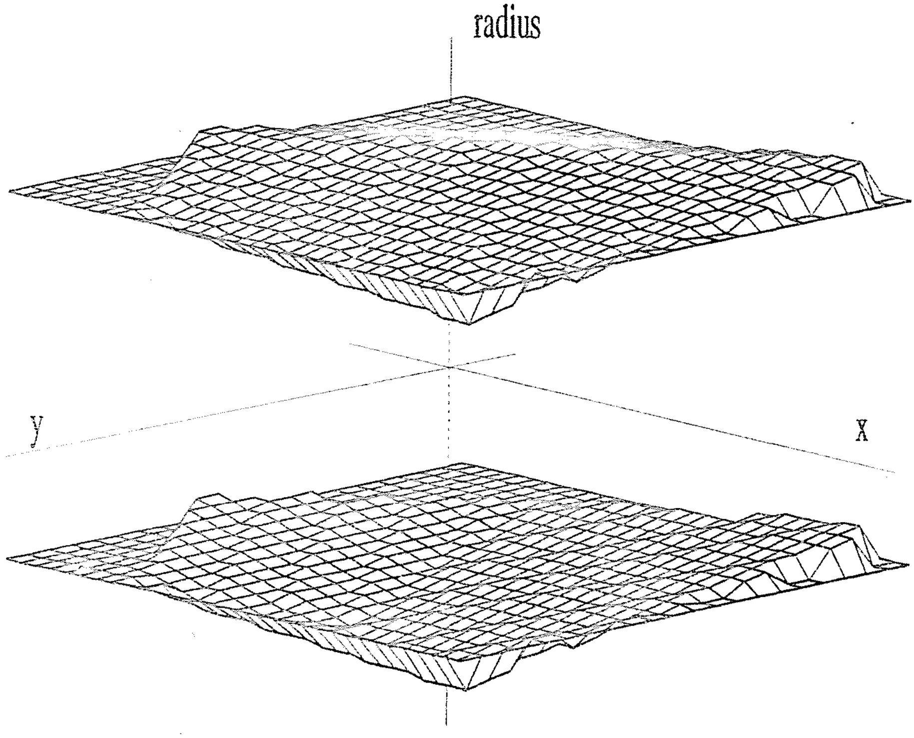

Figure 4.5. Illustration of the possible covering marker images of Fig.4.1. The horizontal plane stands for the x,y coordinates of the centres while the vertical axis is for the radii.

x,y plane - the same as in Fig. 4.2. - contains all the possible centres of the circular covering images, the area corresponds to a fraction of the light sensitive cover of the CCD sensor. The two surfaces are taken apart from each other along the r axis for the sake of better illustration, they should be fitted together along their flat parts. In the x,y,r Descartes coordinate system the two surfaces define a volume so that each triple inside the volume specifies a possible circular covering image: x,y are the coordinate values of its centre and r is its radius.
Fig.4.6. shows the same x,y plane for the centres of possible circular covering marker images as Fig.4.5. To each point on the plane the difference of the maximal and minimal radii, the ring width $\Delta r_r(P_i)$, belonging to that point is related and plotted along the vertical axis. It means that the difference of the two surfaces, given in Fig.4.5. are shown in Fig.4.6. Along the x,y plane of the possible marker image centres both the distribution of the ring width (top) and its contour map (bottom) is plotted.

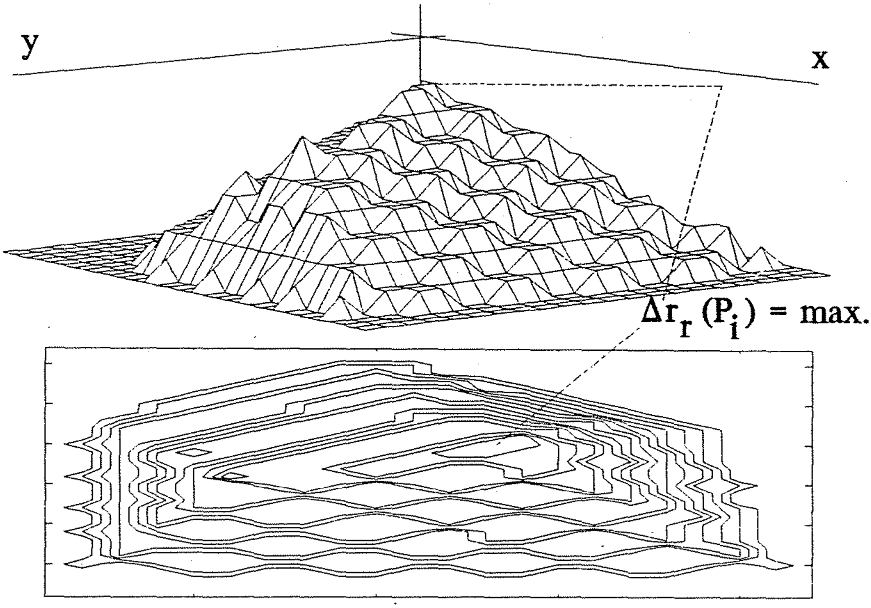

Figure 4.6. Distribution and contour map of the ring width that can cover the *covered pixels* of the binary marker image shown in Fig. 4.1.

The ring fitting method can easily be generalised so that it could be applied to distorted binary marker images, which cannot be covered by ideal circular images. Given the binary marker image let the positions of the covered pixel midpoints be P_k(cov) and the positions of the not covered pixel midpoints, being neighbouring points to the covered points be P_j(ncov). The ring width Δr_r belonging to a point P_i is the distance between P_i and the farthest covered pixel midpoint subtracted from the distance between P_i and the closest not covered pixel midpoint:

$$\Delta r_r(P_i) = \min(d(P_i, P_j(\text{ncov}))) - \max(d(P_i, P_k(\text{cov}))) \tag{4.12}$$

P_j(ncov) and P_k(cov) are the input data, characterising the binary marker image. Fig. 4.7. explains the definition of $d(P_i, P_j(\text{ncov}))$ and $d(P_i, P_k(\text{cov}))$. The ring fitting method means the search for the widest possible ring, $\max(\Delta r_r(P_i))$, moving P_i. Although the ring width is always positive in the ideal case, notice that the definition in Eq.4.12. allows for *negative* values as well! It will be made use of while dealing with distorted marker images.

The ring fitting algorithm was evaluated with simulation. During the simulation I used the geometric centroid of the covered pixels in the binary marker image as a starting point for P_i and searched for the maximal Δr_r with iteration. The simple PCQ method was applied, the step size in the centre position displacement was 2% of the

corresponding pixel side and the step in the equivalent radius was 0.02. Asymmetrical pixels with ratio = 1.56 were assumed. The results are given in Fig. 4.8.
The figure clearly shows that regarding the dev values BEWRI is definitely more favourable than ring fitting, but both are substantially better than geometric centroid calculation. Fig. 4.9. shows devx and devy for the three methods, separately.

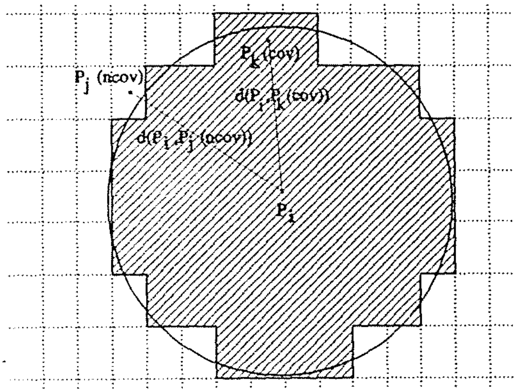

Figure 4.7. Distances of a P_i point from covered and not covered pixel midpoints.

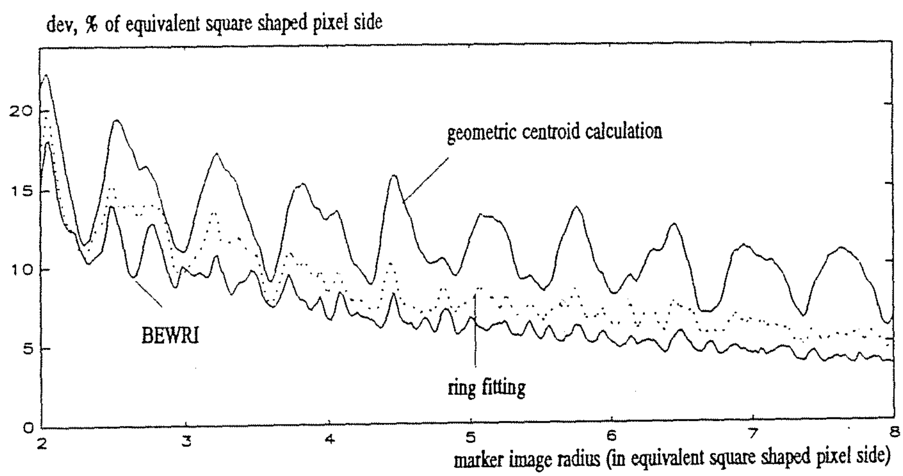

Figure 4.8. Comparing the ring fitting method to BEWRI. Asymmetrical pixels were assumed, with a ratio of 1.56.

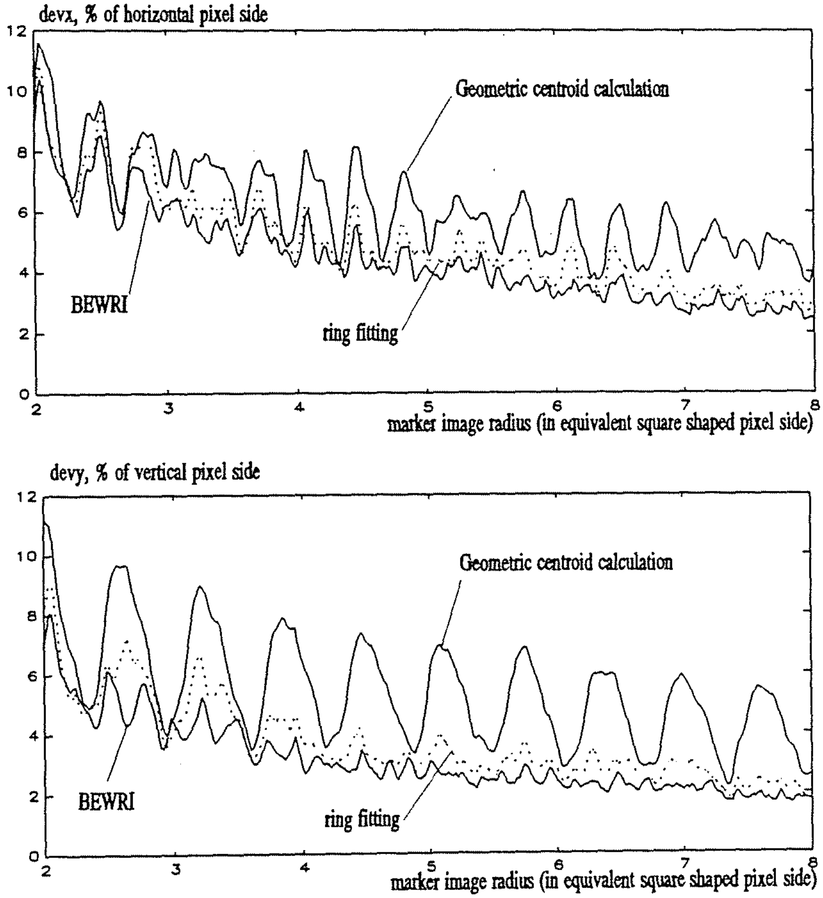

Figure 4.9. The horizontal (top) and the vertical (bottom) accuracies of the geometric centroid calculation, the BEWRI and the ring fitting methods.

4.3. REALISATIONS OF THE METHODS

Realisation of the BEWRI method

Realising the method according to the definition requires a great number of computations and as a result can only be applied off-line. Two algorithms have been developed which approximate the accuracy of the BEWRI procedure and reduce the number of the necessary operations (Jobbágy et al., 1993a). The MAXARE (MAXimal ARea Estimate) algorithm searches for the maximal area, belonging to a possible covering marker image radius, and considers the centre of gravity of this area as the estimate for the centre of the binary marker image.

$$\text{MAXARE(binary marker image)} = \text{CG}[A(r_m)],\quad A(r_m) = \max_{r_1 \le r \le r_2} \{A(r)\} \qquad (4.13)$$

To get the AVRAE (AVerage RAdius Estimate) result for a binary marker image first the minimal and the maximal possible radius of the covering marker image and their average must be determined.

$$\text{AVRAE(binary marker image)} = \text{CG}[A(r_a)],\quad r_a = \frac{r_1 + r_2}{2} \qquad (4.14)$$

In Eq. 4.13. and Eq. 4.14. r_1 stands for the shortest and r_2 for the longest possible covering radius.

While evaluating the BEWRI method and its realisations by simulation the centres of all the possible different binary marker images were estimated. This was done in the following steps (the notations used are the same as defined in section 3.3., cf. page 48):

S1.) The marker image radius was scanned from 2 to 8 equivalent square shaped pixel sides in 0.02 steps: $r_{ci} = r_{cmin} + i*\Delta r$, $i = 0 \ldots N_r$, $r_{cmin} = 2$, $\Delta r = 0.02$ and $N_r = 300$.

S2.) The elements of the A_{c0} vector were determined belonging to $i = 0$: $A_{c0} = [A_{c0}^{(1)}, A_{c0}^{(2)}, \ldots, A_{c0}^{(Nc0)}]$,

S3.) The elements of the A_{c1} vector were determined belonging to $i = 1$ and rearranged to get an A'_{c1} vector in the following way: if there exists an $A_{c1}^{(k)}$, $1 \le k \le N_{c1}$, so that the corresponding binary marker image is the same as it is in the case of $A_{c0}^{(1)}$ then $A'_{c1}{}^{(1)} = A'_{c1}{}^{(k)}$, if there is no such $A_{c1}^{(k)}$ then $A'_{c1}{}^{(1)} = 0$. This rearrangement was repeated until the 1 ... N_{c0} elements of A'_{c1} were determined. If not all the elements of A_{c1} have been used then the remaining elements were put as the consecutive elements of A'_{c1} : $A'_{c1}{}^{(Nc0+1)}$, ...

S4.) The previous step was repeated, i.e. the A_{ci} vectors were rearranged according to the $A'_{c(i-1)}$ vectors to get A'_{ci} until $i = N_r$.

S5.) Zero padding was completed: the A'_{ci} vectors were augmented, $i = 0 \ldots N_r - 1$ with zero elements to achieve row vectors of the same length as A'_{cNr} .

S6.) A matrix was formed by writing the A'_{ci} , $i = 0 \ldots N_r$ row vectors one below the other. The matrix has $N_r + 1$ rows and the number of its columns is equal to the number of different binary marker images while the radius of the covering image is varied between r_{cmin} and r_{cmax} in Δr steps. The form of the matrix is the following:

$$
\begin{array}{llllllllll}
A_{c0}^{(1)} & A_{c0}^{(2)} & & A_{c0}^{(3)} & \ldots & A_{c0}^{(Nc1)} & 0 & \ldots & 0 & \ldots 0 \\
A'_{c1}{}^{(1)} & 0 & A'_{c1}{}^{(3)} & \ldots & A'_{c1}{}^{(Nc1)} & A'_{c1}{}^{(Nc1+1)} \ldots & 0 & \ldots & 0 & \\
 & & & \vdots & & & & & & \\
0 & 0 & 0 & \ldots & 0 & 0 \ldots & A'_{cNr-1}{}^{(NcNr)} & \ldots & 0 & \\
0 & 0 & 0 & \ldots & 0 & 0 \ldots & A'_{cNr}{}^{(NcNr)} \ldots & A'_{cNr}{}^{(NcNr+\ldots)} & &
\end{array}
$$

Table 4.1.

Each column of the matrix belongs to one binary marker image. A zero in the row of r_{ci} indicates that the corresponding binary marker image cannot be covered by an image with that radius. The BEWRI estimation yields the weighted average of the centres of gravity of the areas being present in the column of the binary marker image, the weighting factors being the areas themselves.

$$\text{BEWRI(k. binary marker image)} = \frac{\sum_{l=0}^{N_r} CG(A_{cl}^{'(k)}) A_{cl}^{'(k)}}{\sum_{l=0}^{N_r} A_{cl}^{'(k)}} \tag{4.15}$$

The MAXARE approximation is computed by searching for the maximal area in each column:

$$\text{MAXARE(k. binary marker image)} = CG[\max_{0 \le l \le N_r} \{A_{cl}^{'(k)}\}] \tag{4.16}$$

The calculation of the AVRAE (AVerage RAdius Estimate) result requires the minimal and the maximal values of the radii of the possible covering marker images and then their average value.

$$
\begin{aligned}
a &= \min j \; \{A_{cj}^{'(k)} \neq 0\} \\
b &= \max j \; \{A_{cj}^{'(k)} \neq 0\}
\end{aligned} \tag{4.17}
$$

The centre of gravity of the area, that corresponds to the average radius is considered as the estimated centre of the covering marker image:

$$\text{AVRAE(k. bin. marker image)} = CG(A_{cn}^{'(k)}), \quad n = (a + b)/2 \qquad (4.18)$$

If $a + b$ is an odd number then interpolation can be done based on $A_{cn}^{'(k)}$ and $A_{c(n+1)}^{'(k)}$, where $n = \mathrm{int}[(a+b)/2]$.

For the binary marker image of Fig. 4.1. the BEWRI estimate has been computed together with its MAXARE and AVRAE approximations. Fig. 4.10. shows the x,y plane of Fig. 4.2. Estimates gained by assuming different, fixed radii are shown, together with the results of the above three methods. The step size in the marker image radius was 0.01, increasing it from the shortest to the longest possible value: 3.94 ... 4.09 in equivalent square shaped pixel side.

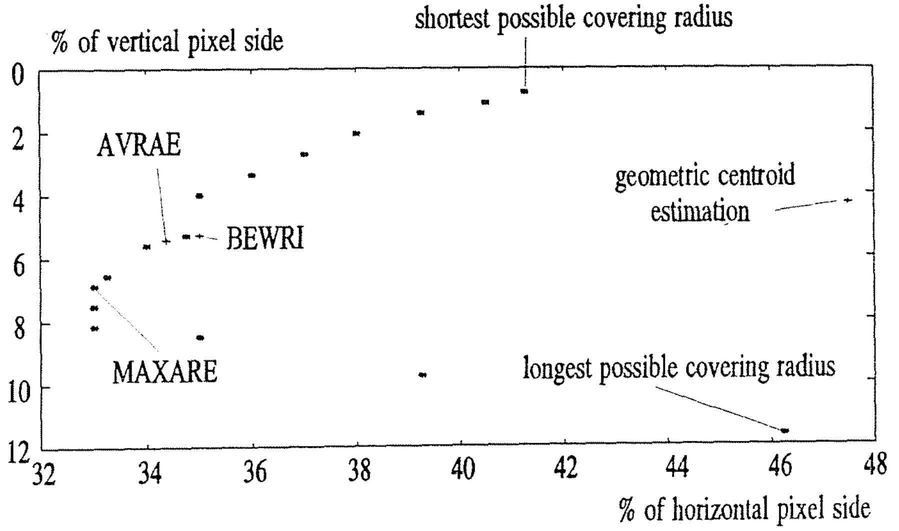

Figure 4.10. Different estimations for the centre of a marker image that covers the pixels hatched in Fig. 4.1.

The MAXARE and the AVRAE methods were tested by simulation and the gained results were compared to that of the BEWRI method. Both the MAXARE and the AVRAE results are close to the results of the BEWRI, as shown in Fig. 4.11. and 4.12. In Fig. 4.11. the MAXARE approximation is compared to the BEWRI method. It is clear that the approximation is excellent

up to mid-size marker images ($r \leq 6$). Even with relatively big marker images ($r = 8$) the deviations of the projections are not more than about 5%.
In Fig. 4.12. the MAXARE and the AVRAE approximations are compared to each other. The differences are subtle, no tendency can be found as the marker image radius increases. The figures were drawn based on a simulation when the pixel was supposed to be asymmetrical, the ratio of the neighbouring sides was 1.56.
Although the MAXARE and the AVRAE methods require less computation than the BEWRI method, their real-time application is still strongly limited.

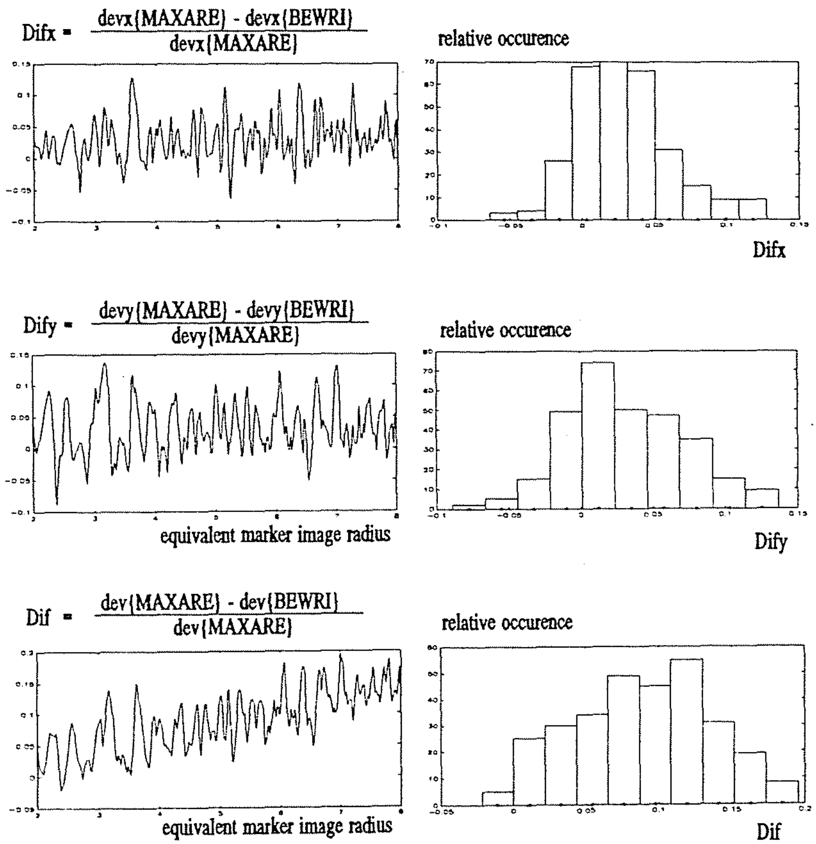

Figure 4.11. Comparing the MAXARE approximation to BEWRI. Asymmetrical pixel is used with a ratio of the neighbouring sides 1.56.

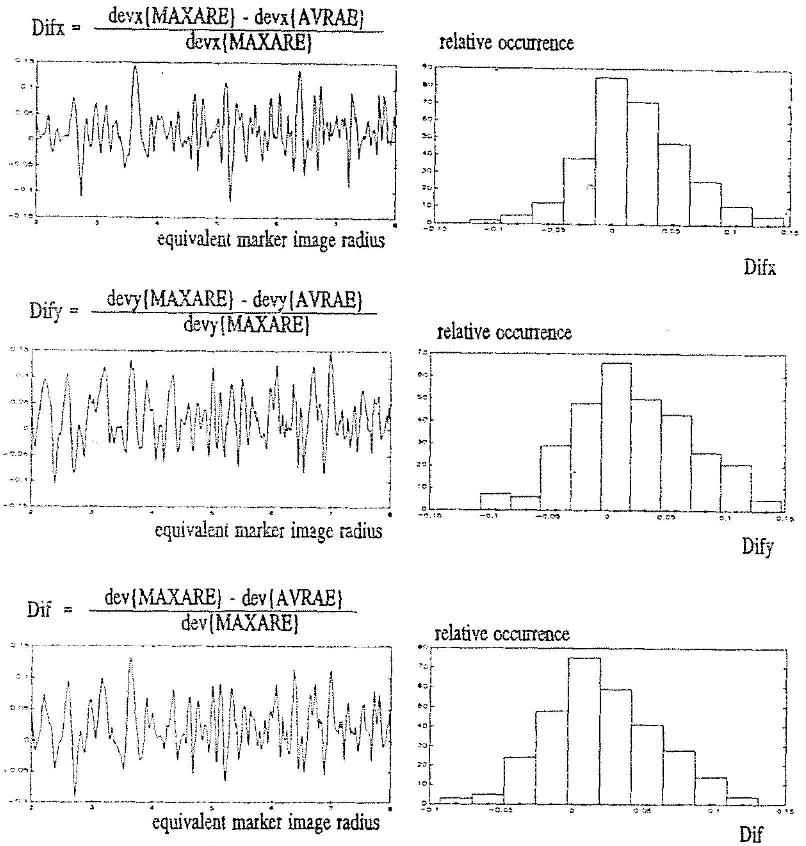

Figure 4.12. Comparing two approximations of BEWRI: the MAXARE and the AVRAE. Asymmetrical pixel is used with a ratio of the neighbouring sides 1.56.

Realisation of the ring fitting method

For the realisation of the method iteration can be applied which starts from the geometric centroid of a binary marker image. The parameters of the iteration can be set according to the requirements of the application. While realising the ring fitting method during the simulation the simple gradient method was used for the iteration. Different values were tested for the constants, determining the horizontal and vertical step sizes during the iteration. The results in the figures of this chapter were derived with a medium step size, resulting in the termination of the iteration in an average of 11 steps even with relatively big markers (diameter = 16 equivalent square shaped pixel sides). Further decrease in the step sizes substantially increases the number of necessary iteration steps while the increase in the accuracy is negligible. Using the half of the above medium steps meant an almost three-fold increase in the average number of iteration steps (29 for the same large marker image) while the accuracy hardly improved (less than 2% relative to the medium size steps). Nevertheless it means, that the accuracy of the ring fitting *method* is *slightly better* compared to the accuracy of its realisations, what is given in the figures of this chapter. Fig. 4.14. shows the contour map of ring widths for the binary marker image of Fig. 4.13. The binary marker image can be generated with ideal circular images (of different radii) if their midpoint is within the contour line belonging to ring width = 0.

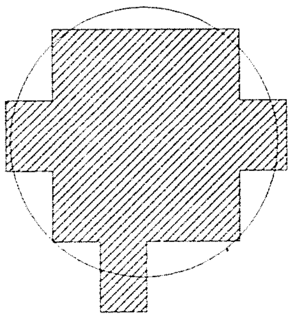

Figure 4.13.The realisation of the ring fitting algorithm is demonstrated using this binary marker image. One possible covering circle is shown.

Fig. 4.15. shows how the iteration advances for this binary marker image, starting from the geometric centroid. As it can be seen, the simple gradient method was applied. The exit criterion is that the actual ring width is not better than any of the previous two values. The point that corresponds to the widest ring width during the iteration is the output result, i.e. the estimated midpoint for all the possible covering marker images. Using bigger steps decreases the necessary iteration cycles but also the accuracy. During the simulation a relatively small step size was applied to achieve a good approximation of the point belonging to the maximal ring width. In order to test the accuracy of the iteration procedure, the ring widths, belonging to the output results were evaluated. As ideal circular marker images were used during the simulation, there is a covering ring with a positive ring width to each marker image. However, a percentage of the ring widths, belonging to the output result was found to be negative, cf. Fig. 4.16. It follows that it is possible to find a better realisation of the ring fitting method, yielding even more accurate results than those depicted here.

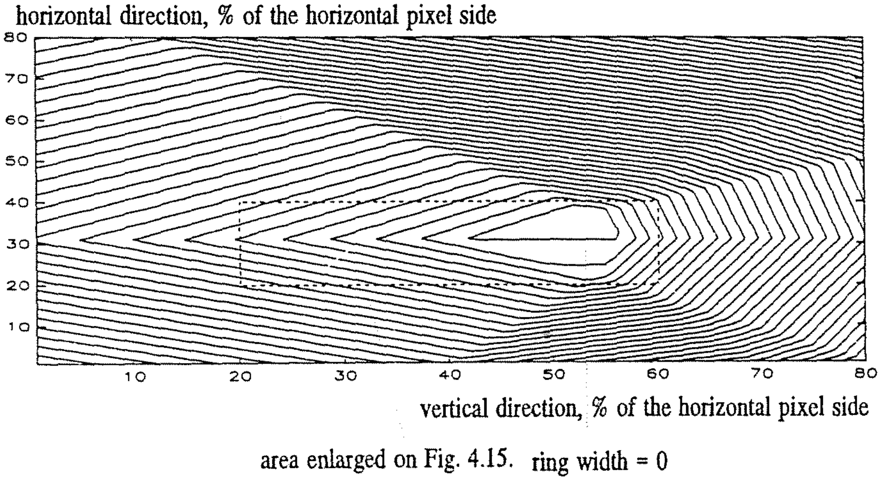

Figure 4.14. The contour map of the ring widths belonging to the binary marker image shown in Fig. 4.13.

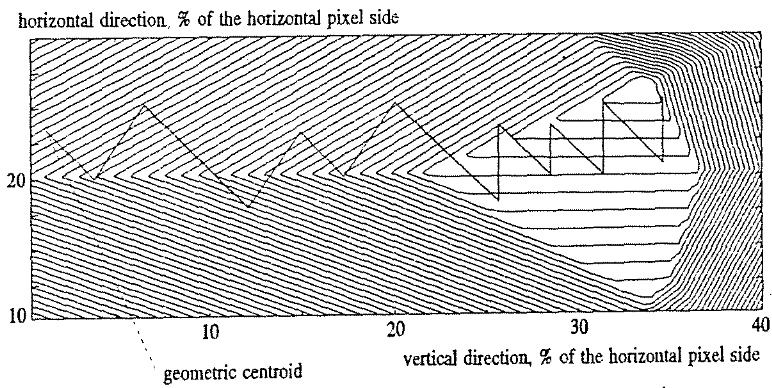

Figure 4.15. The iteration steps for a binary marker image on the contour map reflecting the corresponding ring widths.

The gradient method based iteration was programmed in C language for a RISC Evaluation Board with 16 MHz clock frequency applied in an experimental PRIMAS system. One relatively big (having 20 segments) or four medium size (each having 8 segments) marker images could have been processed in real-time. The increase in the clock frequency for the RISC board to be

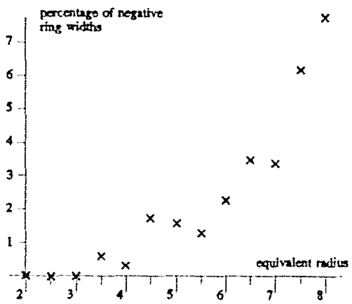

Figure 4.16. The applied iteration method resulted in negative ring width in some cases.

incorporated into the final version is more than twofold, which means that the realisation of the ring fitting algorithm even in its present form allows for practical applications.

The new centre estimation methods are beneficial regarding both the maximum value and the standard deviation of the distances between the actual and the estimated centres of the randomly projected marker images. Fig. 4.17. and Fig. 4.18. show the standard deviations of the above distances, Fig. 4.19. shows the maximum values of the geometric centroid estimation compared to the BEWRI method (upper diagrams) and to the ring fitting method (lower diagram).

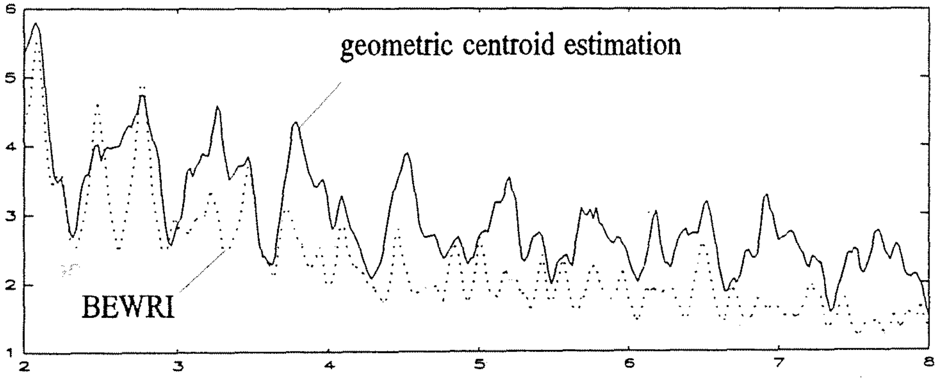

Figure 4.17. Standard deviations of the distances between the actual and the estimated centres of marker images with different radii, expressed as percentage of the equivalent square shaped pixel side.

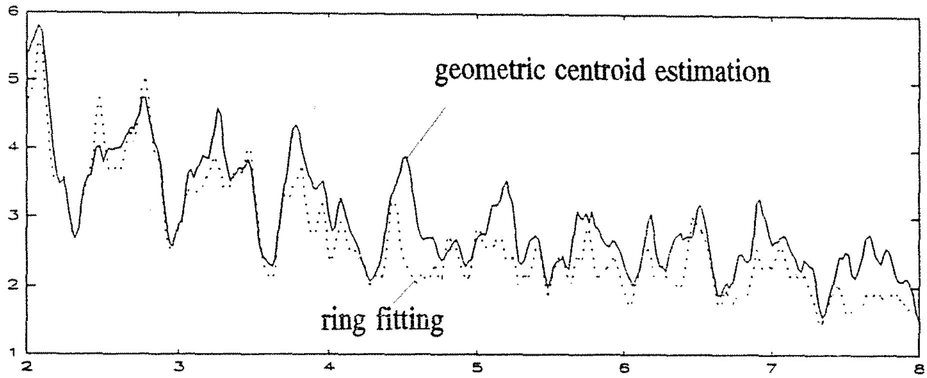

Figure 4.18. Standard deviations of the distances between the actual and the estimated centres of marker images with different radii, expressed as percentage of the equivalent square shaped pixel side.

4.4. THE EFFECT OF DISTORTED MARKER IMAGES

Two basic sources of distortion were investigated: noise and occlusion. The effect of noise was taken into account during the simulation by adding a random noise to the radius of the marker image. The segments of a binary marker image were determined based on the centre and the radius of a marker image. The actual value of r_n was computed with a new ξ both at the beginning and at the end of each segment.

$$r_n = r + m * \sqrt{ratio} * \xi \tag{4.19}$$

where *ratio* is the ratio of the vertical and the horizontal pixel sides, ξ is a random variable with uniform distribution between -1 and 1 and m is the measure of the maximum possible deviation, $0 \leq m \leq 1$. If $m = 1$ then the maximal deviation is 1 equivalent square shaped pixel side both at the beginning and at the end of each segment. Figures 4.20. and 4.21. show the result if $m = 0.25$ and $m = 0.5$, respectively. The difference between the accuracy of the two methods decreases with increasing noise level, which is in harmony with the expectations. The higher the noise level is the more influence it has on the accuracy of the estimation independent of the estimation method itself.

However, the ring fitting method gives substantially better results even in the case of $m = 0.5$, which exceeds the usual noise level.

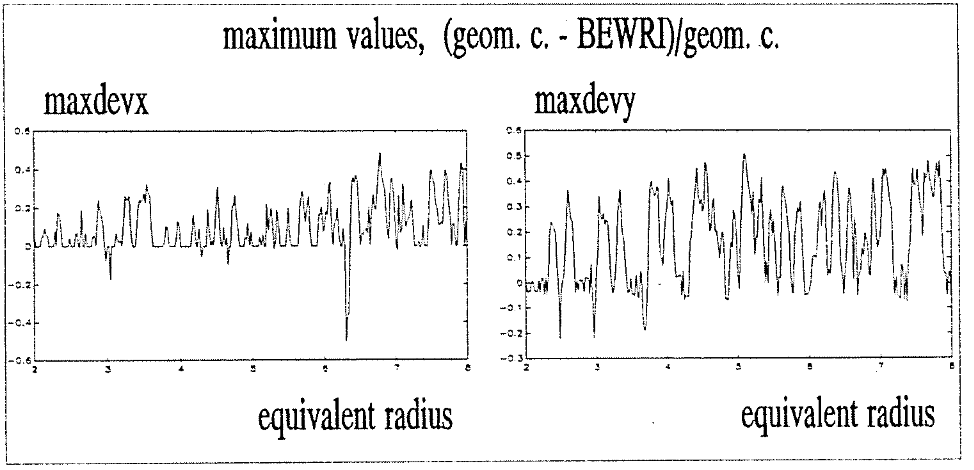

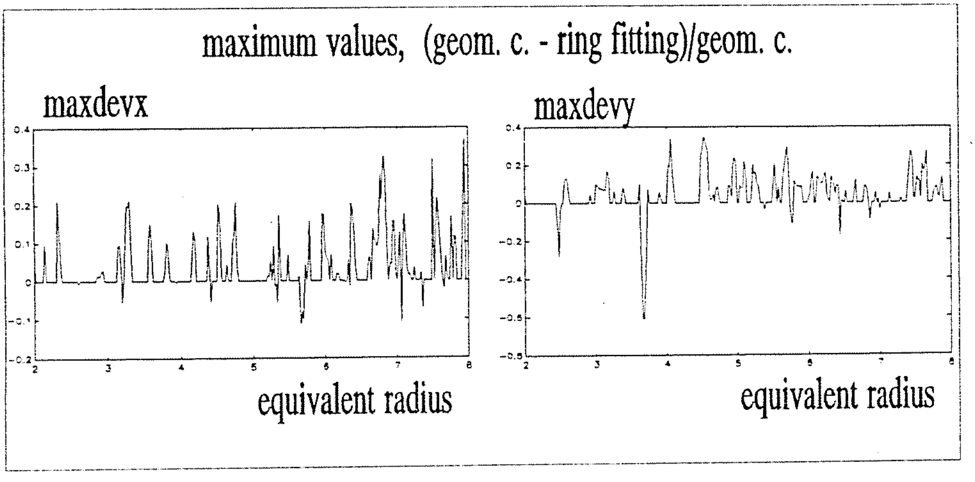

Figure 4.19. Maximum values of the distances between the actual and the estimated centres of randomly projected marker images vs. equivalent marker image radius.

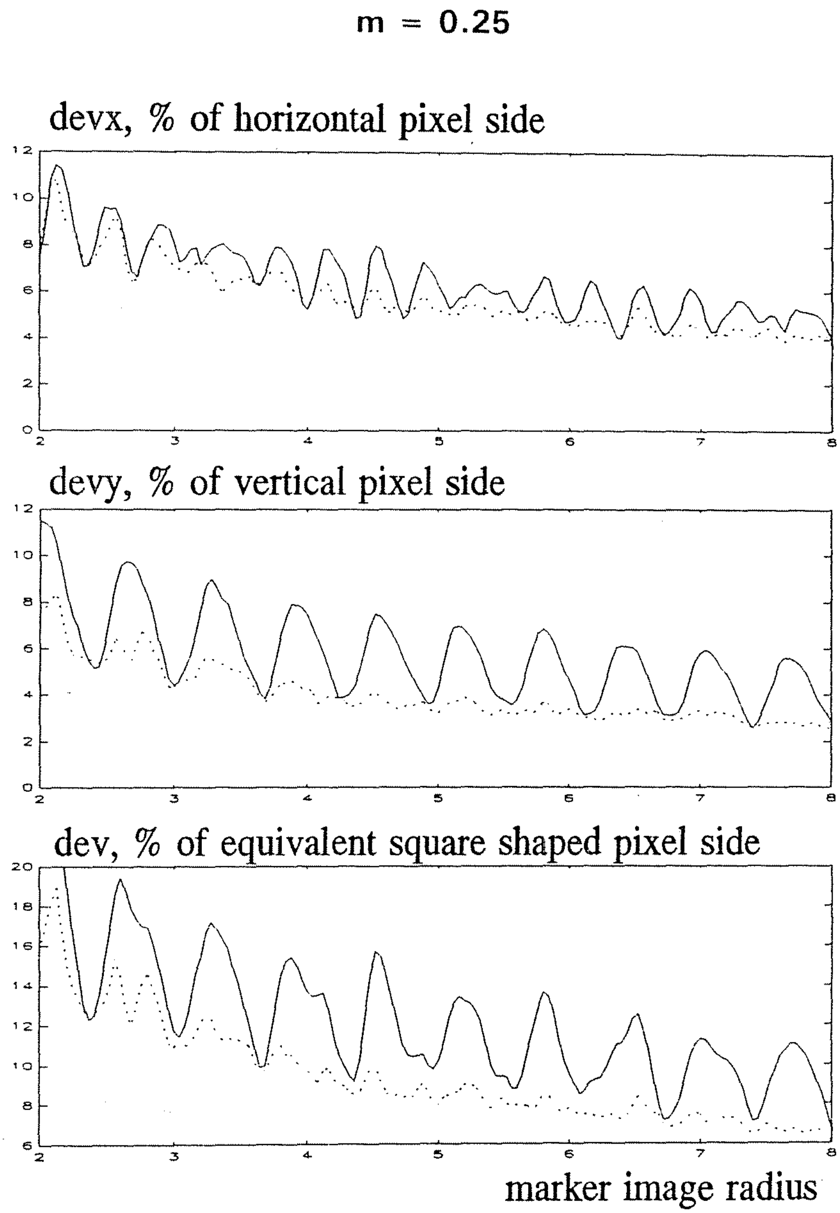

Figure 4.20. Comparing the geometric centroid calculation (solid line) with the ring fitting method (dotted line) using noisy data.

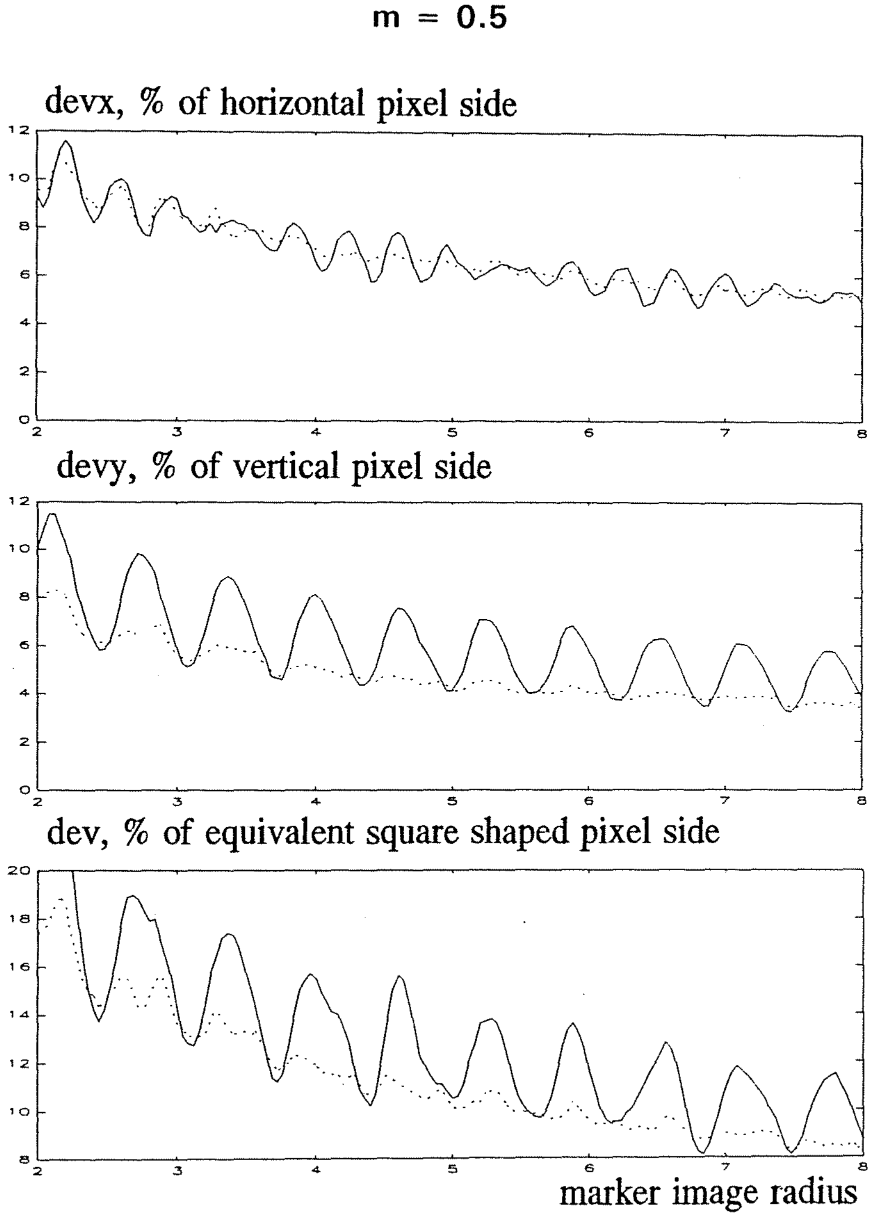

Figure 4.21. Comparing the geometric centroid calculation (solid line) with the ring fitting method (dotted line) using noisy data.

The other source of distortion is occlusion. Should it be caused by another marker, it is called overlapping. The clustering of the distorted images was dealt with in section 2.4. Once the segments are clustered the different methods give different estimations for the centre coordinates of the image of a distorted marker. The circle fitting algorithm can give the most accurate estimation, but only if the points, which are *not* on the circumference are discarded. In Fig. 4.22. the points to be discarded are 1, 3 and 5. However, an effective algorithm for discarding such points has not been found yet.
The application of *template matching* improves the midpoint estimation of distorted images. Ferrigno, in (ed. Walton, 1990) describes a realisation of template matching used in the ELITE system. The cross correlation with predefined patterns not only improves the accuracy of marker midpoint determination but also allows for smaller markers to be tracked. A two level hierarchical structure serves for recovering 3D coordinates. The first level is a SIMD hardware while the second level is in software. A drawback of template matching is that several predefined patterns are needed in the general case, when the marker image size is unknown.
A helpful information would be the measure of distortion, characterising how close the covering image is to the ideal circular shape. It can easily be understood that the residual value of the error function (EF_2, cf. equation 2.11) during circle fitting is not suitable for this purpose. On the one hand points on a straight line would result in $EF_2 = 0$ (with infinite radius), on the other hand different shapes might give the same value because of the quadratic summation of the deviations.
In connection with the ring fitting method I introduced the width of the ring as the measure of the deviation from the ideal circular shape. If the width is positive then the marker image is either ideally circular or the deviation is hidden by the quantisation. The correct interpretation is that the shape of the covering
marker image *might be* ideally circular if the width of the fitted ring is positive. It is important to be emphasised that the width of the fitted ring does not characterise the accuracy of the estimation, because the *binary marker image itself* might be different from the one, corresponding to the marker image in the ideal case. Negative ring width, according to equation 4.12., signals that the covering image is not ideally circular. To get a characteristic result, independent of magnification, the ring width is to be divided by the height of the covered set. The height is similar to the diameter in the case of a circle but can very easily be determined. If the ratio of the ring with and the diameter of the image is a small negative value then the deviation from the ideal circle can be the result of either occlusion or noise.

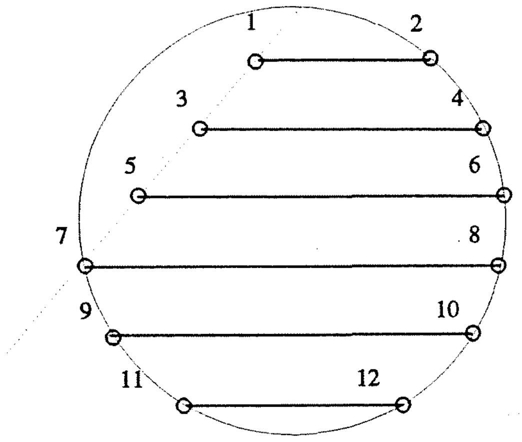

Figure 4.22. The segments of an occluded marker image. The endpoints of the segments are numbered.

4.5. THESES FROM THE CHAPTER

Thesis 3.

I worked out a method - BEWRI, Best Estimate Without Radius Information - which gives optimal results regarding the accuracy of centre estimation, without knowing the radius of the marker image and using CF_{sd} as cost function. The centres of gravity of the areas, belonging to all possible covering radii should be determined and their weighted average should be calculated. The weighting factors are the sizes of the areas.

$$\text{BEWRI(binary marker image)} = \frac{\int_{r_1}^{r_2} A(r)CG[A(r)]dr}{\int_{r_1}^{r_2} A(r)dr}$$

where CG[A] is the centre of gravity of area A, r_1 is the shortest, r_2 is the longest radius of the covering marker images and A(r) is the area, along which the centre of a covering image with radius r can be anywhere to generate the binary marker image.

The BEWRI estimate is not necessarily optimal for all the possible radii separately, but it is optimal for a binary marker image if CF_{sd} is the cost function.

I showed that BEWRI gives more favourable results than the conventional estimation methods also regarding the maximal value and the variance of the deviations between the actual and the estimated centres of marker images. I showed that the results are only slightly different if the cost function, used to characterise accuracy is the expected value of the distance between the actual and the estimated centres of a marker image.

Thesis 4.

4.1. I worked out a method (ring fitting), the accuracy of which approximates the accuracy of BEWRI and is appropriate for real-time applications. The ring width is defined in the following way: given the centre point of the ring, the distance between it and the midpoint of the covered pixel being farthest from it should be subtracted from the distance between the centre point of the ring and the midpoint of the closest not covered pixel. The ring fitting method relates to a binary marker image, generated by an ideal circular marker image, a point as centre point so that drawing circles around it the range of the possible covering radii is maximal.

4.2. I showed that the method inherently provides a measure for the distortion of circular marker images. No such measure can be related to the conventional centre estimation methods. If the marker image, generating the binary marker image is an ideal circle, there is at least one point, to which positive ring width belongs. In case of binary marker images caused by distorted marker images the corresponding maximal ring width can be *negative*: the greater is the ratio of two perpendicular sections, that can be placed onto the covered set of pixels the greater negative value results for the ring width.

4.3. I showed that the ring fitting gives significantly better estimates in the case of noisy images than the conventional methods, using CF_{sd} as cost function.

5. CONCLUSIONS

In this chapter the new theoretical results are summarised and evaluated. They are also compared with the methods known from the literature. Measurement data, gained by using the PRIMAS system with different marker centre estimation methods are also given and evaluated. Finally, those problems are pointed out, which are worth further investigations.

5.1. EVALUATION OF THE THEORETICAL RESULTS

Having defined the resolution of marker image centre estimation it is shown in Chapter 3. that *the resolution is basically determined by the number of covered pixels of a binary marker image.* Regarding the tendency of the resolution, it increases as the number of covered pixels increases, but considering small differences the relation might even be reversed.

Resolution, expressed in distance unit, depends only negligibly on the ratio of the neighbouring sides of a pixel and there is no significant difference between the horizontal and the vertical resolutions.

The accuracy of the different marker image centre estimation methods has been evaluated. The accuracy of the most popular method, that of the geometric centroid estimation was first investigated by (Winter et al., 1972a). The computational power available at that time explains that they computed the accuracy corresponding to only nine different marker image radii. Neither a detailed description of the method used nor a precise definition of the accuracy is given. Their results show that increased accuracy can be achieved if the marker image increases. Our results, computed by simulation for the geometric centroid estimation reflect the same trend but the small step size in the marker image radius allowed for discovering the oscillatory characteristic as well. In Fig. 5.1. the solid line shows the accuracy data gained by us using simulation. Of the above mentioned nine marker image radii three fall into the given range, they are included in the figure using x marks.

The theoretical limit of accuracy has been defined for binary marker images. This limit can be reached if the radius of the covering circle is known. The cost function is defined supposing the marker image is projected randomly on the sensor surface with uniform distribution. If the cost function is the expected value of the squared distance between the actual and the estimated centres of a marker image then the best estimate is the centre of gravity of the area, along which the centre of the covering image with fixed radius can be anywhere to result in the given binary marker image. If the cost function is the expected value of the distance between the actual and the estimated centres of a marker image then the best estimate cannot be analytically determined. It can be approximated by a point: its x, y coordinates are the median points of the x, y coordinates of all the points along the above defined area. It has been found that there is no significant difference between the results gained by using the two different cost functions.

In practical applications the theoretical limit cannot be reached as the radius of the covering image is unknown. Based on the binary marker image, the range of the possible covering radius can be determined. A method has been formulated (BEWRI) which takes into account all the possible values of the covering radius and results in an optimal estimate *without knowing the actual radius.* The estimate is optimal for a binary marker image if the cost function is the expected value of the squared distance between the actual and the estimated centres of the possible covering marker images, cf. Eq. 3.19.

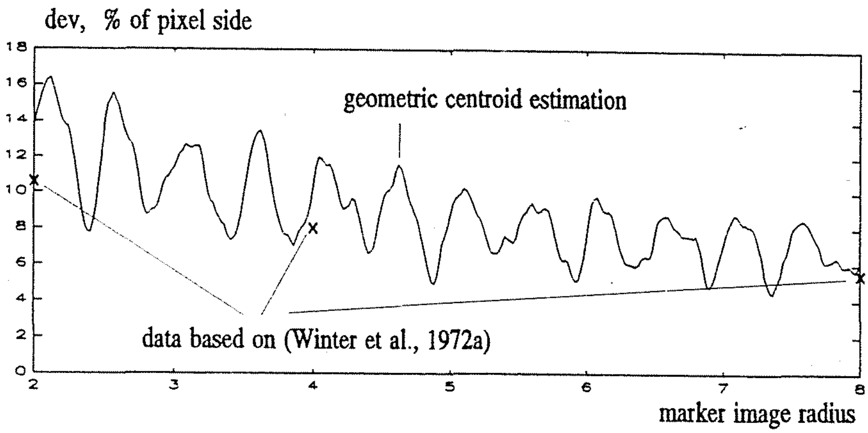

Figure 5.1. The comparison of the accuracy data of our simulation coincides with those calculated in (Winter et al., 1972a).

The BEWRI procedure provides the minimum of the cost function by yielding as the estimated midpoint of a binary marker image the weighted average of the centres of gravity of the areas, along which the centre of the covering image with radius **r** can be anywhere to produce the given binary marker image. The weighting factor is the area belonging to a fixed **r** radius, which is varied from the minimal to the maximal possible covering value, cf. Eq. 4.1. and Eq. 4.2. If the cost function is modified then the centre of gravity of each area must be replaced accordingly.
Three methods have been worked out which approximate the BEWRI results. Both the MAXARE and the AVRAE procedures first select a possible covering radius of high probability for a binary marker image and then, *considering this radius to be the covering radius,* calculate the estimated centre. The MAXARE procedure selects the radius, to which the maximal area belongs, along which the centre of the covering image may be anywhere to produce the given binary marker image. The AVRAE procedure selects the average of the minimal and the maximal possible covering radii. Supposing the covering marker image as known both MAXARE and AVRAE calculate the estimated midpoint the same as described at the theoretical limit of accuracy.
The ring fitting method relates to a binary marker image that point as the estimated midpoint, around which the range of the possible covering radius is maximal, i.e. around which the widest ring can be placed.
In Chapter 3 the accuracy of the conventional and the new estimation methods are compared using simulation and supposing ideal circular images, scanning a wide range of marker image radii. Regarding the accuracy the methods belong to three classes. The BEWRI method approximates the theoretical limit of accuracy the best. The MAXARE, AVRAE and ring fitting methods give results close to each other and their accuracy is not far from that of BEWRI. The conventional algorithms, circle fitting and geometric centroid estimation have about the same accuracy, which is

substantially worse than that of the new algorithms. The conventional algorithms have a further drawback: the local variations in their accuracy (if the elementary pixel is rectangular with longer vertical side then especially in the vertical accuracy) is high. Table 5.1. gives a short comparison of the methods. The data were derived with the following assumptions:

- asymmetrical pixels, ratio = 1.56,
- marker image radius varies between 6.5 and 7 equivalent square shaped pixel sides.

The expected value of the deviation between the actual and the estimated centres of a randomly projected marker image is given as a fraction of the radius. The horizontal and the vertical projections of this deviation are also given, expressed as percentages of the corresponding pixel sides.
To get a simple 'figure of merit' for each method, roughly characterising their accuracy corresponding to the given marker size, relative values have been computed. Table 5.2. is composed on the basis of the average values of Table 5.1. The average values of each method are divided by the average values of the geometric centroid calculation method. It means that in this table the accuracy is the better the smaller this ratio is.

method	dev, % of r		devy, % of vertical pixel side		devx, % of hor. pixel side	
	range	average	range	average	range	average
theor. limit	0.38... 0.50	0.45	2.0... 2.9	2.45	1.4... 2.2	1.80
BEWRI	0.44... 0.56	0.50	2.5... 3.4	2.95	1.7... 2.4	2.05
ring fitting	0.56... 0.75	0.66	3.0... 3.7	3.35	1.9... 3.1	2.50
geom. centr.	0.77... 1.29	1.03	4.0... 6.4	5.20	2.8... 6.0	4.40

Table 5.1. The accuracy of different methods supposing asymmetrical pixels. The marker image radius varies between 6.5 ... 7 equivalent square shaped pixel sides.

method	ratio of averages dev	devx	devy
theor. limits	0.43	0.48	0.42
BEWRI	0.48	0.56	0.45
ring fitting	0.63	0.63	0.56
geometric centr.	1.0	1.0	1.0

Table 5.2 Expressing the accuracy of each method compared to that of geometric calculation.

The ring fitting method inherently provides a measure of distortion for circular images. If the width of the fitted ring is negative (cf. section 4.4) it means that the image causing the binary marker image cannot be circular. If the negative ring width is relatively small compared with the radius of the image then the distortion might as well derive from random noise while a relatively big negative ring width is certainly caused by occlusion.
Template matching also provides a measure of distortion but it has the disadvantage that in the general case several different size templates must be tried out. The oscillatory nature of the relations obtained for the resolution and accuracy of marker image centre estimation with simulations, which have used a near continuum of marker image sizes, should not detract from the obvious general trend. In practical applications, the apparent marker size is varying to the extent that transverse distance to the sensor system varies, so there is little to gain for the investigator to accommodate the marker size to any local minimum in the curves presented. By smoothing the results, the general trend in accuracy vs. marker radius r was found to be proportional to the relation: $1/\sqrt{r}$.

5.2. EVALUATION OF THE MEASUREMENT RESULTS

I could perform the measurement series, depicted in this dissertation in the Motion Studies Laboratory of Delft University of Technology using the PRIMAS system (cf. section 2.2.). Naturally I have to restrict the delineation of the results to those being closely related to the new theoretical achievements. It is essential in order not to cause handicap to the manufacturer of the system in the business competition.
The first step was the test of the precision - i.e. the reproducibility - of the system and the measurement setup. Circular disks, placed perpendicularly to the camera axis, were used as static markers.
The CCD sensor, applied in the camera has 604 columns and 288 lines, the pixel size is 10 μm (horizontal) $\times$ 15.6 μm (vertical). This means that the width/height ratio of the field of view (FOV) is $1.344 \approx 4:3$. The result of the centroid estimation is represented on 15 effective bits. The marker segment processor performs a scaling during geometric centroid calculation before dividing two integer numbers (cf. Eq.2.6.). The scaling factor is 256/5 horizontally and 512/5 vertically resulting in a

resolution in data representation 1:30924.8 and 1:29491.2 respectively. Thus the smallest possible difference in the representation of the centre coordinates, 1 LSB - also will be called 'unit' - corresponds to 1.95 % of the horizontal pixel side and 0.98 % of the vertical pixel side while specifying the x,y coordinates of a marker centre. One horizontal unit, expressed in distance, corresponds to 1.27 vertical unit. In the case of a 2m $\times$ 1.5m FOV this means 1 horizontal unit $\approx$ 0.065 mm or 65 μm and 1 vertical unit $\approx$ 0.051 mm or 51 μm.
The position of a stationary marker with 13 segments was measured. The FOV was 1m $\times$ 0.75m, sampling with 100 Hz the recording lasted for 10 s yielding 1000 estimates for the marker centre. The data were processed by an ASYST program to get the mean value and the standard deviation. With the same measurement setup 3 different marker centre estimations were used: geometric centroid calculation (Eq.2.6.), weighted averaging of the segments using the squared segment widths as weights (Eq.2.7.) and circle fitting. The results are summarised in Table 5.3.

	X_c	st.dev.	Y_c	st.dev
geom.centroid calc.	11118.4	1.15	14151.6	0.78
squared weights	11119.8	1.33	14145.3	2.33
circle fitting	11119.7	1.50	14137.5	1.63

Table 5.3. Mean values and standard deviations - expressed in *units* - of the measured centre coordinates using a static marker.

The results show a good short term stability. The measurement was repeated occluding the lower 6 segments. The results are in Table 5.4.

	X_c	st.dev.	Y_c	st.dev
geom.centroid calc.	11091.0	1.85	14806.8	0.97
squared weights	11093.2	1.90	14761.6	1.47
circle fitting	11091.5	2.70	14321.5	10.6

Table 5.4. Results with the same measurement setup (cf. Table 5.3.) and occluding the lower 6 segments of the marker image.

The results show that
- the mean values for the X_c exhibit much smaller deviations than for Y_c,
- with a distorted marker image, where only whole segments are occluded, the circle fitting gives much more accurate results for Y_c but its precision is worse than that of the other methods.

The measurement with an ideal circular marker was repeated using the geometric centroid calculation and the ring fitting method. The sampling rate was 50 frames/s, the recording lasted for 8 s yielding 400 estimates. The distribution of the estimates for the marker centre is presented in Fig.5.2. The size of a rectangle in the grid is 1 horizontal unit × 1 vertical unit.

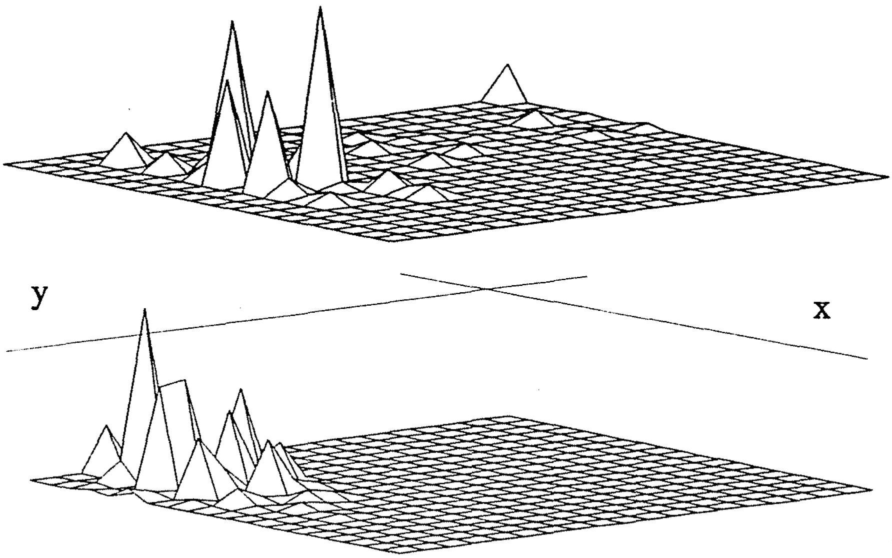

Figure 5.2. Estimates of the centre position of a stationary marker using ring fitting (top) and geometric centroid calculation (bottom).

Experiences using the ring fitting estimation method show that

- in order to exploit its favourable accuracy fully the centre coordinate representation must be increased from the present 15 bits,
- the iteration method must be replaced by a more effective algorithm,
- a detailed system noise analysis is required.

6. REFERENCES

Abdel-Aziz, Y. and Karara, H.M.(1971) *Direct Linear Transformation From Comparator Coordinates In Object-Space Coordinates In Close-Range Photogrammetry.* ***Proc. ASP, Urbana Ill.***, 1-18.

D'Amico, M., Ferrigno, G.(1992) *Comparison between the more recent techniques for smoothing and derivative assessment in biomechanics.* ***Med. & Biol. Eng. & Comput., 1992*****, 30.** 193-204.

Andrews, B.J.(1982) *On-line Locomotion Analysis Using Television Techniques.* ***PhD Thesis***, 1982. Strathclyde University, Glasgow.

Balch, K.S.(1991) *Techniques for capturing over 10.000 images/second with intensified imagers.* ***Proc.of SPIE, vol. 1358, Bellingham, WA USA*** 358-372.

Borghese, N.A., Ferrigno, G.(1990) *An Algorithm for 3-D Automatic Movement Detection by Means of Standard TV Cameras.* ***IEEE Trans. on BME, Vol. 37. No. 12.*** 1221-25.

Bruegger, W. and Milner, M.(1978) *Computer-Aided Tracking Of Body Motions Using A CCD Image Sensor.* ***J.MBEC 16, March 1978.*** 207-210.

Cappozzo, A., Marchetti, M. and Tosi, V. (eds) (1992) *Biolocomotion: A Century Of Research Using Moving Pictures.* ***Promograph-Roma-Italy, 1992.***

Collet, M.(1985) *Make Way For Solid-State Imagers.* ***Photonics Spectra, Sept. 1985.*** 103-112.

Costigan, P.A., Wyss, U.P., Deluzio, K.J., Li, J.(1992) *Semiautomatic three-dimensional knee motion assessment system.* ***Med. & Biol. Eng. & Comput., 1992*****, 30.** 343-350.

Chao, E.Y., An, K.N., Askew, L.J. and Morrey, B.F.(1980) *Electrogoniometer For The Measurement Of Human Elbow Joint Rotation.* ***J.Biomech. Eng., 102,*** 301-310.

Chernov, N.I. and Ososkov, G.A.(1984) *Effective Algorithms For Circle Fitting.* ***Computer Physics Communications 33 (1984)*** 329-333.

Das, G.B.(1949) *A Mathematical Approach to Problems in Photogrammetry.* ***Empire Survey Review, Vol. X., No. 73. July, 1949.***

Dinn, D.F., Winter, D.A., Trenholm, B.G.(1970) *CINTEL - Computer Interface for Television.* ***IEEE Trans. on Computers, 1970.*** 1091-95.

Downs, J., Halperin, H.R., Humphrey, J., Yin, F.(1990) *An Improved Video-Based Computer Tracking System for Soft Biomaterials Testing.* ***IEEE Trans. on BME, Vol. 37. No. 9.*** 903-907.

Feddern, U. and Zur Verth, S.(1984) *The Frame-Transfer Sensor: An Attractive Alternative To The TV Camera Tube.* ***Electronic Components and Applications. Vol.6. No.4. (1984)*** 223-229.

Ferrigno, G. and Pedotti, A.(1985) *ELITE: A Digital Dedicated Hardware System For Movement Analysis Via Real-Time TV Signal Processing.* ***IEEE Trans. on BME, vol. BME-32,*** 943-950.

Ferrigno, G., Gussoni, M.(1988) *Procedure to automatically classify markers in biomechanical analysis of whole-body movement in different sports activities.* ***Med. & Biol. Eng. & Comput.,*** **26.** 321-324.

Fioretti, S., Leo, T., Pisani, E., Corradini, M.L.(1990a) *A computer-aided movement analysis system.* ***IEEE Trans. on BME, vol. 37. No. 8.*** 812-819.

Fioretti, S., Jetto, L., Leo, T.(1990b) *Reliable In Vivo Estimation of the Instantaneous Helical Axis in Human Segmental Movements.* ***IEEE Trans. on BME,*** 398-409.

Furnée, E.H.(1967) *Hybrid Instrumentation In Prosthesis Research.* ***Digest 7th Int. Conf. Med. & Biol. Eng., Stockholm,*** 446.

Furnée, E.H.(1970) *Graphic input to a digital computer by means of a TV-camera.* ***Abstr. IMEKO V, Versailles, May 25-30, 1970.*** 509.

Furnée, E.H.(1984) *Intelligent movement measurement devices I.: video converter with real-time marker processor.* ***Proc. 8th Int. Symp. Ext. Control Human Extremities, ETAN Belgrade, 1984.*** Supp. 39-41.

Furnée, E.H., Halbertsma, J.M., Klunder, G., Miller, S., Nieukerke, K.J., van den Burg, J. and van der Meché(1974) *Automatic Analysis Of Stepping Movements In Cats By Means Of A Television System And A Digital Computer.* ***Journal of Physiology, 240,*** 3-4.

Furnée, E.H.(1989) *TV/Computer Motion Analysis Systems: The First Two Decades.* ***PhD thesis*** Oct. 1989. Delft University of Technology. ISBN 90-9003095-6.

Furnée, E.H.(1990) *A TV/Computer Movement Measurement System, Using A-Priori and Trajectory Data in Real Time* ***VDI Berichte, NR.856*** 125-132.

Furnée, E.H., Sabel, J.C., van Veenendaal, H.L.J., Jobbágy, Á.(1992) *3-D Performance Characterization In Motion Analysis Systems: An Example.* ***Conf. proc. of Gait Analysis Symposium, 1992. Zürich,*** 280-283.

Furnée, E.H., Jobbágy, Á.(1993) *Precision 3-D Motion Analysis System For Real-time Applications.* invited paper for ***Microprocessors and Microsystems, Vol.17., Nr.4., May 1993.*** 223-231.

Given, D.(1988) *CCD vs. Silicon Photodiode Technology for 3D Motion Analysis* ***Sensors, 1988. Sept.*** 81-87.

Hatze, H.(1988) *High-Precision Three-Dimensional Photogrammetric Calibration and Object Space Reconstruction Using a Modified DLT Approach.* ***J. Biomechanics, Vol.21. 1988.*** 533-538.

Jarrett, M.D.(1976) *A TV/Computer System For Human Locomotion Analysis.* ***PhD thesis*** July 1976. University of Strathclyde, Glasgow.

Jobbágy, Á., Furnée, E.H., van Veenendaal, H.L.J.(1991) *New Algorithms For Real-Time Marker Centre Estimation In Motion Analysis.* ***Proc. of the 2nd International DSP Associates Conf. on DSP Applications and Technology, Berlin, 1991.*** 489-498.

Jobbágy, Á.(1992) *Resolution And Accuracy Of Motion Analysis Using CCD Based Cameras And Reflecting Markers.* ***Proc of the Seventh Symposium On Microcomputer And Microprocessor Applications, Budapest, April 22-24, 1992.*** 471-478.

Jobbágy, Á., Furnée, E.H.(1993a) *New Marker Centre Estimation Algorithms Of High Accuracy In Motion Analysis.* (accepted paper for ***Periodica Polytechnica, Ser. El. Eng.***)

Jobbágy, Á., Furnée, E.H.(1993b) *Marker Centre Estimation Algorithms In CCD Camera Based Motion Analysis.* (accepted paper for ***Medical & Biological Engineering & Computing***)

Keemink, C.J., Hoek van Dijke, G.A., Snijders, C.J.(1991) *Upgrading of efficiency in the tracking of body markers with video techniques.* ***Medical & Biological Engineering & Computing, vol. 29. no. 1.*** 70-74.

Kemp, B., Franzen, J.M., Buruma, O.J.S. and Roos, R.A.C.(1982) *Quantification Of Random Body Movements By A Doppler Radar Device.* ***Med. & Biol. Eng. & Comput., Sept. 1982.*** 539-544.

Lindholm, L.-E., Öberg, K.E.T.(1974) *An Optoelectronic Instrument For Remote On-line Movement Monitoring.* ***In (ed. P.A.Neukomm) Proc. of the 2nd Int. Symp. Biotelemetry, Karger, Basel 1974.***

Macellari, V.(1983) *COSTEL - A Computer Peripheral Remote Sensing Device For 3-Dimensional Monitoring Of Human Motion.* ***Med. & Biol. Eng. & Comput., 21#3.*** 311-318.

Medved, V., Tonkovic, S.(1991) *Method to evaluate the skill level in fast locomotion through myoelectric and kinetic signal analysis.* ***Med. & Biol. Eng. & Comput., 1991,*** **29**, 406-412.

Mesqui, F., Niederer, P.(1981) *Motion Analysis Of Simulated Vehicle - Pedestrian Impacts Using Automated Highspeed Cinephotogrammetry.* ***SPIE 427: Highspeed Photography, Videography And Photonics, 1981.*** 250-257.

Miller, N.R.(1980) *A Technique For Obtaining Spatial Kinematic Parameters Of Segments Of Biomechanical Systems From Cinematographic Data.* ***J.Biomechanics, Vol.13. 1980.*** 535-547.

Mitchelson, D.L.(1975) *Recording Of Movement Without Photography.* In: ***The Human Movement Studies. Whiting, H.T.A.(ed.) Series Lepus Books, London, 1975.***

Mitchelson, D.L.(1988) *Automated three dimensional movement analysis using the CODA-3 system.* ***Biomedizinische Technik (in German) 23#7, aug. 1988.*** 179-182.

Moura, L. and Kitney, R.(1991) *A Direct Method For Least-Squares Circle Fitting.* ***Computer Physics Communications 64 (1991)*** 57-63.

Oderkerk, B.J., Inbar, G.F.(1991) *Walking cycle recording and analysis for FNS-assistted paraplegic walking.* ***Medical & Biological Engineering & Computing, vol. 29. no. 1.*** 79-83.

Paul, J.P., Jarrett, M.O., Andrews, B.J.(1974) *Quantitative analysis of locomotion using television.* ***Abstr. World Congr. ISPO, Montreux, 8-12. Oct. 1974,*** 43.

Sabel, J.C.(1990) *Implementation Of SMAC In A 3D Motion Analysis System.* ***In Macellari, V. and Torre, M.(eds.) Proceedings of the Workshop Experience and New Programs, Rome, 1990. Dipartimento di Elettronica e Automatica, Ancona, 1990.*** 153-158.

Safee-Rad, R., Shwedyk, E., Quanbury, A.O.(1990) *Three-dimensional measurement system for functional arm motion study.* ***J.Med. & Biol. Eng. & Comput., 1990,*** 28, 569-573.

Sanderson, D.J., Cavanagh, P.R.(1986) *The Use Of Augmented Feedback To Modify Pedalling Mechanics.* ***Proc. of the North American Congress on Biomechanics. Montreal, 1986. Aug. 25-27.*** 297-298.

Simonyi, K.(1978) *A fizika kultúrtörténete* (in Hungarian) ***Gondolat Könyvkiadó, Budapest, 1978.***

van de Steeg, M.S.H., Peek, H.L., Bakker, J.G.C., Pals, J.A., Dillen, B.G.M.H., Oppers, J.M.A.M.(1985) *A Frame-Transfer CCD Color Imager with Vertical*

Antiblooming. ***IEEE Trans. on Electron Devices, Vol. ED-32, No.8. Aug. 1985.*** 1430-1438.

Steinwender, G., Hochmair, E.S., Berger, M., Holzmüller, G.(1992) *The 3-D Motion Measurement System Used in the Austrian-Soviet Space-Flight.* ***Proc. of the XIVth Annual Conf. of IEEE/EMBS, Paris, 1992. Oct.29.-Nov.1.*** 41-42.

Szirányi, T.(1991) *Új mérési és felismerési módszerek a képfeldolgozásban.* (in Hungarian) ***PhD thesis***, 1991.

Taylor, K.D., Mottier, F.M., Simmons, D.W., Cohen, W., Pavlak, R.jr., Cornell, D.P., Hankins, B.(1982) *An Automated Motion Measurement System For Clinical Gait Analysis.* ***J.Biomech., 15#7,*** 505-516.

Toet, D.J.(1991) *Simulation programs for the design of the light distribution for the PRIMAS system.* ***Graduation thesis*** in Dutch, TU Delft, Fac. Applied Physics, 1991.

van Veenendaal, H.L.J.(1992) *Recommendations for the next generation PRIMAS systems.* ***Graduatuion thesis***, TU Delft, Fac. Applied Physics, 1992.

Walton, J.S.(ed.)(1990) *Proc. Of Mini-Symposium On Image-Based Motion Measurement.* ***SPIE Vol.1356., 31.Aug. - 1.sept. 1990. University of California, San Diego La Jolla Calif., USA***

Webb, J.A., Aggarwal, J.K.(1982) *Structure from Motion of Rigid and Jointed Objects.* ***Artificial Intelligence, 19. (1982)*** 107-130.

Winter, D.A. and Reimer, G.D.(1972a) *Quantization Errors In Calculation Of Volumes, Areas And Coordinates In Medical Images.* ***Proc. of the SPIE vol. 32.*** 107-109.

Winter, D.A., Greenlaw, R.K., Hobson, D.A.(1972b) *Television-Computer Analysis of Kinematics of Human Gait.* ***Computers and Biomedical Research, Vol.5.,*** 498-504.

Winter, D.A., Quanbury, A.O., Hobson, D.A., Sidwall, H.G., Reimer, G., Trenholm, B.G., Steinke, T., Shlosser, H.(1974) *Kinematics Of Normal Locomotion - A Statistical Study Based On T.V. Data* ***Journal of Biomechanics, Vol.7.*** 479-486.

Winter, D.A.(1986) *Strategies and Concerns Regarding the Assessment Of Pathological Gait.* ***Proc. of the North American Congress on Biomechanics. Montreal, 1986. Aug. 25-27.*** 171-172.

Woltring, H.J.(1975) *Single- And Dual Axis Lateral Photodetectors Of Rectangular Shape.* ***IEEE Tran. on ED, 22.*** 581-590.

Woltring, H.J.(1990) *Planar Control In Multicamera Calibration For 3D-Gait Studies.* ***J.Biomechanics Vol.13.*** 39-48.

Zatsiorsky, V.M., Aktov, A.V.(1990) *Biomechanics of highly precise movements. The aiming process in air rifle shooting.* ***Journal of Biomechanics, vol. 23. no. 1.*** 35-41.

TECHNICAL REPORTS OF THE
TECHNICAL UNIVERSITY OF BUDAPEST

SER. ELECTRICAL ENGINEERING:

TUB–TR–93–EE01 Tamás Dabóczi: Deconvolution of Noisy Transient Waveforms, Jan. 1993

TUB–TR–93–EE02 Molnár Sándor: Congestion Controll and Queueing Models in ATM Networks, Feb. 1993

TUB–TR–93–EE03 József Zoltai: New Feedback Structure for Monolithic Integrated Instrumentation Amplifiers, March 1993

TUB–TR–93–EE04 Ákos Jobbágy: Centre Estimation in Marker Based Motion Analysis, April 1993

9397